INVESTIGATION ON SUBCOOLED FLOW BOILING HEAT TRANSFER TO WATER-ETHANOL MIXTURE IN CONVENTIONAL CHANNEL

Thesis

Submitted in partial fulfillment of the requirements for the Degree of

DOCTOR OF PHILOSOPHY

By

SUHAS B.G
(135013ME13F09)

DEPARTMENT OF MECHANICAL ENGINEERING
NATIONAL INSTITUTE OF TECHNOLOGY KARNATAKA
SURATHKAL, MANGALORE – 575025

February, 2018

DECLARATION

By the PhD research scholar

I hereby declare that the Research Thesis entitled **"INVESTIGATION ON SUBCOOLED FLOW BOILING HEAT TRANSFER TO WATER-ETHANOL MIXTURE IN CONVENTIONAL CHANNEL"** which is being submitted to the **National Institute of Technology Karnataka, Surathkal** in partial fulfillment of the requirements for the award of the Degree of **Doctor of Philosophy** in **Mechanical Engineering** is a *bonafide report of the research work carried out by me*. The material contained in this Research Thesis has not been submitted to any other Universities or Institutes for the award of any degree.

Register Number: **ME13F09**

Name of the Research Scholar: **SUHAS B G**

Signature of the Research Scholar:

Department of Mechanical Engineering

Place: NITK-Surathkal

Date:

CERTIFICATE

This is to certify that the Research Thesis entitled **"INVESTIGATION ON SUBCOOLED FLOW BOILING HEAT TRANSFER TO WATER-ETHANOL MIXTURE IN CONVENTIONAL CHANNEL"** submitted by **Mr. SUHAS BG (Register Number: 135013ME13F09)** as the record of the research work carried out by him, *is accepted as the Research Thesis submission* in partial fulfillment of the requirements for the award of the Degree of **Doctor of Philosophy.**

Dr. Sathyabhama A
Research Guide
Date:

Dr. Narendranath S
Chairman-DRPC
Date:

A C K N O W L E D G E M E N T

I would like to express my deep sense of gratitude and appreciation to my project guide **Dr. Sathyabhama A**, Assistant Professor, Department of Mechanical Engineering for the guidance given for the completion of this project. She suggested me the research problem and provided all the facilities for doing my work in progressive way. She always supported me by her expert guidance and valuable remarks during my research work. I am also thankful to **Dr. Prasad Krishna** and **Dr. Gangadharan K V,** Professor and former Head, Department of Mechanical Engineering, **Dr. Narendranath S** Professor and Head, Department of Mechanical Engineering for their help and wholehearted support.

I extend appreciation to **Mr. Sreejith B K,** and **Mr. Avadooth Walnuj,** the research scholars, Department of Mechanical Engineering and all other research scholars for their friendship and the support they have given me throughout the project work. And foremost, I would like to express my deepest gratitude to my family for always being there with me to provide the best opportunities in my life. Finally, I would like to thank all those who have helped me directly or indirectly in completing this project work.

TABLE OF CONTENTS

LIST OF FIGURES

LIST OF TABLES

NOMENCLATURE

Bo	Boiling number
C_D	Drag coefficient
C_p	Specific heat (kJ/kg-K)
C_L	Lift coefficient
c	Courant number
d	Diameter (mm)
d_h	Hydraulic diameter (m)
Er	Ertos number
F_b	Buoyancy force (N)
F_{cp}	Force due to contact pressure (N)
F_{du}	Force due to unsteady growth (N)
F_h	Force due to the hydrodynamic pressure (N)
F_{qs}	Force due to quasi static force (N)
F_{sx}	Force due to surface tension in parallel direction (N)
F_{sl}	Force due to lift (N)
F_{sy}	Force due to surface tension in normal direction (N)
F_x	Force parallel to flow direction (N)
f	Bubble frequency (1/s)
h	Heat transfer coefficient (kW/m^2-K)
h_{fg}	Latent heat of vaporization (kJ/kg)
Ja	Jakob number
k	Thermal conductivity (W/m-K)
M	Molecular mass of the liquid
m	Mass flow rate (kg/s)
N_a	Nucleation site density (m^{-2})
Nu	Nusselt number
Pr	Prandtl number
p	Pressure (Bar)

Re	Reynolds number
q''	Heat flux (kW/m^2)
t	Time
T	Temperature (K)
u	Liquid velocity in parallel direction (m/s)
$u*$	Liquid velocity of previous iteration (m/s)
u'	Corrected liquid velocity (m/s)
x	Vapour fraction
X	Position (m)
We	Weber number
$z*$	Dimensionless position

Greek Symbols

α	Bubble void fraction
α_A	Bubble void fraction in accepter cell
α_D	Bubble void fraction in donor cell
$\widetilde{\alpha_D}$	Normalized bubble void fraction in donor cell
α_f^{**}	New value of bubble void fraction in face cell
$\widetilde{\alpha_f}$	Normalized bubble void fraction in face cell
$\widetilde{\alpha_{fBC}}$	Boundedness criteria for bubble void fraction in face cell
$\widetilde{\alpha_{fquick}}$	QUICK scheme for bubble void fraction in face cell
α_f^c	Corrected value of Bubble void fraction in face cell
β_f	Weighing factor
β_f^*	New value of weighing factor
Δp_{Sat}	Difference between the saturated pressure and vapour pressure (Bar)
$\Delta p'$	Corrected pressure drop (Bar)
Δp^*	Pressure drop of previous iteration (Bar)
ΔT	Temperature difference (K)

ΔT_W	Wall superheat (K)
ΔU	Relative velocity between liquid and bubble (m/s)
δ_{Th}	Thermal boundary layer thickness (mm)
ρ	Density (kg/m^3)
μ	Dynamic viscosity (kg/m-s)
ω	Uncertainty

Subscripts

BC	Boundedness criteria
b	Bubble point
cr	Critical
d	Dew point
dep	Departure
ch	Channel
cp	Calculated parameter
Exp	Experimental
ev	Evaporation
f	Fluid
fc	Forced convection
fr	First row
fw	Wall and fluid
g	Growth
i	First sample
i+1	Next sample
in	Inlet
ip	Independent parameter
n	Total number of samples
nb	Nucleate boiling
l	Liquid

lm	Mixture in liquid phase
Pred	Predicted
pb	Pool boiling
QUICK	Quadratic ultimate implicit convection kinetics
rel	Relative motion between the bulk fluid and the bubble
Sat	Saturated
Sr	Second row
St_{rl}	Strouhal number
s	Single phase
tp	Two phase
vm	Mixture in vapour phase
w	Waiting
W	Wall
σ_i	Standard deviation

Abbreviation

CRI	Colour refractive index
DMX	Digital multiplex
RSS	Root sum square

CHAPTER 1

INTRODUCTION

1.1 APPLICATION OF BOILING HEAT TRANSFER IN COOLING HEAT DISSIPATIVE DEVICES

In nuclear, petroleum, chemical, automobile industries heat is dissipated from the catalytic reactors, batteries, electronic devices, burners, radiators etc. To prevent the overheating of these devices an efficient cooling system is required. In some devices heat flux is high enough to encounter subcooled boiling of the coolant. Following are the industries and equipment where cooling is of critical interest.

1.1.1 Hybrid electric vehicle battery module cooling

The rising price of oil and the environmental concern lead automotive industry to develop suitable alternatives such as electric and hybrid electric vehicles (HEV) in place of oil based engines. The electric and hybrid vehicles decrease the use of gasoline and diesel automotive engines. Electric vehicle runs on battery and HEV run on both fuel and battery. (Lokendra, 2010). HEV are operated by lithium ion (Li-ion), nickel-zinc and lead acid battery. The heat generated from these battery cells causes significant effect on the performance of the vehicle. The previous studies have measured the heat generated by these cells (Said Al et al, 2004 ; Thanh et al, 2014). In all these studies, there is a significant variation depending on battery temperature, discharge rate and state of charge (SOC). The value of heat generation for these cells were measured between 2 W to 20 W per cell which sometimes peaks up to 50 W due to increasing temperature of the battery module (Anthony, 2011). At this temperature the active chemicals break down causes more effect on durability and performance. Hence battery temperature should be maintained, so as to establish both performance and durability which are critical in HEV applications.

1.1.2 Steam reforming industries

Hydrogen fuel is a potentially strong contender as an energy carrier. It is produced by steam reforming of ethanol on microscale platforms. Such systems require a preheater for liquid to vapor conversion and a gas-phase catalytic reactor. At higher heat flux, the channel is

subjected to axial back conduction from the single-phase vapor region to the two-phase liquid-vapor region, thus raising local wall temperatures (Moharana et al. 2011).

1.1.3 Electronic devices

In recent years, electronic devices, such as micro-processors, are reduced in size. This has led to increasing intensity in heat generation which needs to be removed during the operation. One method of cooling is to use a boiling fluid as the coolant which transfers more heat. This has led to an abundance of research into boiling in small diameter channels (Mcniel et al. 2010).

1.1.4 Nuclear power plants

According to International Atomic Energy Agency, nuclear reactors whose electric power output is less than 300 MW are classified as small modular reactors. There are different small modular reactor designs like water cooled reactors, high temperature gas cooled reactors, liquid metal cooled reactors and molten salt reactors. Here the coolants used absorb significant amount of heat.

1.2 SIGNIFICANT AMOUNT OF MODE OF COOLING

Maintaining the peak temperature of the heat dissipative devices below an allowable level is a major concern in the design of a cooling system (Yan, 2013). Cooling by a fluid can be divided into two categories, i.e., direct and indirect cooling. Direct cooling permits contact between the fluid and heat source, where as in indirect cooling a conductive thick plate known as cold plate is placed between the heat source and the flowing fluid as heat transfer interface (Hajmohammadi et al. 2013). The fluid is passed through channels in the cold plate. Based on engineering practice and application areas mentioned in section 1.1, if the channel hydraulic diameter ranges from 3 to 25 mm, then it is known as conventional channel.

1.3 COLD PLATES WITH CONVENTIONAL CHANNELS

1.3.1 General classification of cold plate

The cold plate configuration is classified into four major types as shown in Figure 1.1 (Kandlikar and Clifford, 2009).

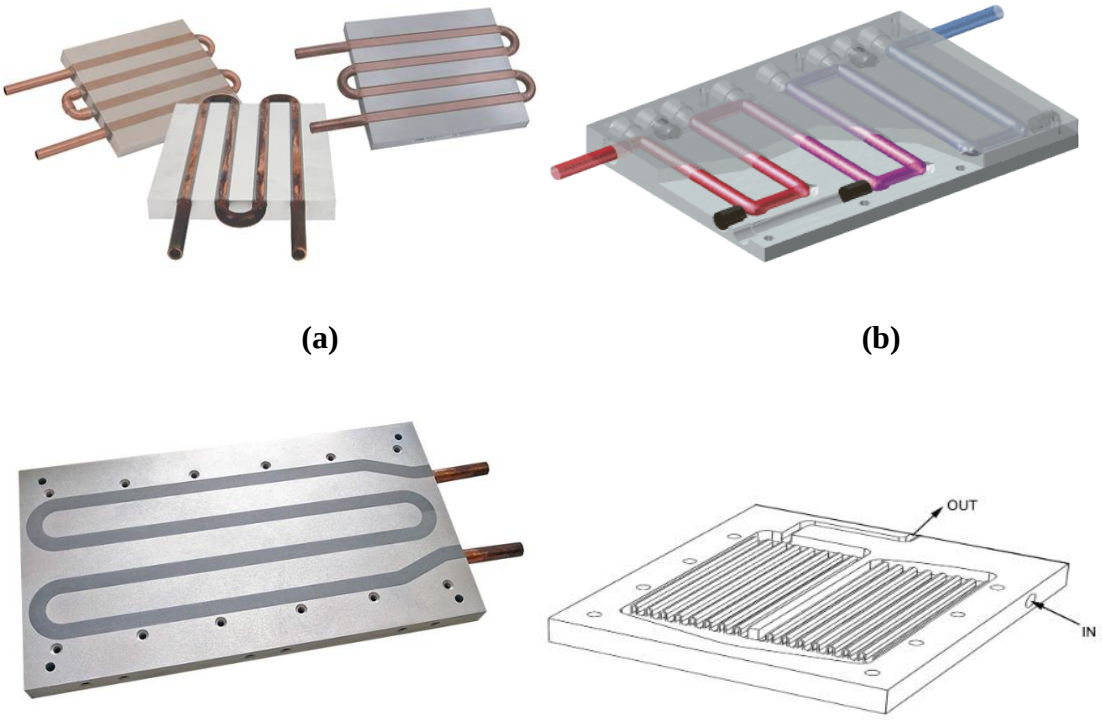

(a) **(b)**

(c) **(d)**

Figure 1.1: Cold plates with conventional channels **(a):** FTCP. **(b)** DDCP. **(c)** MCCP. **(d)** PFFCP (http://www.lytron.com/Cold-Plates).

a) *Formed Tube Cold Plate* (FTCP): The coolant tubes are inserted to the cold plate by soldering or using thermal epoxy. In this design, copper plate or aluminum plate is generally used. This kind of design is used for low heat flux applications of 10-25 W/cm^2.

b) *Deep Drilled Cold Plate* (DDCP): In this design, deep holes are drilled in the plane of the plate, which are generally made of copper or aluminum. These holes are fitted with end caps (or plugs) to create coolant flow path through the plate. This kind of design is used for medium heat flux applications of 50-100 W/cm^2.

c) *Machined Channel Cold Plates* (MCCP): In this design, the channels are machined in the base plate itself. Depending on the thermal performance, these channels vary in width from 10 mm to 200 μm. This kind of design is used for high heat flux applications of above 100 W/cm^2.

d) *Pocketed Folded-Fin Cold Plates* (PFFCP): In this design recessed pockets are machined in the form of various folded fin inserts and are soldered inside the passages. The local heat transfer coefficient, as well as the surface area in the coolant passages, can be enhanced by introducing fins in the coolant channels. This kind of design is used for extremely high heat flux applications of above 250 W/cm^2.

1.3.2 Optimum design of cold plate

Three important performance measures considered are temperature uniformity along the cold plate, mean wall temperature of the cold plate and pressure drop. The mean wall temperature of the cold plate is the most sensitive to the operating conditions, especially with respect to the distribution of the input heat flux, and also to the coolant flow rate. The role of the cold plate is to work on the unfavorable non uniform heat flux distribution at the lower surface of the plate. Few designs are available for channel path in the cold plates. They are serpentine shaped, single S configured and double S configured cold plates. These designs lead to pressure drop of the coolant at higher flow rate. But the pressure drop is negligible for the cold plate with rectangular straight channel. The thick plate with variable cross section area has revealed no significant advantage in the literature. Therefore optimization of the channels in cold plate is not significant. The minimizing the peak temperature of the cold plate depends upon the Reynolds number of the fluid flow, Prandtl number and the material thermal conductivity (Anthony and Yong, 2011).

1.4 FUNDAMENTALS OF FLOW BOILING

When a heated surface of the cold plate exceeds the saturation temperature of the surrounding coolant, boiling occurs on the surface. If the bulk fluid temperature is below the saturation temperature, boiling is referred to as subcooled boiling. If the bulk fluid temperature is equal to the saturation temperature, then saturated boiling is said to occur. Bubbles formed on the heated surface depart from it and are carried away by the bulk fluid. In subcooled boiling, this process results in further heating of the fluid towards the saturation temperature. In saturated boiling, bubbles can be carried along the entire length of the heated channel without collapsing (Tong and Tang, 1997). The various regimes of heat transfer in the flow boiling are illustrated in the subsections 1.4.1 and 1.4.2.

1.4.1 Vertical flow boiling

The upward flow of a liquid in a vertical channel with heated walls is shown in Figure 1.2. The various flow patterns corresponding to heat transfer regions along the length are explained in this figure. When the heat flux from the heating surface is increased above a certain value, the convective heat transfer is not significant to prevent the wall temperature from rising above the saturation temperature of the coolant. The elevated wall temperature superheats the liquid in contact with the wall and activates the nucleation sites, generating bubbles to produce incipience of boiling. It also initiates the formation of vapor. This regime is termed as partial nucleate boiling and also as onset of nucleate boiling. As the heat flux is increased, more nucleation sites are activated until fully developed nucleate boiling is occurred. The region B in the figure indicates the subcooled nucleate boiling consisting of partial nucleate and fully developed nucleate boiling. In this region, the wall temperature remains constant above the saturation temperature. The amount by which the wall temperature exceeds the saturation temperature is called degree of super heat, ΔT_{sat}, and the difference between the saturation and local bulk fluid temperature is the degree of subcooling ΔT_{sub}.

The regime C is called the saturated nucleate boiling. The vapor bubbles growing from wall sites detach to form bubbly flow. With the production of more vapor, the bubble population increases along the length of the channel. The coalescence takes place to form slug flow and then followed by annular flow as shown in the region D and E. At this regime, the formation of vapor will cease. Further vapor formation is due to evaporation at the liquid film-vapor interface, thus increasing velocity in the vapor core interface causes entrainment of liquid in the form of droplets as shown in region F. Since nucleation is completely suppressed, the heat transfer process becomes two-phase i.e., forced convection and evaporation. The depletion of the liquid from the film by entrainment and evaporation causes the film to dry out completely. Droplets continue to exit in region G and the corresponding flow pattern is called drop flow. Drops in this region, which is shown as region H, are slowly evaporated to form single phase vapor (Tong and Tang, 1997).

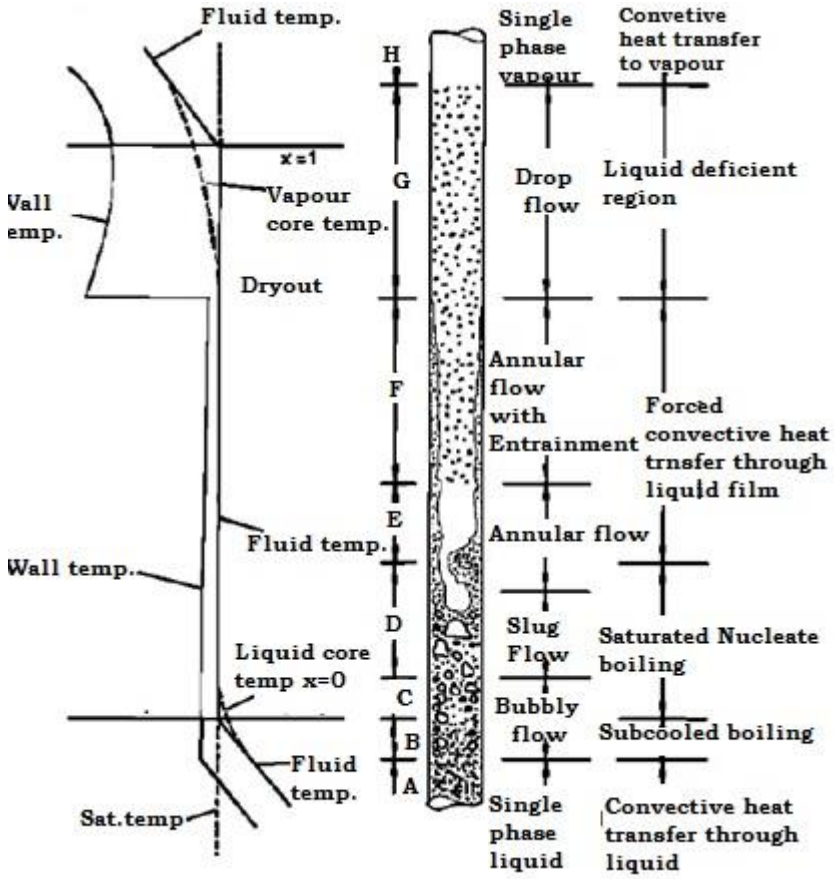

Figure 1.2: Regions of heat transfer in vertical flow boiling (Collier, 1994).

1.4.2 Horizontal flow boiling

Flow pattern formed during generation of vapor in a horizontal tube is shown in Figure 1.3. The regions of flow and the mechanisms of horizontal flow boiling are similar to that of vertical flow boiling. But the asymmetric distribution of the vapour and liquid phases due to effect of gravity makes horizontal flow complicated compared to vertical up flow. There is an intermediate flow which exists between the bubbly and the slug flow called as plug flow. The plug flow consists of elongated gas bubbles. The wavy flow which exists between the annular flow and slug flow is absent in vertical flow. In a wavy flow, the top of the tube may be intermittent dry if the waves wash the top of the tube. These waves leave behind thin films of liquid that may or may not evaporate completely before the arrival of the next wave. Annular flow the film is thicker at the bottom than at the top and

progressively increases around the perimeter of the tube in the direction of flow (Wolverine tube- INC, 2007).

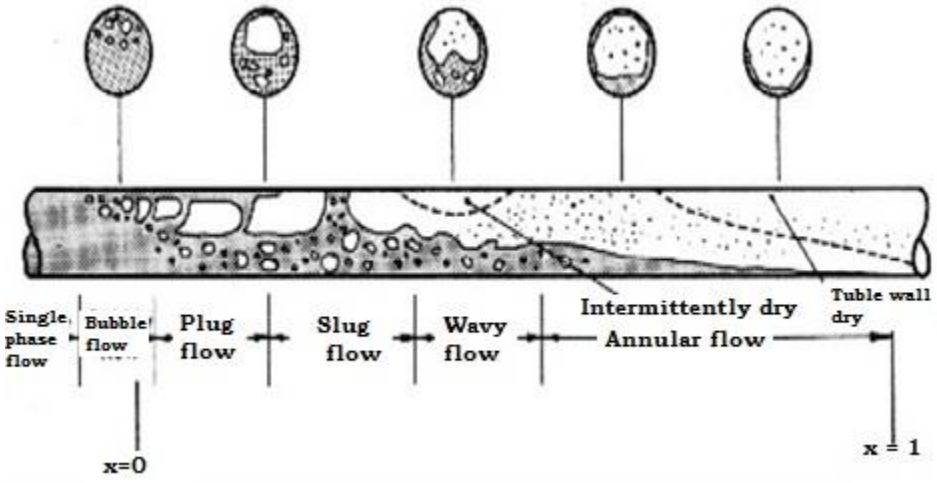

Figure 1.3: Flow pattern during horizontal flow boiling in tubes (Collier, 1994).

1.5 WATER-ETHANOL MIXTURE AS COOLANT

The liquid which is used as coolant must meet certain requirements. The ozone depletion potential (ODP) and global warming potential (GWP) must be minimum for these coolants. The coolant must have high-dielectric strength prevent current from travelling through the working liquid which causes damage or malfunction of battery component by short circuit. In the past decades, refrigerants were mainly used as coolants. But the impact of these refrigerants on the environment in terms of global warming and ozone depletion has been identified in recent times. The use of binary mixtures is one of the alternatives for the refrigerants. The binary mixture like water-glycol are expensive and require higher pumping power due to their higher viscosity. Water-methanol, water-butanol and water-propanol are toxic in nature. For cost effectiveness and environmental concerns water-ethanol mixture can be used in cooling knowledge of the heat dissipative devices. To design a cooling system with water-ethanol as a coolant, its flow boiling characteristics are essential.

Flow boiling of binary mixtures is more complicated than the corresponding pure fluids due to following reasons (a) boiling point temperature varies with the mixture composition (b) thermo-physical properties of the mixture do not follow the linear mixing

law (c) the overall transport mechanism is limited by the mass transfer process of the less volatile component during phase-change, and (d) the bulk liquid contact angle, which is important for understanding boiling mechanism, usually shows highly non-linear behavior with varying concentration (Lixin and Dieter, 2006). There is very limited availability of literature on flow boiling of binary mixtures, other than refrigerants, especially in conventional, mini and microchannels.

The subcooled flow boiling of water-ethanol mixture is pertinent to the operation of small catalytic reactors, electronic devices and HEV battery module. It is well known that the operational temperature must be maintained to avoid any malfunction of these heat dissipative devices. Moreover, the two-phase flow boiling is one of the most effective methods because of the high latent heat involved in the process. Detailed investigation on subcooled flow boiling of water-ethanol mixture is limited in literature which is essential to design the cooling devices. In view of this, the present study aims to determine the forced convective and subcooled flow boiling heat transfer coefficients of water-ethanol mixture. The understanding of the bubble behavior and its effect on heat transfer significantly contributes to a better understanding of physical phenomena in subcooled flow boiling. Hence flow visualization is essential to study the bubble dynamics of water-ethanol mixture during subcooled flow boiling.

1.6 ORGANIZATION OF THE THESIS

This thesis consists of eight chapters namely introduction, literature review, methodology, results and discussions, conclusions and the reference followed by appendices.

The second chapter reviews the literature available on battery module cooling, forced convective heat transfer and subcooled boiling heat transfer, bubble dynamics and correlation development. Summary of the literature review followed by the objectives are given at the end of this chapter.

The third chapter is the experimental approach in which details of the experimental test set up, procedure followed for visualization, data reduction for heat transfer coefficient and uncertainties are given.

The fourth chapter discusses the experimental results obtained for forced convective and subcooled flow boiling heat transfer coefficients. The results also include prediction of onset of nucleate boiling (ONB), onset of vapour generation (OSV) by heat flux partitioning analysis for the water-ethanol mixture. The Comparison between the experimental results and those predicted from the developed mechanistic correlation based on heat transfer approach is also given.

The mathematical modelling and numerical simulation which are used to determine the forced convective heat transfer coefficient are given in chapter 5. The mathematical modeling used to determine the subcooled flow boiling heat transfer coefficient and its comparison with that of experimental results is also given.

The bubble dynamics of the water ethanol mixture is discussed in chapter 6. The effect of bubble parameters like bubble departure, growth period and waiting period on heat transfer coefficient are discussed. The Comparison between the experimental results and those predicted from the developed mechanistic correlation based on bubble dynamic data are also added.

The seventh chapter concludes the results obtained from the present study.

CHAPTER 2

LITERATURE REVIEW

Literature review for this dissertation is divided into four sections. The first section provides literature on forced convective and subcooled flow boiling and second section concerns with the literature on bubble dynamics. The third section reviews the literature regarding correlation development and the fourth section provides literature on numerical analysis.

2.1 FORCED CONVECTIVE AND SUBCOOLED FLOW BOILING

Inigo et al. (2013) conducted a simulation work on lithium ion batteries cooling for automotive application to analyze battery module design and assess the temperature of the cells along the testing time. For analysis CFD simulation using STAR CCM+ software was used. Two versions displayed for one set of cold plates with cold extrusion and the other set without cold extrusion were considered. The channel path was serpentine shaped to which the tube of circular cross section was inserted. The coolant chosen was de-ionized water. In both the cases the internal temperature of the battery cells did not exceed the operating range specified by the manufacturer, and hence both systems were considered as valid approach for cooling batteries for hybrid electric vehicles.

Anthony and Yong (2014) determined the influence of different operating conditions such as heat flux and mass flow rate on the cooling plate design by assessing a thin rectangular aluminum block having serpentine path of rectangular cross section channel. The cold plates were vertically sandwiched between the battery cells. Water-glycol mixture was passed through the channel. A model for the cooling plate was developed with the computational fluid dynamics (CFD) pre-processor GAMBIT. Three important performance measures considered were temperature uniformity, mean temperature, and pressure drop. They were analyzed using the commercial CFD solver-FLUENT. It was found that of these three, temperature uniformity was most sensitive to the operating conditions, especially with respect to the distribution of the input heat flux and the coolant flow rate. The mean temperature decreased with increase in coolant flow rate.

Kandlikar (2002) compared the flow pattern occurring in the conventional channels and small diameter channels. He found that the flow pattern was similar between these two types of channels. The role of surface tension becomes more important in smaller diameter channels than in the conventional channels. Due to the dominance of surface tension, stratified flow was absent. The slug, plug and churn flow patterns occurred over extensive ranges of parameters such as wall superheat and heat fluxes than the conventional channels. The slip velocity under these patterns was small. Stratified flow existed at very low flow rates.

Kandlikar and Mark (2004) conducted experiment to study the single phase flow of degassed water in 207 mm hydraulic diameter trapezoidal channels during laminar flow. The Nusselt numbers for their experimental data fell between the constant temperature and constant heat flux boundary conditions.

Sarfaraz et al. (2012) studied subcooled nucleate flow boiling heat transfer of dilute water–diethylene glycol (DEG) mixture inside a vertical annulus. Results revealed that increase in heat flux caused the single phase heat transfer coefficient to increase till the incipience of bubble formation. The flow boiling heat transfer coefficient increased when heat flux increased.

Chin et al. (2012) conducted an experiment on the convective boiling heat transfer of ethanol–water mixture in a diverging microchannel with artificial cavities. The result showed that the boiling heat transfer was influenced by the molar fraction as well as the mass flux. For single-phase convection region, except for the region near the onset of nucleate boiling, single-phase heat transfer coefficient was independent of wall superheat and increased with a decrease in the molar fraction. After boiling incipience, two-phase heat transfer coefficient was much higher than that of single-phase convection. The two-phase heat transfer coefficient showed a maximum in the region of bubbly-elongated slug flow and deceased with further increase in the wall superheat.

Yuan et al. (2012) investigated flow boiling heat transfer in high aspect ratio microchannels for ethanol and FC-72 fluid. The channel wall temperature profiles and fluctuations as well

as two-phase heat transfer coefficients were obtained. FC-72 and ethanol showed similar bubble dynamics during boiling in micro-channels. Flow regimes including bubble nucleation, confined bubbly flow which rapidly turned into slug-annular flow were observed. FC-72 has very low surface tension when compared to ethanol and it completely wets the glass wall. Onset of nucleate boiling increased with increase in mass flux for both fluids. The heat flux for onset of nucleate boiling occurred at lower wall super heat for ethanol when compared with the FC-72 fluid.

Mahorana et al. (2013) conducted an experiment using water-ethanol mixtures in a 256 μm square channel. The heat transfer coefficient remained almost constant in the single-phase region but increased in the two-phase region. Heat transfer coefficient decreased at higher wall superheat.

Wang et al. (2014) conducted series of experiments on boiling incipience for water. The inception wall superheat was dependent on the inlet subcooling, heat flux and mass flux, but the variation of pressure was not significant in boiling incipience.

2.2 BUBBLE DYNAMICS

Gunther et al. (1951) observed that bubbles collapsed while sliding along the heated surface of bottom wall of the channel.

Gorenflo et al. (1986) assumed that the bubble detaches if the combination of buoyancy and drag force is able to overcome the force due to surface tension. The drag force includes the quasi-steady drag in the bulk liquid flow direction, the unsteady drag due to asymmetric growth of the bubble in the direction of the liquid flow and the shear lift force.

Bibeau and Salcudean (1994) conducted an experiment on subcooled flow boiling of water. They found that the bubbles were sliding along the heated surface of channel before being ejected into the bulk subcooled liquid. Since the bubbles were collapsed due to condensation, they did not travel further after nucleation.

Zeitoun and Shoukri (1996) observed that the bubbles detached from the channel surface. They developed an empirical correlation for the mean bubble departure diameter as a function of the Reynolds number, Jakob number and the boiling number.

Thorncroft et al. (1998) observed the bubble behavior in subcooled vertical flow boiling using FC-87. They found that the bubble slide along the heated surface but did not lift off during upward flow. In contrast, in downward flow, bubbles were lifted off from the nucleation site.

Nilanjana et al. (2002) studied onset of nucleate boiling and active nucleation site density during subcooled flow boiling. Active nucleation site density data is required to account for the energy carried away by the bubbles departing from the wall. Subcooled flow boiling experiments were conducted using a flat plate copper surface. The location of ONB during the experiments was determined from visual observation as well as from the thermocouple output. From the data obtained, it was found that the heat flux and wall superheat required for inception were dependent on flow rate, liquid subcooling and contact angle.

Okawa et al. (2005) studied the bubble behavior of water in the subcooled boiling region. They observed that some of the bubbles slid along the vertical surface and did not lift off. But few of them lifted off the surface after sliding along the surface.

Reinhold et al. (2006) investigated the nucleate boiling regime for water circulating in a closed loop at atmospheric pressure. The horizontal oriented test-section consisted of a rectangular channel with one side heated copper strip and good optical access. The bubble behavior was recorded by the high-speed cinematography and by a digital high resolution camera. It was found that with increasing mass flux the bubble lifetime decreases and for high mass fluxes no bubbles reach a lifetime of more than 1.5 ms.

Vijay et al. (2007) carried out force balance in both the directions during flow boiling, i.e., flow directions parallel to the heating surface and normal to heating surface. He estimated the theoretical bubble departure size from the force balance approach.

Tannaz and Suresh (2009) conducted experiment with FC-77, to investigate the effects of channel size and mass flux on microchannel flow boiling regimes by means of high-speed photography. Seven different silicon test pieces with parallel microchannels of widths ranging from 100 μm to 5850 μm, with a depth of 400 μm. Flow visualizations were performed with a high-speed digital video camera. The local measurements of the heat

transfer coefficient are simultaneously obtained. The visualizations and the heat transfer data showed that the flow regimes with nucleate boiling was dominant in these channels over a wide range of heat flux. In contrast, flow regimes in the smaller microchannels were different and bubble nucleation at the walls was suppressed at a relatively low heat flux for these sizes.

Fu et al. (2010) studied the bubble growth, departure and the following flow pattern evolution during flow boiling in the mini-tube. The bubble growth rates were investigated upto the bubbles departing from the nucleation site. The bubble size was noted to be increased which indicated that it was governed by the inertial force. Mass flux and heat flux were found to be two major factors affecting the bubble departure from the nucleation site. The departure diameter of bubbles decreased as the mass flux was increased, while the heat flux posed the inverse trend as the mass flux.

Mukherjee et al. (2011) studied the wall heat transfer mechanism during growth of vapor bubble inside the microchannel of 200 μm square cross section. The vapor bubble grew on the walls with liquid coming through the channel inlet. The numerical results showed that the wall heat transfer increases with wall superheat but remains almost constant with the liquid flow rate. The bubble which had the lowest contact angle resulted in the highest wall heat transfer.

Rouhollah et al. (2012) investigated bubble dynamics of water in the subcooled flow boiling regime using a high speed camera. He used a vertical rectangular channel as test section, and a copper surface as a heated surface. Main experimental parameters were pressure, heat flux, mass flux and liquid subcooling. Although all the experiments were conducted under low void fraction conditions, close to the onset of nucleate boiling, no bubble stayed at the nucleation sites. Depending on the experimental conditions, the following two types of bubble behavior were observed after nucleation: one was, lift-off from the heated surface followed by collapsing rapidly in subcooled bulk liquid due to condensation, and the other one was sliding along the vertical heated surface for a long distance. Since the bubble lift-off was observed only when the wall superheat was high,

the boundary between the lift-off and the sliding could be determined in terms of the Jakob number.

Paz et al. (2015) studied about the growth stages of the bubbles. Initially a small bubble lie above the superheated wall which gradually grows in size. The bubble growth is governed by the forces on the bubble-liquid-wall interfaces. This stage is known as inertia controlled stage of the bubble growth. In the later stage, as the bubble grows, it comes in contact with the liquid at subcooled region. The bubble growth for this stage is controlled by the rate of liquid evaporation near the bubble.

2.3 CORRELATION DEVELOPMENT

During the last five decades, numerous models have been developed to predict the heat transfer rate during subcooled flow boiling. These models can be broadly classified into three categories: i) empirical correlations for wall heat flux, ii) empirical correlations for partitioning of wall heat flux, and iii) mechanistic models for wall heat flux partitioning. The empirical correlations for wall heat flux are generally limited to the prediction of total wall heat flux for a particular flow situation. They are merely correlations of experimental data and as such do not include modeling of the heat transfer mechanisms involved.

Stephan et al. (1978) developed correlation on subcooled boiling heat transfer coefficient for water, hydrocarbons, cryogenic fluids and refrigerants which compared well with the experimental data.

Klausner et al. (1993) had developed expressions for surface tension force based on variation of contact angle along the periphery of the bubble. It was found that the surface tension alone is unable to prevent the bubble departure. The liquid drag on the bubble due to asymmetrical bubble growth acting in the direction opposite to liquid flow is important in holding the bubble to its nucleation site before departure.

Nilanjana et al. (2005) developed mechanistic model for the wall heat flux partitioning during subcooled flow boiling. In the proposed model the entire energy from the wall was first transferred to the superheated liquid layer adjacent to the wall. A portion of the energy was utilized for vapor generation and the rest of energy was utilized for sensible heat of

the bulk liquid. The contribution for this heat transfer to the liquid were from forced convection, transient conduction and energy transport associated with vapor generation.

Kandlikar (2004) obtained correlation by fitting the experimental data which gave an explicit relation between several parameter. The mechanism based correlation or mechanistic model incorporates the thermo physical properties, thermodynamic properties and physics involved in the boiling phenomena.

Sarma et al. (2008) developed subcooled boiling heat transfer coefficient correlation for water and ethyl alcohol based on experimental data obtained for channel diameter varying between 5 to 7 mm. The correlation predicted the experimental values with a maximum deviation of ±16% .

2.4 NUMERICAL ANALYSIS

Vijay, et al. (2007) conducted numerical simulations of the bubble dynamics for de-ionised water. They studied the effects of wall superheat, liquid subcooling, contact angle and level of gravity on bubble growth process, bubble diameter at departure, and growth period. The bubbles merged normal to the heater as well as along the heater leading to the formation of vapor columns and mushroom type bubbles. The merger process is highly nonlinear. As the wall superheat is increased the bubble diameter at departure increased but the growth period decreased. With the increase in wall superheat, the rate of heat transfer into the vapor bubble increased and hence the growth period.

Tomasz and Tadeusz (2008) studied an alternative approach to the problem of preserving interface resolution to discretize the convective scalar transport equation for the bubble volume of fraction (α) with a differencing scheme. This scheme guarantees physical (bounded) values of α while preventing the smearing of the transitional area over several mesh intervals. Basically α is the presence of bubble in the subcooled fluid and its presence affects the thermophysical and thermodynamic properties of the fluid.

Ronghua et al. (2010) studied two-dimensional numerical simulation of bubble dynamics during nucleate flow boiling. The bulk liquid velocities ranged from 0.07 m/s to 0.3 m/s. The surface orientations varied from vertical to horizontal through 60º, 45º and 30º. Bulk

liquid subcooling varied from 0° C to 6.5° C and wall superheat from 2°C to 20°C. The results showed that the bulk liquid velocity and surface orientation influenced the bubble diameter and lift off time. Bubble slid along the heater surface before lifting off and the sliding velocity increased with an increase in bulk liquid velocity at lift off.

2.5 MOTIVE AND SCOPE OF THE PRESENT WORK

From the detailed literature review presented in the above sections, it is clear that experimental investigations on saturated and two phase convective flow boiling of pure components and binary mixtures are well reported. There is a lack of information on subcooled flow boiling of water-ethanol mixture. There is insufficient literature on bubble dynamics of water-ethanol mixture in the subcooled flow boiling region. Correlations to predict subcooled and saturated flow boiling heat transfer coefficients of pure components are well established, however, little effort is gone into the development of correlation for subcooled flow boiling heat transfer coefficient of binary mixtures and are not available for water-ethanol mixture. The experimental studies to date on the flow boiling have yielded only limited information on the basic two-phase hydrodynamic characteristics of binary mixtures. On the other hand, benefit from the recent advancement of numerical analysis can be considered as an alternative tool to provide useful physical information with limited cost. However, the detailed literature shows that the numerical analysis for determining the forced convective and subcooled flow boiling heat transfer coefficients for water-ethanol mixtures are not available.

In view of the great significance of the reliable data for water-ethanol mixture as an alternative coolant, an independent study is undertaken here to determine the subcooled flow boiling characteristics of this mixture.

2.6 OBJECTIVES OF THE PRESENT RESEARCH WORK

1. To determine the forced convective and subcooled flow boiling heat transfer coefficients of water-ethanol mixture experimentally and numerically.
2. To investigate the bubble dynamics of water-ethanol mixture.
3. To develop the mechanistic correlations to predict the subcooled flow boiling Nusselt number of water-ethanol mixture.

CHAPTER 3

EXPERIMENTAL METHOD

Present chapter consists of experimental approach in which, details of the experimental test set up, procedure followed for visualization, data reduction for heat transfer coefficient and uncertainties are reported.

3.1 EXPERIMENTAL SETUP AND PROCEDURE

The schematic diagram of the experimental test set up is shown in Figure.3.1 (a). Figure 3.1(b) and 3.1 (c) are the photographic images of the experimental set up.

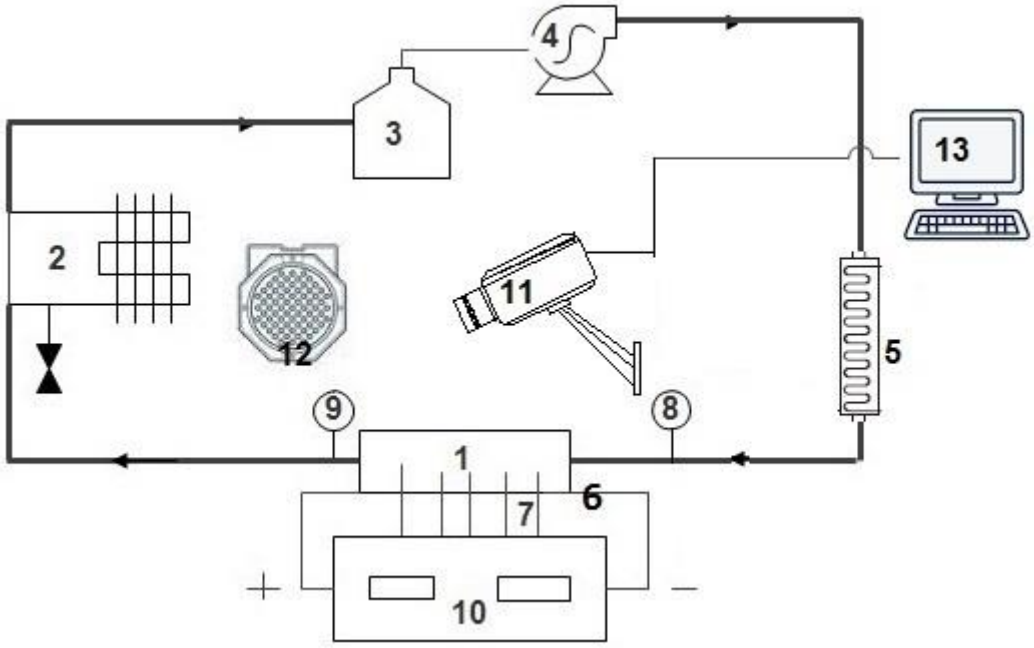

Figure 3.1 (a): Schematic diagram of experimental setup (1) Rectangular aluminium block consisting of two rectangular channels (2) Condenser coil dipped in ice water bath (3) Reservoir (4) Peristaltic pump (5) Preheater (6) Cartridge heaters (7) Thermocouples to measure wall temperature (8) Thermocouple to measure fluid inlet temperature (9) Thermocouple to measure fluid outlet temperature (10) Temperature indicator panel (11) High speed camera (12) Light source (13) Data Aquisiation system for flow visualization

The experimental set up is of closed loop type having a rectangular aluminum block consisting of two rectangular conventional channels, condenser coil dipped in ice water bath, reservoir, preheater and variable flow rate peristaltic pump. The aluminum block

consisting of two conventional channels of 150 mm (Length) × 10 mm (width) × 10 mm (height) is shown in Figure 3.2. The two cartridge heaters are inserted inside the aluminum block. The aluminum block is considered as cold plate. Heat loss is prevented by providing mineral wool as insulating material. The wall temperatures, fluid temperature at the inlet and outlet of the channel are measured by thermocouples and are displayed on the temperature indicator panel. The high speed camera is used for flow visualization.

(b)

Figure 3.1 (b): Front view of the experimental setup (1) High speed camera (2) Condenser coil dipped in ice water bath (3) Reservoir (4) Peristaltic pump (5) Preheater (6) Temperature indicator panel (7) Light source

(c)

Figure 3.1 (c): Rear view of the experimental setup (1) Rectangular aluminum block consisting of two rectangular channels (2) Thermocouples to measure wall temperature (3) Thermocouple to measure channel inlet temperature (4) Thermocouple to measure outlet fluid temperature

Figure.3.2: Aluminum block with rectangular conventional channels.

The instrument and equipment used in the experiment are shown in Table 3.1 and summary of operating conditions is presented in Table 3.2.

Table 3.1: Instruments and equipments used in the present experiment

Instrument/Equipment	Specifications
k-type thermocouple (12 no's)	Range :-20℃ to 400℃ Sheath length: 20 mm Sheath diameter: 1.2 mm
Cartridge heater (2 no's)	Diameter: 12.7 mm Length: 150 mm Capacity: 750 W
Peristaltic pump	Capacity: 100 liters per hour Operating pressure: Atmospheric
Preheater	Chamber capacity: 4 Liters Heater capacity: 3 kW.

Figure 3.3 shows the arrangement of thermocouples in the cold plate to measure wall temperature and to calculate heat flux. The first set of five thermocouples (T_{11}, T_{12}, T_{13}, T_{14} and T_{15}) are placed 2 mm below the channel in a row. The second set of five thermocouples (T_{21}, T_{22}, T_{23}, T_{24} and T_{25}) are placed 20 mm below the first row of thermocouple. The distance between two thermocouples in a row is 25 mm. Two cylindrical cartridge heaters are placed 40 mm below the channels.

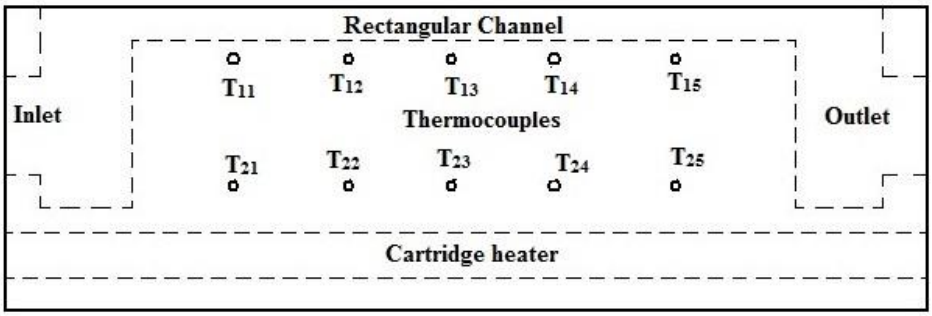

Figure 3.3: Arrangement of thermocouples in the cold plate.

Table 3.2: Operating conditions in the present experiment

Parameter	Operating Range				
	Pure water	25% Ethanol volume fraction	50% Ethanol volume fraction	75% Ethanol volume fraction	Pure ethanol
Hydraulic Diameter (mm)	10				
Heat flux (kW/m^2)	21.78, 35.11, 45.33, 62.33, 78.4, 90.4, 100.5, 109.6, 121.9, 133.47	21.78, 35.11, 45.33, 62.33, 78.4, 90.4, 100.5, 109.6, 121.9	21.38, 35.11 45.33, 62.33 78.4, 90.4 100.3, 109.6	21.78, 35.11 45.33, 62.33, 78.4, 90.4, 100.3	21.78 35.11 45.33 62.33, 78.4, 90.4,
Mass Flux (kg/m^2-s)	76.67, 91.33, 115.33,151.67, 228.33				
Channel Inlet Temperature (K)	303, 313, 323				

Due to possibility of solubility of air in water and ethanol, degassing is done for thirty minutes before commencing the experiment. The liquid is preheated and pumped through the channels. The heat is supplied to the channels by cartridge heater. The liquid after getting cooled in the condenser coil enters the reservoir.

The steps followed during the experiment are listed below:

1. Fill the water in the reservoir.
2. Set the volume flow rate of the liquid and fix the channel inlet temperature by temperature controller in the preheater.
3. Set a heat input value to the channel such that it maintains the wall temperature of the channel above the inlet temperature of the liquid.

4. Note down the bottom wall temperature of the channel and outlet temperature of the fluid when the bottom wall temperature of the channel reaches steady state. Capture the flow by using high speed camera.
5. Change the volume flow rate and repeat step 4.
6. Change the heat input value and repeat step 5. These steps are repeated upto subcooled boiling region (Before attaining saturation state).
7. Change the inlet temperature and repeat the steps 3 to 6.
8. Repeat step 2 to step 7 for 25%, 50%, 75% and 100% ethanol volume fractions.

Flow visualization is carried out using high speed camera to understand the phenomena of heat transfer during the subcooled flow boiling of the mixture. The specifications of high speed camera and LED light are given in Table 3. 3. The steps followed to measure the bubble departure diameter and contact angle by an image processing tool in Lab view 8.5 vision builder software are given in Figure 3.4.

Table 3.3: Specifications of high speed camera and source light

Processor	AOS Promon 501
Lens	50 mm
Aperture setting	f/1.4 D
Shutter speed	1/15
Frames per second	1459
Resolution	480×240 pixels
LED PAR Light	Slim die cast body, Power 120W, beam 25 degree, CRI>85, DMX 512 Auto, sound active, 3 section lightweight aluminum stand

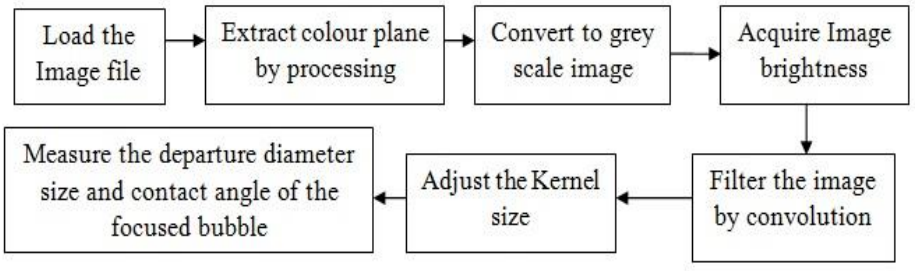

Figure.3.4: Image processing

A tangent is drawn along the bubble as shown in Figure 3.5. The angle between this tangent and the channel surface is considered as the contact angle. The channel width is considered as the reference length to measure the departure diameter. Camera is placed at the top of the channel as shown in Figure 3.6. The trigonometric relations are considered to calculate the actual contact angle. However, there is no significant variation in measuring the bubble departure diameter because the bubbles are assumed to be spherical in shape.

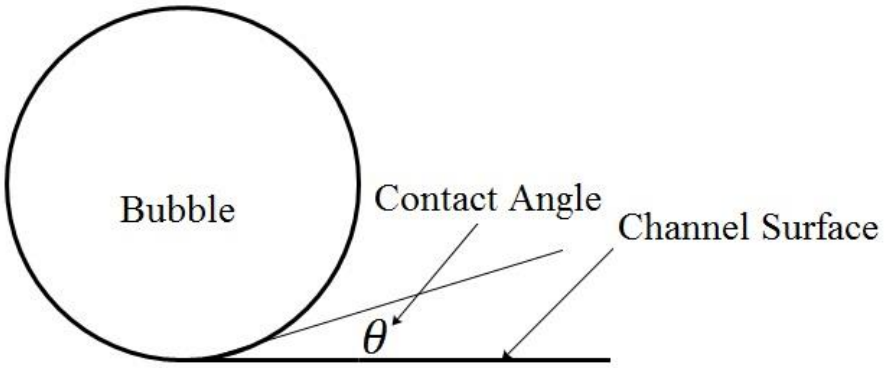

Figure 3.5: Contact angle

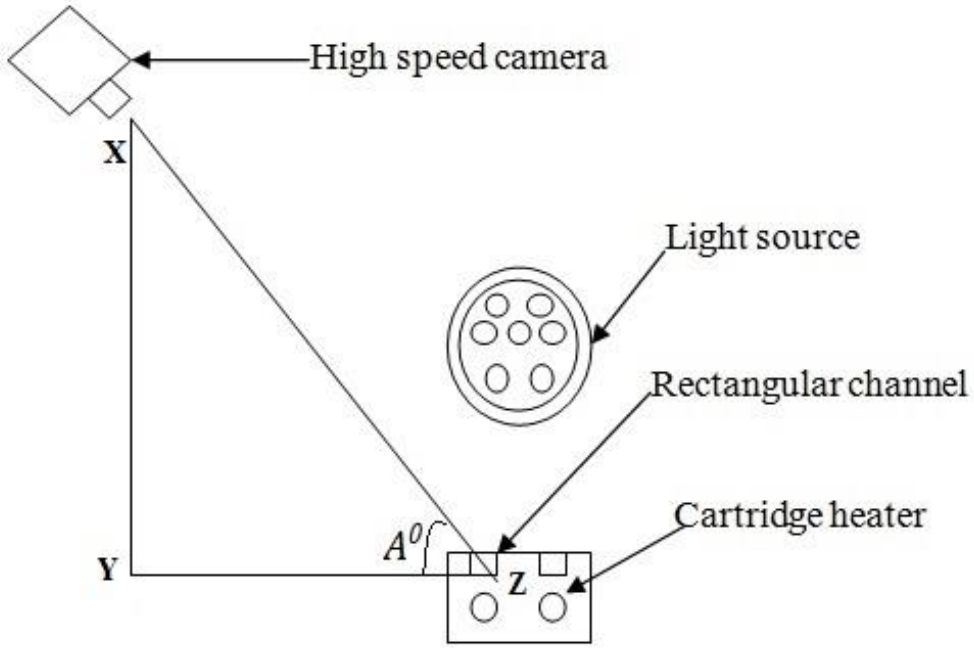

Figure 3.6: High speed camera and the channel.

From the trigonometric relation

$$\frac{XY}{YZ} = \tan(A°)$$

XY is the distance from the camera lens to the point on the camera stand which is parallel to the bottom wall of channel. YZ is the distance from the bottom wall of the channel to the point on the camera stand which is parallel to the bottom wall of channel.

$$A° = tan^{-1}\left(\frac{XY}{YZ}\right)$$

$$\frac{Measured\ contact\ angle}{Actual\ contact\ angle} = \frac{XZ}{YZ} = \frac{XZ}{XZ\ cos(A°)}$$

$$\text{Actual contact angle} = \text{Measured contact angle} \times \cos(\text{A}°)$$

3.2 DATA REDUCTION

Fourier's law of heat conduction given by Equation (3.1) is applied to calculate the heat flux from the measured values of temperature gradient and known value of thermal conductivity of aluminum.

$$q" = -k\frac{dT}{dx} \tag{3.1}$$

The temperature gradient is calculated by Equation (3.2).

$$\frac{dT}{dx} = \frac{(T_{sr} - T_{fr})}{(X_{sr} - X_{fr})} \tag{3.2}$$

The temperature of bottom wall of the channel is assumed to be the same as that of the first row because the first row of thermocouples are very near to the bottom wall. The heat transfer coefficient is calculated by Equation (3.3) from the calculated values of heat flux, calculated values of wall temperature and measured values of fluid temperature. Fluid temperature is the average fluid temperature at inlet and the outlet of the channel.

$$h = \frac{q"}{(T_w - T_f)} \tag{3.3}$$

It is observed that the heat flux value is higher at the inlet of the channel and decreases along the length of the channel. It is also observed that the wall temperature is lower at the entrance and marginally increases along the channel length. Therefore average of five

readings of wall temperature is considered to determine the difference between the wall and fluid temperature.

3.3 UNCERTAINTIES

According to International Bureau of weights and measures (IBWM) and International organization of standards, (ISO) random independent variables may be calculated using root-sum-square (RSS) of standard deviation (Kleine et al. 1953).

$$\omega_{ip} = \sqrt{\omega_{iresolution}^2 + \omega_{iconversion}^2 + \omega_{icalibration}^2 + s_{2\sigma_i}^2} \tag{3.4}$$

After determining the uncertainty of independent variables, the uncertainties of calculated parameters are determined (Claudi, 2010).

$$\omega_{cp}^2 = \sum_{i=1}^{n} \left(\frac{\partial f}{\partial x_i}\right)^2 \omega_{x_i}^2 \tag{3.5}$$

3.3.1 Uncertainty in temperature measurement

The Thermocouples are calibrated against an insulated ice bath and boiling water. The temperature equation follows linear relation which is given as $T_{Actual} = aT_{measured} + b$. The constants (a and b) for temperature measurement corrections are shown in Table 3.4.

Table 3.4: Constants for temperature measurement corrections

Readings	Steam point (K)	Ice point (K)	a	b
T1	372.3	274.1	1.0204	-6.5896
T2	375.4	275.2	1	-2
T3	374.3	275.1	1.0101	-4.778
T4	375.1	275.3	1	-2
T5	374.3	273.1	0.990099	2.7029
T6	374.2	273.2	0.990099	2.7029
T7	373.3	274.2	1.0101	-3.7674
T8	375.2	274.1	0.9901	1.7129
T9	373.2	275.2	1.0204	-7.61
T10	373.1	274.3	1.0101	-3.7674
T11	372.1	273.2	1.0101	-2.75758
T12	371.4	275.1	1.04167	-13.458

After allowing the system to stabilize for a period of two hours in the ice bath, all measured temperature readings fluctuated within $\pm$0.3 ºC. The voltage resolution in the data logger at a 100mv range signal is 0.01mv, corresponding to $\pm$0.1℃ and conversion accuracy is less than $\pm$0.02 ℃. The standard deviation is found to be $\pm$0.15℃. Since, the different components of the uncertainty are independent variables, the combined uncertainty of the temperature measurements can be calculated by Equation (3.6)

$$\omega_T = \pm\sqrt{\omega_{T,resolution}^2 + \omega_{T,conversion}^2 + \omega_{T,calibration}^2 + S_{2\sigma_T}^2} \quad (3.6)$$

3.3.2 Uncertainty in mass flux

The mass flux is the mass flow rate across unit area and is given by:

$$G = \frac{4m}{\pi {d_h}^2} \quad (3.7)$$

The uncertainty in mass flux is given by the uncertainty in liquid mass flow rate and uncertainty in channel dimensions

$$\omega_G = \pm\sqrt{\left(\frac{\partial G}{\partial m}\omega_m\right)^2 + \left(\frac{\partial G}{\partial D_h}\omega_{D_h}\right)^2} \quad (3.8)$$

3.3.3 Uncertainty in heat flux

The uncertainty in heat flux is calculated by the independent variables like uncertainties in the temperature and distance measurements.

$$\omega_{q"} = \pm\sqrt{\left(\frac{\partial q"}{\partial T_{wsr}}\omega_{T_{wsr}}\right)^2 + \left(\frac{\partial q"}{\partial T_{wfr}}\omega_{T_{wfr}}\right)^2 + \left(\frac{\partial q"}{\partial \Delta x}\omega_{\Delta x}\right)^2} \quad (3.9)$$

$\omega_{T_{wfr}}$ and $\omega_{T_{wfr}}$are uncertainties in measuring wall temperatures in the first rows and seconds rows. $\omega_{\Delta x}$ is uncertainty in measuring distance between the first row and second row of thermocouples.

3.3.4 Uncertainty in heat transfer coefficient

The heat transfer coefficient is calculated from the uncertainty values of heat flux and temperature as given by Equation (3.10)

$$\omega_h = \pm\sqrt{\left(\frac{\partial h}{\partial q}\omega_q\right)^2 + \left(\frac{\partial h}{\partial (T_w)}\omega_{T_w}\right)^2 + \left(\frac{\partial h}{\partial (T_f)}\omega_{T_f}\right)^2} \quad (3.10)$$

The maximum uncertainties of measured and calculated parameters are shown in Table 3.5. The uncertainties in mass flux and mass flow rate are given in Table A1 of Appendix A. The details of uncertainties in heat flux and heat transfer coefficient for water at inlet temperature=303 K are shown in Table A2 of Appendix A.

Table 3.5: Uncertainties of measured and calculated parameters

Parameter	Uncertainty
Temperature (K)	±0.35℃ (RSS)/ ±0.1℃ (resolution)
Mass flow rate (kg/s)	±2.32%
Mass flux (kg/m^2-s)	±0.77%
Heat flux (kW/m^2)	±13.3%
Heat transfer coefficient (kW/m^2-K)	±9.11%

3.4 ESTIMATION OF CONFIDENCE INTERVALS

To estimate the data distribution with which the data is spread around the mean, lower and upper confidence intervals are determined for the 285 samples of experimental value of subcooled flow boiling heat transfer coefficient.

For $y_i$individual data points, the arithmetic mean $(\bar{y})$ of n samples is given by Equation (3.11)

$$\bar{y} = \frac{\sum y_i}{n} \quad (3.11)$$

The standard deviation of the sample is calculated by Equation (3.12)

$$\sigma^2 = \frac{\sum y_i^2 - (y_i)^2/n}{n-1} \quad (3.12)$$

The lower and the upper confidence intervals are then calculated using the Equation (3.13)

$$CI = \bar{y} \pm \frac{\sigma}{\sqrt{n}} z^* \quad (3.13)$$

Summary of the calculation is given in Table 3.6

Table 3.6: Estimation of 95% confidence interval for the experimental data of subcooled flow boiling heat transfer coefficient of water-ethanol mixture.

n	$\bar{y}$	σ	*Lower limit*	*Upper limit*
285	2199	337.6	2239	2160

3.5 REPEATABILITY

The repeatability results is an important concern in boiling experimentation. To demonstrate the reproducibility of the experimental data, several tests were repeated. Figure 3.7 shows the repeatability of the experiment at mass flux of 76.67 kg/m²-s and inlet temperature of 303 K. The maximum deviation is found to be less than 10%.

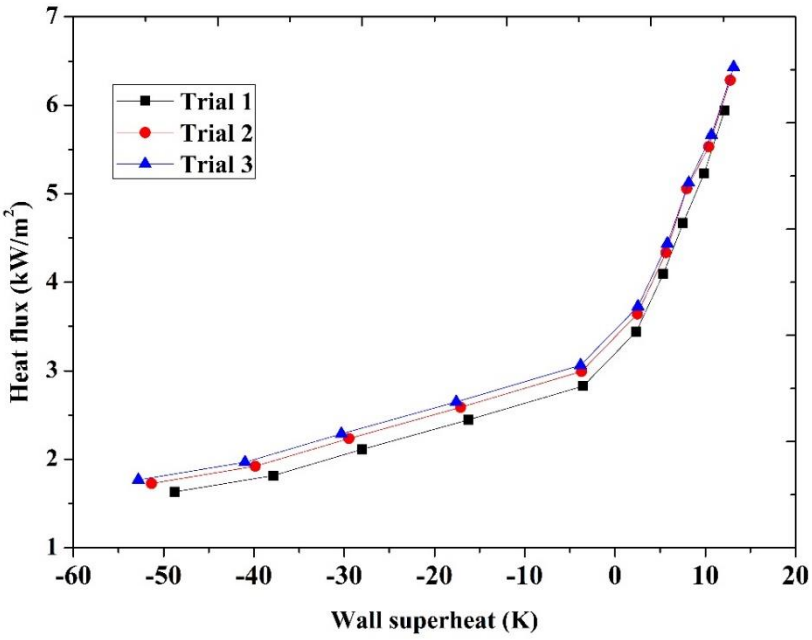

Figure 3.7: Repeatability of the experiment

CHAPTER 4

EXPERIMENTAL RESULTS

The experimental results of forced convection and subcooled flow boiling of water-ethanol mixtures are presented in this chapter. Heat transfer data are correlated based on mechanistic approach.

4.1 PERFORMANCE VALIDATION OF EXPERIMENTAL SETUP

Nusselt number in a rectangular channel for forced convective flow can be calculated by the Churchill and Ozoe equation (Yovanovich and Muzychka, 2004). The characteristics of this region for uniform wall temperature boundary condition are given in Equation (4.1).

$$Nu = \frac{C_0\sqrt{RePr}}{\left[1+\left(\frac{C_0 Pr^{1/6}}{C_\infty}\right)^n\right]^{1/n}} \tag{4.1}$$

$$Pr \to 0 \quad \frac{Nu}{\sqrt{Re}} = 0.564Pr^{0.5} \tag{4.2}$$

$$Pr \to \infty \quad \frac{Nu}{\sqrt{Re}} = 0.339Pr^{0.33} \tag{4.3}$$

C_0 and C_∞ are the coefficients of the right hand side of Equations (4.2) and (4.3), n = 4.598 for the uniform temperature boundary condition. For a parallel rectangular channel, Stephan Equation for Nusselt number is shown in Equation (4.4). This equation is valid for Prandtl numbers varying from 0.1 to 1000 and for laminar flows (Yovanovich and Muzychka, 2004).

$$Nu = 7.55 + \frac{0.024(z^*)^{-1.14}}{1 + 0.035Pr^{0.17}z^{*-0.64}} \tag{4.4}$$

The MAE of experimentally determined Nusselt number for water and those predicted from the correlations is calculated by Equation (4.5). The comparison between predicted and experimental values is shown in Figure 4.1 and 4.2.

$$MAE = \frac{1}{n}\sum\left|\frac{Predicted\ values - Experimental\ values}{Predicted\ values}\right| \times 100 \tag{4.5}$$

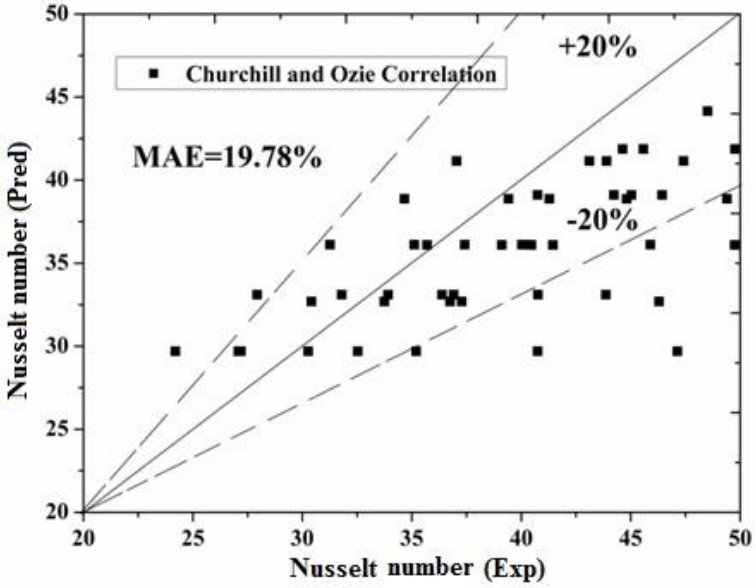

Figure 4.1: Validation of forced convective Nusselt number with Churchill and Ozoe correlation.

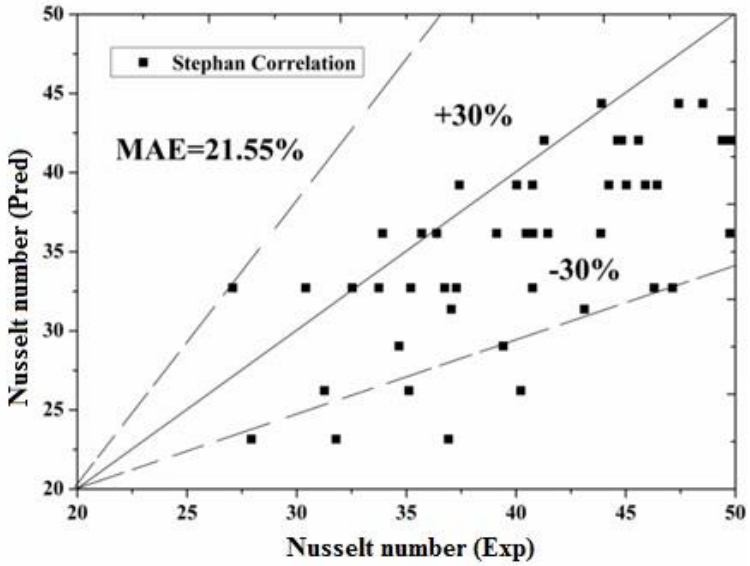

Figure 4.2: Validation of forced convective Nusselt number with Stephan correlation.

Following are the observations made from validation:

- 63% of experimental data are predicted within $\pm 20\%$ error band and 26.15% experimental data are predicted within error band of $\pm 10\%$. The MAE of

experimentally determined Nusselt number for water and those predicted with Churchill-Ozoe correlation is 19.78 %.

- 81.54% of experimental data lie within $\pm 30\%$ error band and 61.54% of experimental data lie within error band of $\pm 20\%$. The MAE of experimentally determined Nusselt number for water and those predicted with Stephan correlation is 21.55%.

The experimental values obtained for water are validated with available subcooled boiling literature correlations. Chen (1966) redeveloped the Rohsenow correlation for subcooled boiling heat transfer coefficient as given by Equation (4.6). Forced convective heat transfer and pool boiling heat transfer coefficients are determined by Equations (4.7) and (4.8). The Reynolds number factor F and the suppression factor S were determined empirically from experimental data as given by Equations (4.9) and (4.11). F is a function of Martinelli parmeter (χ_{tt}) as shown in Equation (4.10). Martinelli parameter is determined from vapour quality (Weiwei and Fang, 2014). Since the presence of vapour quality is negligible during the subcooled boiling, F is chosen as 1 in the present experiment.

$$h_{tp} = Fh_{fc} + Sh_{pb} \tag{4.6}$$

$$h_{fc} = 0.023 Re^{0.8} Pr^{0.4} \frac{k_l}{d_h} \tag{4.7}$$

$$h_{pb} = 0.00122 \frac{k^{0.79} c_P^{0.45} \rho_l^{0.49}}{\sigma_s^{0.5} \mu_l^{0.29} h_{fg}^{0.24} \rho_g^{0.24}} \Delta T_{Sat}^{0.24} \Delta p_{Sat}^{0.75} \tag{4.8}$$

$$F = \left(1 + \frac{1}{(\chi_{tt})^{0.5}}\right)^{1.78} \tag{4.9}$$

$$\chi_{tt} = \left(\frac{1-x}{x}\right)^{0.9} \left(\frac{\rho_g}{\rho_l}\right) \left(\frac{\mu_l}{\mu_g}\right)^{0.1} \tag{4.10}$$

$$S = \frac{1}{1+2.53\times10^{-6} Re^{1.17}} \tag{4.11}$$

Figure 4.3 shows that 81.5% of present experimental data are predicted within $\pm 35\%$ error band and 66.15% are predicted within error band of $\pm 20\%$. The MAE of experimentally determined Nusselt number for water and those predicted with Chen correlation is 26.29 %. The Chen correlation was developed by considering 600 data points

for water. The parameter range were vapour quality from 0.01 to 0.71, mass flux from 54 to 4070 kg/m^2-s, heat flux from 6.3 to 2397.5 kW/m^2, and saturation pressure from 0.055 to 3.48 MPa. This is the reason for deviation of the present experimental data from those data predicted from the Chen correlation. The other reason for deviation is the presence of Reynolds number factor F in the Chen correlation.

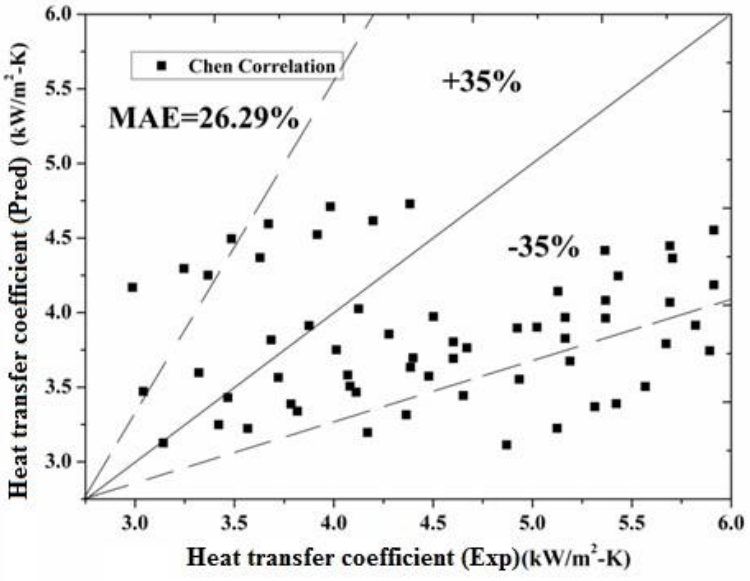

Figure 4.3 : Validation of subcooled flow boiling heat transfer coefficient values with Chen correlation.

Gungor and Winterton (1986) suggested Cooper correlation for pool boiling heat transfer component in the Equation (4.6). Cooper correlation is given by Equation (4.12). S was calculated by using Equation (4.13). Chen correlation was modified by introducing boiling number (Bo) in the enhancement factor E as shown in Equation (4.14).

$$h_{pb} = 55\left(\frac{P}{P_{cr}}\right)^{0.12}\left[-log_{10}\left(\frac{P}{P_{cr}}\right)\right]^{-0.55} M^{-0.5} q''^{0.67} \quad (4.12)$$

$$S = \frac{1}{1+1.15\times10^{-6}E^2Re^{1.17}} \quad (4.13)$$

$$E = 1 + 24000Bo^{1.16} \quad (4.14)$$

h_{tp} and h_{fc} are calculated by Equation (4.6) and Equation (4.7) respectively. Figure 4.4 shows that 78.64% of present experimental data are predicted within $\pm 20\%$ error band

and 44.62% are predicted within $\pm 10\%$ error band. The MAE of experimentally determined Nusselt number for water and those predicted with Gungour and Winterton correlation is 16.83 %. The Boiling number in Equation (4.14) leads to relatively lower deviation when compared with that of Chen correlation. The Gungor and Winterton correlation was developed for 4300 data points for water, R11, R12, R113, R114 and Ethylene Glycol for various tube diameters, orientation of flow, mass flux, heat flux, saturation pressure and vapour quality. This is the reason for deviation of the present experimental data from those data predicted from the correlation.

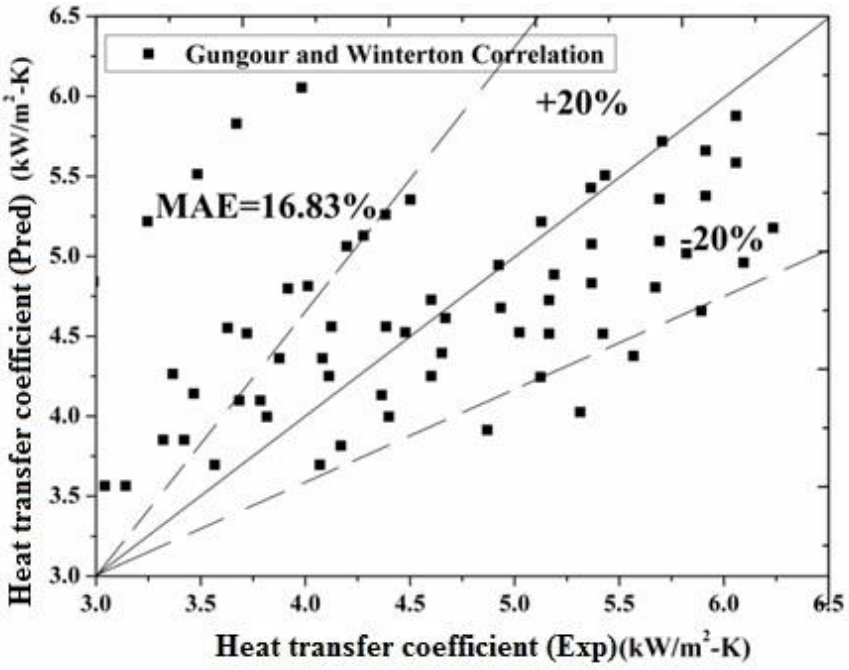

Figure 4.4 : Validation of subcooled flow boiling heat transfer coefficient values with Gungour and Winterton correlation.

Kandlikar (1998) proposed subcooled boiling correlations for water and is given by Equation (4.15).

$$\frac{h_{tp}}{h_{fc}} = 1058 Bo^{0.7} F \tag{4.15}$$

h_{fc} is calculated by the Equation (4.7). Figure 4.5 shows that 90.76% of experimental data are predicted within $\pm 30\%$ error band and which 75.92% of experimental data are

predicted within $\pm 20\%$ error band. The MAE of experimentally determined Nusselt number for water and those predicted with Kandlikar correlation is 18.78%.

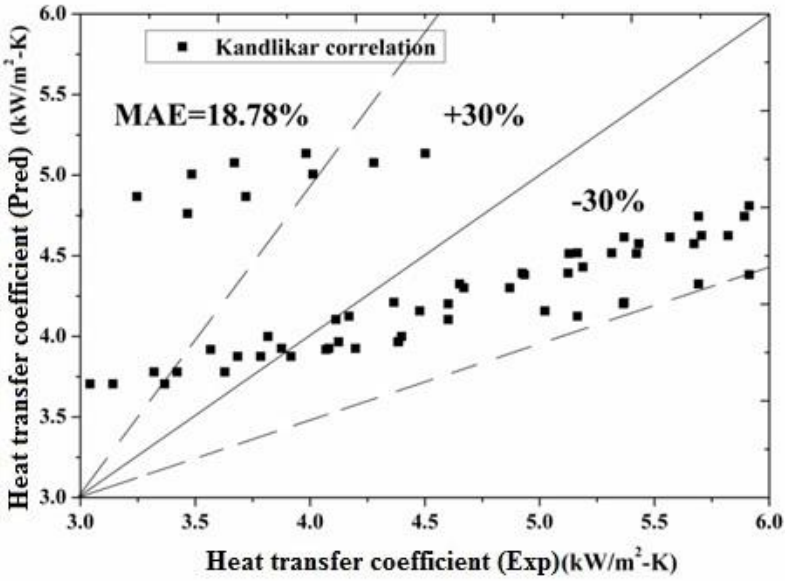

Figure 4.5: Validation of subcooled flow boiling heat transfer coefficient values with Kandlikar correlation.

Liu and Winterton (1991) proposed a power-type addition model for the prediction of subcooled flow boiling heat transfer. Their experiments were carried out in tubes and annuli and covered a range of mass flux from 12.4 to 8180 kg/m^2-s, Pressure from 0.05 to 20 MPa, and T_{sub} from 0 to 173℃. The correlation for subcooled flow boiling heat transfer coefficient is expressed as given by Equation (4.16). S is calculated by using Equation (4.17).

$$h_{tp} = \sqrt{F{h_{fc}}^2 + \left(S h_{pb} \frac{T_{Wall} - T_{Sat}}{T_{Wall} - T_{Sat}}\right)^2} \tag{4.16}$$

$$S = \frac{1}{1 + 0.0055 F^{0.1} Re_l^{0.16}} \tag{4.17}$$

h_{pb} is calculated by Equation (4.12). Figure 4.6 shows that 69.23% of present experimental data are predicted within $\pm 20\%$ error band and 38.46% are predicted within error band of $\pm 10\%$. The MAE of Liu-Winterton correlation is 22.69% while predicting the experimental data.

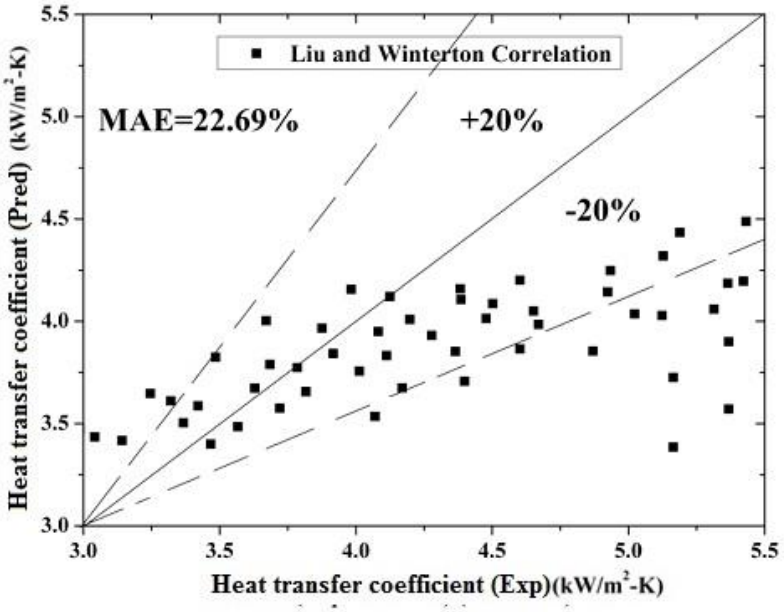

Figure 4.6 : Validation of subcooled flow boiling heat transfer coefficient values with Liu and Winterton correlation.

The Gungour –Winterton and Kandlikar correlations predicted the experimental data better when compared with that of Chen and Liu-Winterton correlations. This is due to the presence of Boiling number in Gungour-Winterton and Kandlikar correlations. The boiling number plays a vital role during subcooled flow boiling heat transfer and it also proved to be significant while predicting the subcooled flow boiling heat transfer coefficient by heat transfer approach which is given in section 4.5. Boiling number is defined as the ratio of heat flux to heat of evaporation. When heat flux increases, the active nucleation sites increase. Isolated bubbles are formed on active nucleation sites during nucleate boiling. After bubble inception, the superheated liquid layer which is pushed outward mixes with the subcooled liquid leading to agitation (Minxia Li et al. 2012). The heat flux is considered by combining the effect of transient conduction around nucleation sites and micro-layer evaporation below the bubbles. The departed bubble acts as an energy carrier by removing the heat from the channel wall surface. Hence Boiling number is more significant in the subcooled boiling region.

The deviation of the present experimental data from those predicted using correlations is also attributed to non-uniform temperature distribution in cold plate,

assumption of one dimensional temperature distribution to calculate heat flux and non possibility of making the experimental system air tight.

4.2 BOILING CURVE

The variation of heat flux with wall superheat for water at inlet temperature=303 K is shown in Figure 4.7 (a).

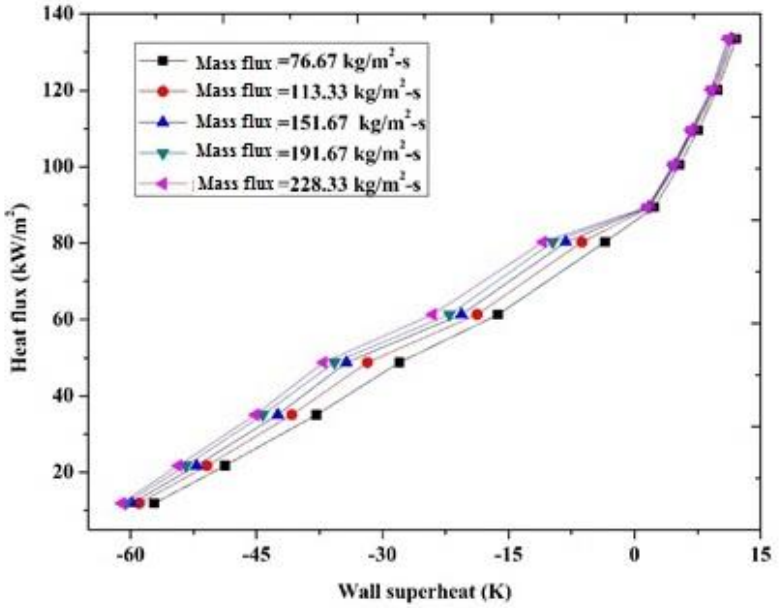

Figure 4.7(a): Boiling curves for water at inlet temperature=303 K.

The heat flux increases with increase in wall superheat for both forced convection and subcooled boiling region. But the increase in heat flux is higher in the subcooled boiling region. The boiling curves almost merge into a single curve for different values of mass fluxes in the subcooled boiling region. The increase in mass flux decreases the wall temperature in forced convection region but the wall temperature does not vary significantly at subcooled boiling region. Decrease in wall temperature decreases the wall superheat. This shows that increase in mass flux has negligible influence on heat transfer in the subcooled flow boiling region. Figure 4.7 (b) shows the variation of heat flux with wall super heat for water-ethanol mixture of ethanol volume fraction 25%. It can be observed that the trend obtained for 25% ethanol volume fraction are similar to that of

water. The boiling curves for water-ethanol mixtures of different ethanol volume fraction are shown in APPENDIX B.

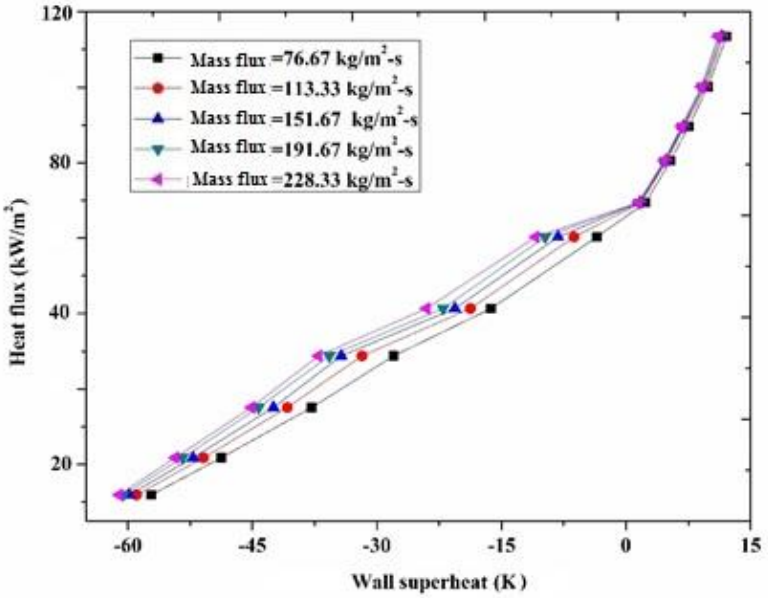

Figure 4.7 (b): Boiling curves for water-ethanol mixture of ethanol volume fraction 25% at inlet temperature=303 K.

4.3 EFFECT OF HEAT FLUX AND MASS FLUX ON HEAT TRANSFER COEFFICIENT

Figure 4.8 (a) shows the variation of heat transfer coefficient of water with wall super heat for different values of mass fluxes. The heat transfer coefficient increases with increase in heat flux and mass flux in both the regions. The wall temperature decreases with increase in mass flux and the heat transfer coefficient increases when wall temperature reduces.

The heat transfer coefficient increases with increase in heat flux in the forced convection region. But the increase is not significant because, the velocity (mass flux) convects the heat through the fluid which is conducted from wall of the channel. But the effect of mass flux is not significant to increase heat transfer coefficient in subcooled boiling region. This is because convective contribution does not play a significant role on the heat transfer due to establishment of vapour turbulent flow. Higher mass flux

contributes towards convective mode of heat transfer, but the convective heat transfer is dominated by vapour turbulence in the flow.

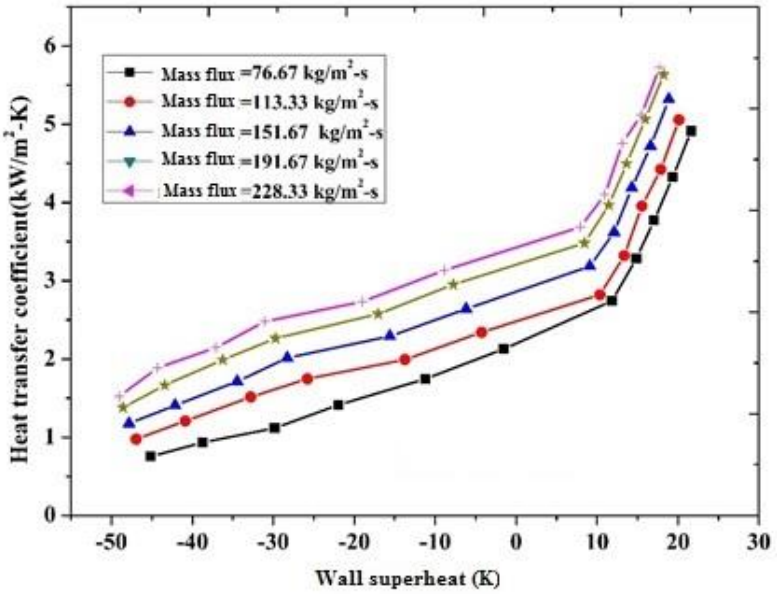

Figure 4.8 (a): Variation of heat transfer coefficient with wall superheat for water at inlet temperature=303 K

When heat flux increases, the vapour bubble is subjected to variation of surface tension force, thus drags the adjacent warm layer of fluid causing the flow of bubble from hot region to cold region. This causes local vapour momentum forces to act along the flow. These local vapour momentum forces dominate the convective mode of heat transfer to increase the heat transfer coefficient at higher heat flux. Figure 4.8(b) shows the variation of heat transfer coefficient with wall superheat for water-ethanol mixture of ethanol volume fraction 25%. It can be seen that the similar trends are obtained for 25% ethanol volume fraction as that of water. Similar trends are also obtained for water-ethanol mixtures of different volume fraction which are shown in APPENDIX B.

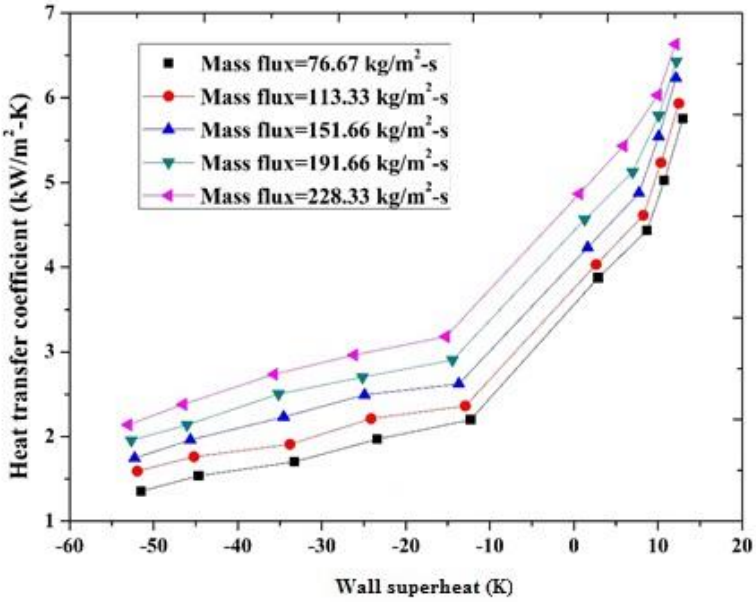

Figure 4.8 (b): Variation of heat transfer coefficient with wall superheat for water ethanol mixture of ethanol volume fraction 25% at inlet temperature =303 K.

4.4 EFFECT OF INLET TEMPERATURE ON HEAT TRANSFER COEFFICIENT

Figures 4.9 (a) and (b) show the variation of forced convective heat transfer coefficient with inlet temperature for water and water-ethanol mixture of ethanol volume fraction 25%. Figures 4.9 (c) and (d) show the variation of subcooled flow boiling heat transfer coefficient with inlet temperature for water and water-ethanol mixture of ethanol volume fraction 25%. It is observed that the forced convective heat transfer and subcooled flow boiling coefficients decrease with increase in inlet temperature. This is attributed to the: i) increase in thickness of thermal boundary layer as shown in Figure 4.10. Higher the thickness, lower is the potential to absorb heat from the channel wall. The thickness of thermal boundary layer (δ_{Th}) is calculated by Equation (4.18)

$$\delta_{Th} = k\frac{(T_W - T_f)}{q"} \qquad (4.18)$$

ii) The surface tension decreases with increase in temperature. During subcooled boiling, increase in inlet temperature causes lesser vapour bubble formation, thus reducing the vapour turbulence and vapour momentum forces. Hence the vapour bubble agitation and

heat transfer decreases with increase in inlet temperature. Similar trends are obtained for forced convective and subcooled flow boiling heat transfer coefficients of water-ethanol mixtures of various ethanol volume fractions which are shown in APPENDIX B.

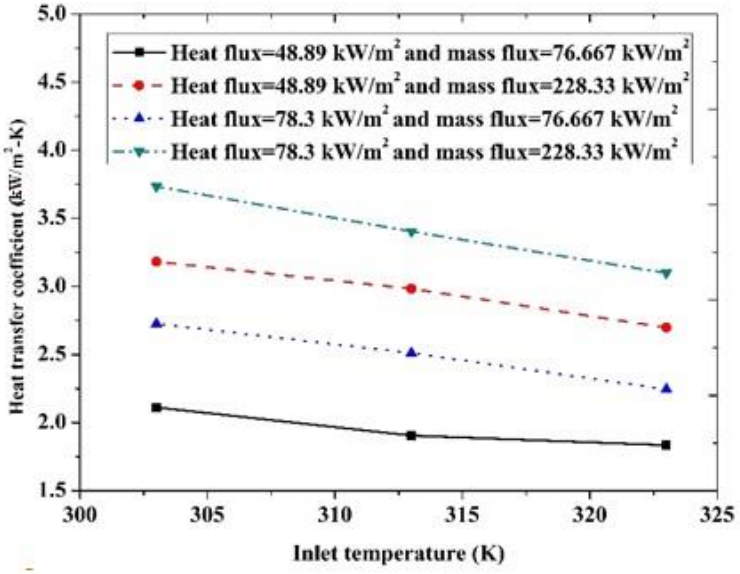

Figure 4.9 (a): Variation of forced convective heat transfer coefficient with inlet temperature for water

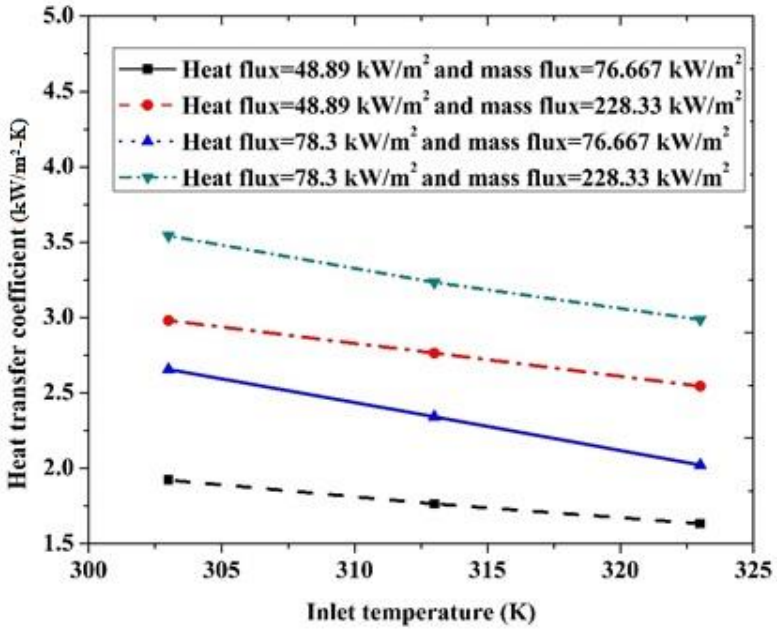

Figure 4.9 (b): Variation of forced convective heat transfer coefficient with inlet temperature for water-ethanol mixture of ethanol volume fraction 25%.

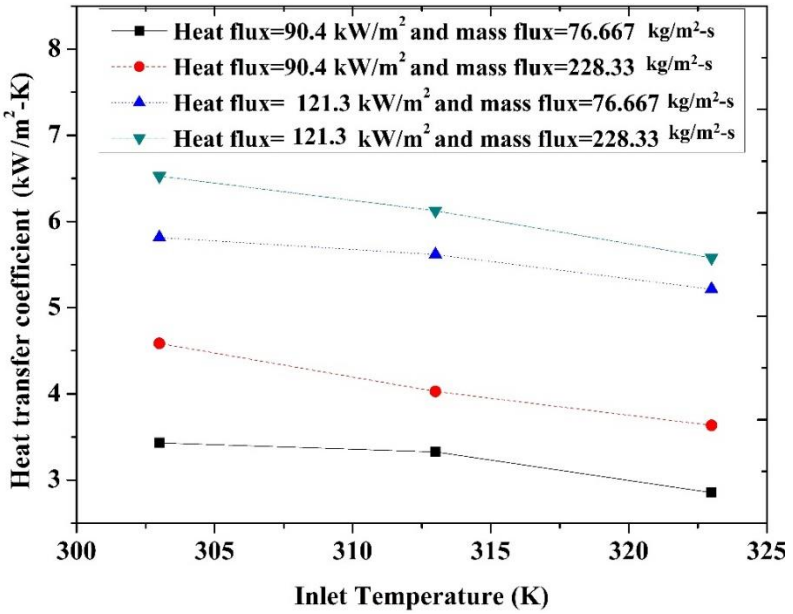

Figure 4.9(c): Variation of subcooled boiling heat transfer coefficient with inlet temperature for water.

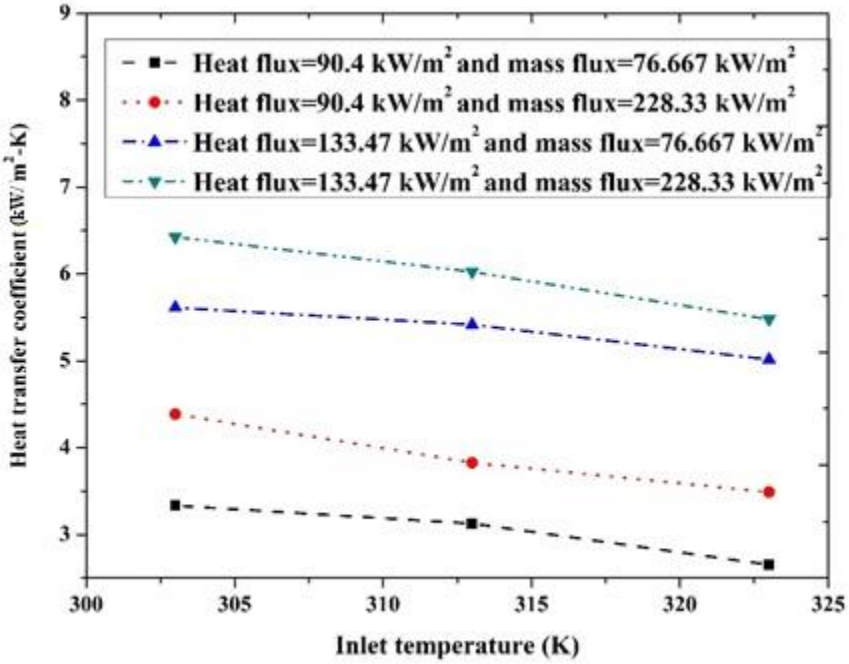

Figure 4.9(d): Variation of subcooled boiling heat transfer coefficient with inlet temperature for water-ethanol mixture of ethanol volume fraction 25%.

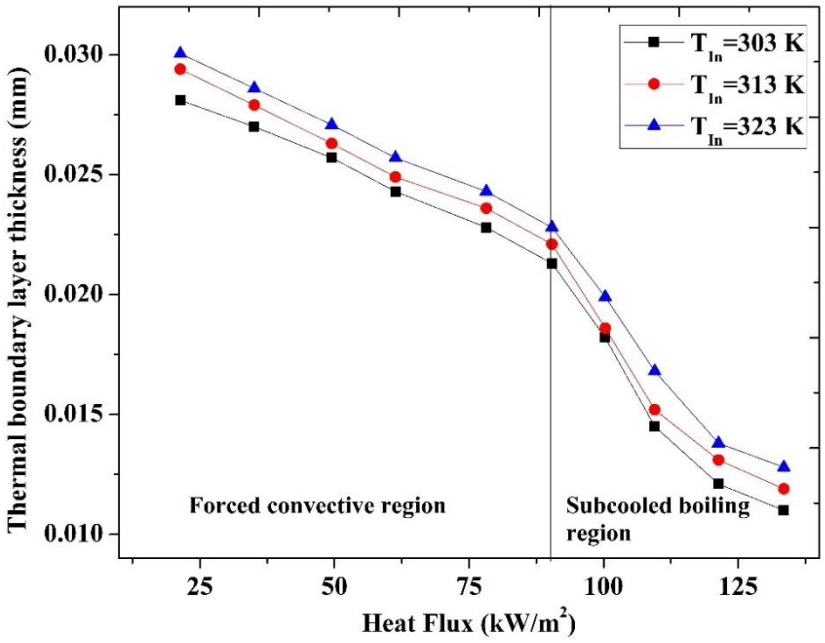

Figure 4.10: Variation of thermal boundary layer thickness with heat flux at different inlet temperature.

4.5 EFFECT OF ETHANOL VOLUME FRACTION ON HEAT TRANSFER COEFFICIENT

Figure 4.11 shows the variation of forced convective heat transfer coefficient with ethanol volume fraction at various inlet temperatures. The surface tension, thermal conductivity and thermal capacity decrease with increase in ethanol volume fraction. This results in decrease in heat transfer coefficient of the mixture with increase ethanol addition.

The variation of subcooled flow boiling heat transfer coefficient with ethanol volume fraction at various inlet temperatures at heat flux of 90.4 kW/m^2 is shown in Figure 4.12(a). This particular value of heat flux is so chosen that the subcooled boiling takes place for both water and ethanol. If the heat flux is lower than 90.4 kW/m^2, subcooled boiling of water will not commence, instead it will be in forced convective region. If the heat flux is higher than 90.4 kW/m^2, saturated boiling of ethanol will be initiated.

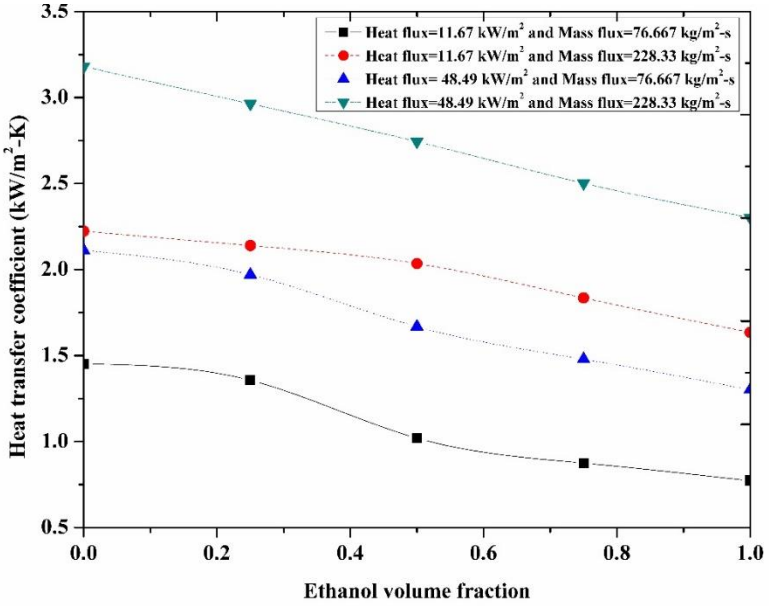

Figure 4.11: Variation of forced convective heat transfer coefficient with ethanol volume fraction.

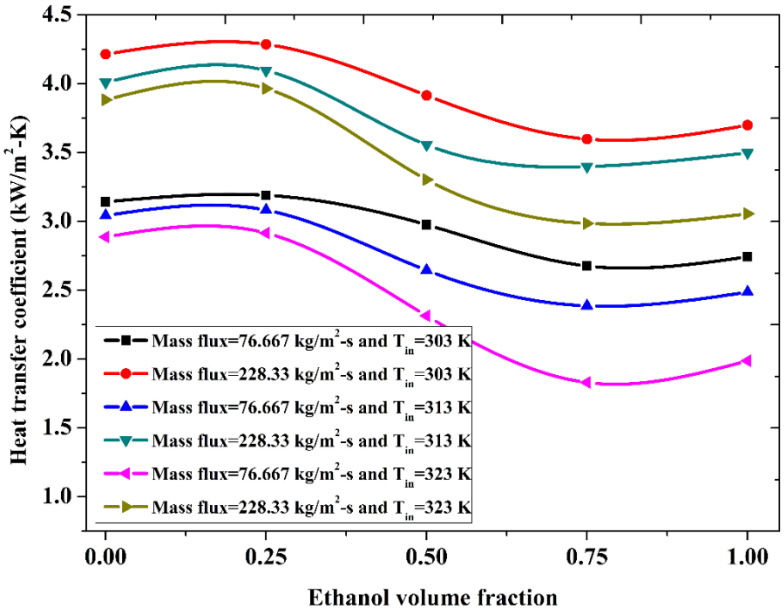

Figure 4.12 (a): Variation of subcooled flow boiling heat transfer coefficient with ethnaol volume fraction.

It is observed that the heat transfer coefficient increases with the addition of ethanol to water inititially upto 25% ethanol volume fraction, but with further addition of ethanol, the

heat transfer coefficient reduces. At 25% volume fraction, maximum difference between dew point temperature (T_d) and bubble point temperature (T_b) is observed as shown in Figure 4.12(b). This indicates that the liquid vapour coexisting region is widest at this ethanol volume fraction (Chin et al. 2012).

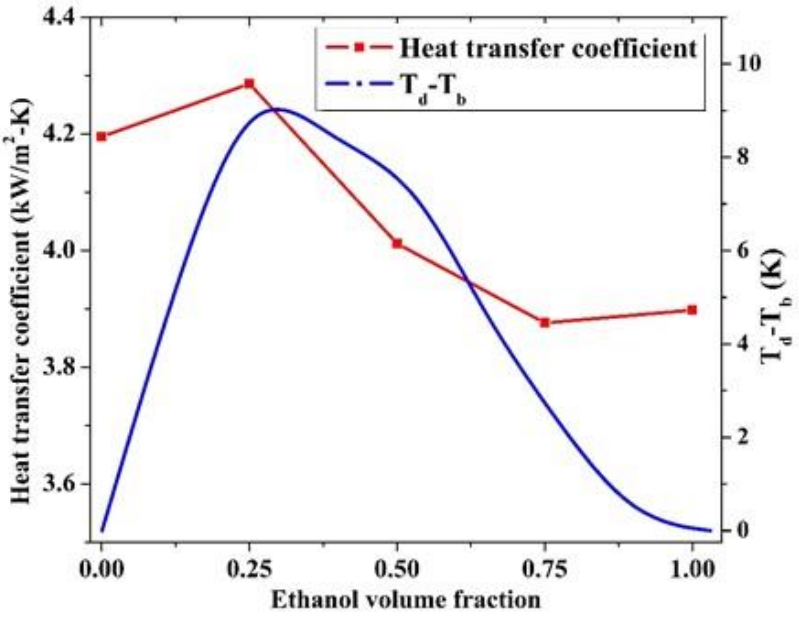

Figure 4.12 (b): Variation of subcooled flow boiling heat transfer coefficient and ($T_d - T_b$) with ethanol volume fraction.

During the onset of boiling, more volatile component of the mixture near the channel wall surface induces concentration and temperature gradients in the micro layer region along the vapour-liquid interface. The induced gradients cause the Marangoni force to pull the bulk liquid towards the liquid vapour interface causing micro layer agitation and thus increasing the heat transfer coefficient. The reason for decrease in heat transfer coefficient with the addition of ethanol to water at 50% and 75% ethanol volume fraction is supported with the bubble dynamic data given in section 6.4.

The components in the liquid mixture have different evaporation rates. The lower boiling component escapes from the liquid-vapor interface and the higher boiling component accumulates near the liquid-vapor interface and the layer of the concentration gradient forms near this interface (Minxia et al. 2012, 2013). Because of two phase and convective heat transfer, the concentration gradient layer exists not only at the surface of

the bubble but also at the liquid - vapor interface at the bottom wall. During the partial developed boiling, the mass diffusion affects the heat transfer coefficient of mixture during the subcooled flow boiling process. The lower boiling component in the bulk liquid has to pass through the diffusion layer before arriving at the interface. Therefore, for a mixture, heat transfer coefficients are affected not only by the interaction between the two phase flow and the convective heat transfer, but also by mass transfer resistance inside the diffusion layer. The concentration gradient near the interface of evaporation is low because the evaporating process is less vigorous. Moreover, a bubble transitioning from the liquid to the vapor phase can cause agitation that decreases the effect of mass diffusion.

4.6 CORRELATION DEVELOPMENT BASED ON HEAT TRANSFER APPROACH

To arrive at correlation for subcooled boiling heat transfer, it is reasonable to start from physical properties and parameters that characterize the heat transfer process based on some assumptions. Following are the assumptions made for developing new correlation:

- The present experiment is carried out for constant hydraulic diameter, but the hydraulic diameter is chosen as a geometric property.
- Effects of inlet temperature and volume fractions are considered from the thermodynamic properties and thermo physical properties which correspond to the average fluid temperature of the fluid.
- The dimensionless parameters which do not contribute for reducing mean absolute error (MAE) represented by Equation (4.19) are neglected.

$$MAE = \frac{1}{n}\sum \left|\frac{Thoretical\ values - Experimental\ values}{Experimental\ values}\right| \times 100 \qquad (4.19)$$

Mixture properties like liquid density, specific heat, thermal diffusivity are calculated using simple mixing rule. Thermal conductivity, liquid viscosity and surface tension are calculated by Flippov (1968), McLaughlin Equation (Ratliff et al. 1971) and Macleoad-Sudgen correlation (Deam and Mattox, 1970) represented in the Equation (4.20), Equation (4.21) and Equation (4.22) respectively.

$$\frac{k_m - k_i}{k_j - k_i} = C m_{fj}^2 - m_{fi}(1 - C) \quad (4.20)$$

$$ln(\mu_m) = x_i ln\mu_i + x_j ln\mu_j \quad (4.21)$$

$$\sigma_m^{1/4} = Pa_j(\rho_{Lm} x_j - \rho_{lv} y_j) \quad (4.22)$$

If the value of mixture constant C in Equation (4.20) is not available, then C can be chosen as 0.72 (Robert et al. 1972).

The subcooled flow boiling heat transfer coefficient is a function of $\rho, u, d_h, \mu, k, \Delta T_{fw}, C_P, h_{fg}, \sigma_s \; and \; q"$ i.e, $h = f(\mu, \rho, u, d_h, k, \Delta T_{fw}, C_P, h_{fg}, q", \sigma_s)$ .The properties and parameters chosen are combined as dimensionless numbers by Buckingham's π-theorem. These dimensionless numbers are:

$\pi_1 = \frac{k\Delta T_{fw}}{\rho u^3 d_h}$, $\pi_2 = \frac{C_P \Delta T_{fw}}{v^2}$, $\pi_3 = \frac{\sigma_s}{\rho u^2 d_h}$, $\pi_4 = \frac{h_{fg}}{v^2}$, $\pi_5 = \frac{q"}{\rho u^3}$,$\pi_6 = \frac{h\Delta T_{fw}}{\rho u^3}$ and $\pi_7 = \frac{\mu}{\rho u d_h}$.

The independent dimensionless numbers $(\pi_1, \pi_2, \pi_3, \pi_4, \pi_5 and \; \pi_7)$ which significantly influence the dependent dimensionless number (π_6) are chosen. The present correlation is obtained by regression analysis. In the first step, for each of the independent dimensionless number, an Equation (4.23) is formed.

$\pi_6 = a_1 {\pi_1}^{b_1}$, $\pi_6 = a_2 {\pi_2}^{b_2}$, $\pi_6 = a_3 {\pi_3}^{b_3}$, $\pi_6 = a_4 {\pi_4}^{b_4}$, $\pi_6 = a_5 {\pi_5}^{b_5}$ and $\pi_6 = a_7 {\pi_7}^{b_7}$ (4.23)

Of all the different independent dimensionless numbers employed in the analysis the one which contains the most essential dimensionless number yields the smallest MAE. It is found that $\pi_6 = a_5 {\pi_5}^{b_5}$ has smallest MAE of 25.54%. So π_5 is considered to be the first essential dimensionless number. In the second step, each of the remaining dimensionless numbers are multiplied with π_6 and Equation (4.24) is formed.

$$\pi_6 = a_{5,1}(\pi_5 \pi_1)^{b_{5,1}} , \quad \pi_6 = a_{5,2}(\pi_5 \pi_2)^{b_{5,2}} , \quad \pi_6 = a_{5,3}(\pi_5 \pi_3)^{b_{5,3}} ,$$

$$\pi_6 = a_{5,4}(\pi_5 \pi_4)^{b_{5,4}} \quad \pi_6 = a_{5,7}(\pi_5 \pi_7)^{b_{5,7}} \quad (4.24)$$

It is found that $\pi_6 = a_{5,4}(\pi_5 \pi_4)^{b_{5,4}}$ has smallest MAE of 10.43%. So π_4 is considered to be the second essential dimensionless number. In next steps, the MAE is reduced by introducing next set of independent dimensionless numbers.

$$\pi_6 = a_{5,4,3}(\pi_5\pi_4\pi_3)^{b_{5,4,3}} \quad (4.25)$$

$$\pi_6 = a_{5,4,3,1}(\pi_5\pi_4\pi_3\pi_1)^{b_{5,4,3,1}} \quad (4.26)$$

MAE obtained while predicting π_6 from Equation (4.25) and Equation (4.26) are 9.71% and 8.8 % respectively. It is found that π_3 and π_1 are the third and fourth essential dimensionless numbers. Introduction of further dimensionless numbers (π_2 *and* π_7) did not reduce MAE and hence they are neglected. Figures 4.13 to 4.16 show the variation of π_6 due to addition of independent dimensionless numbers. Final form of the present correlation is given in Equation (4.27).

$$\frac{h\Delta T_{fw}}{\rho u^3} = 2.319\left(\frac{k\Delta T_{fw}}{\rho u^3 d_h}\right)^{0.425}\left(\frac{\sigma_s}{\rho u^2 d_h}\right)^{0.105}\left(\frac{h_{fg}}{u^2}\right)^{0.0135}\left(\frac{q''}{\rho u^3}\right)^{0.627} \quad (4.27)$$

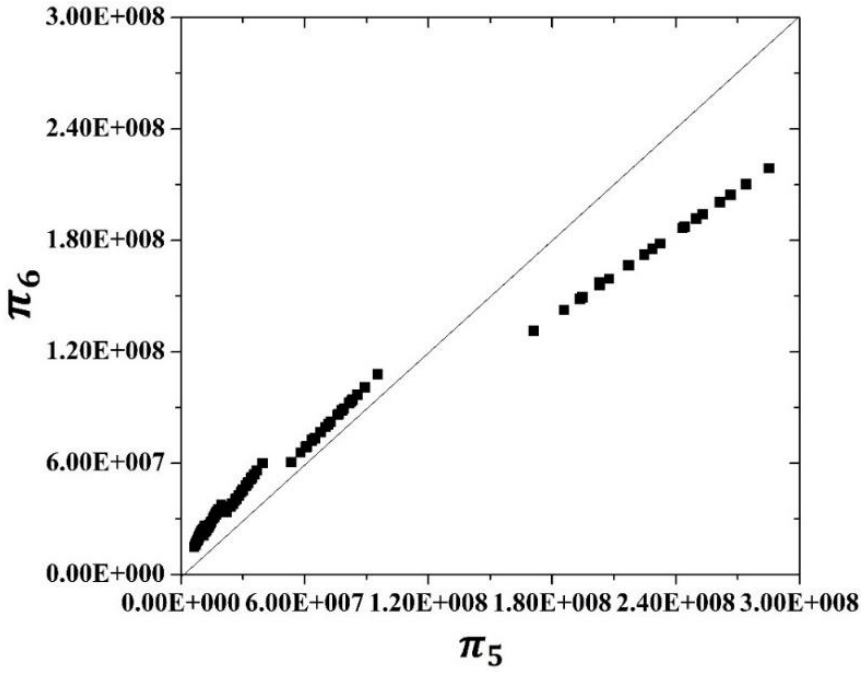

Figure 4.13: $\pi_6\ vs.\ \pi_5$

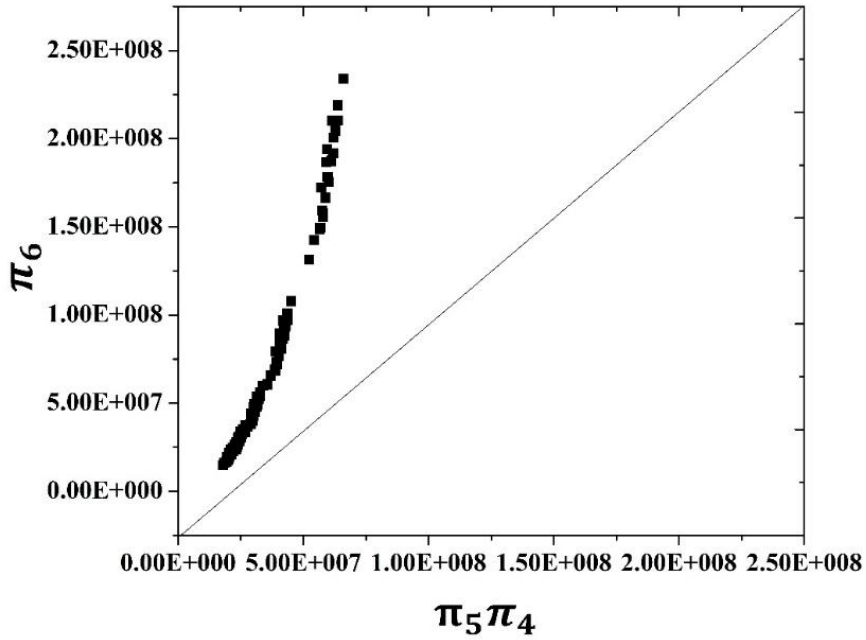

Figure 4.14: $\pi_6\ vs.\ \pi_5\ \pi_4$

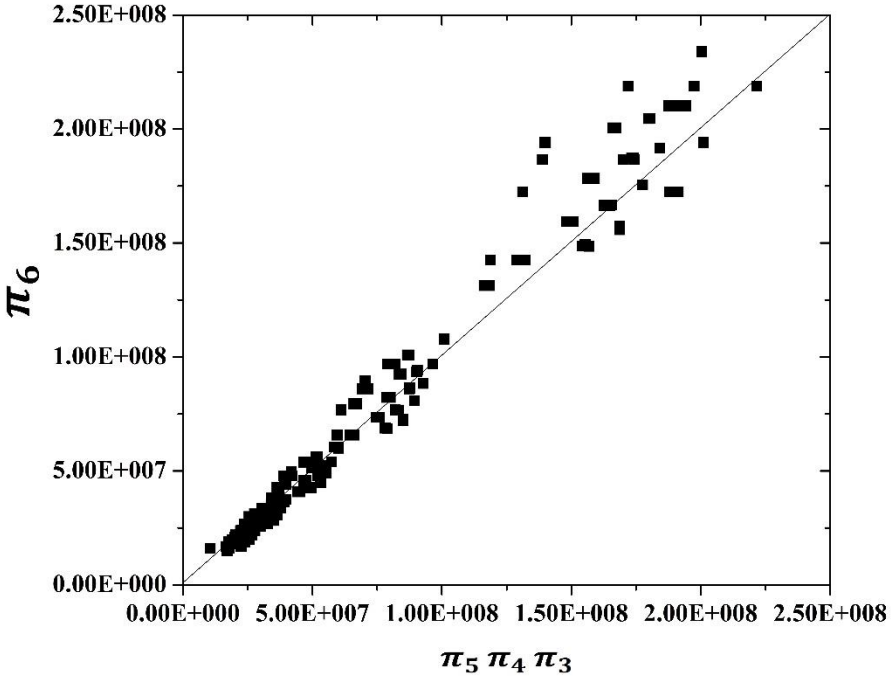

Figure 4.15: $\pi_6\ vs.\ \pi_5\ \pi_4\ \pi_3$

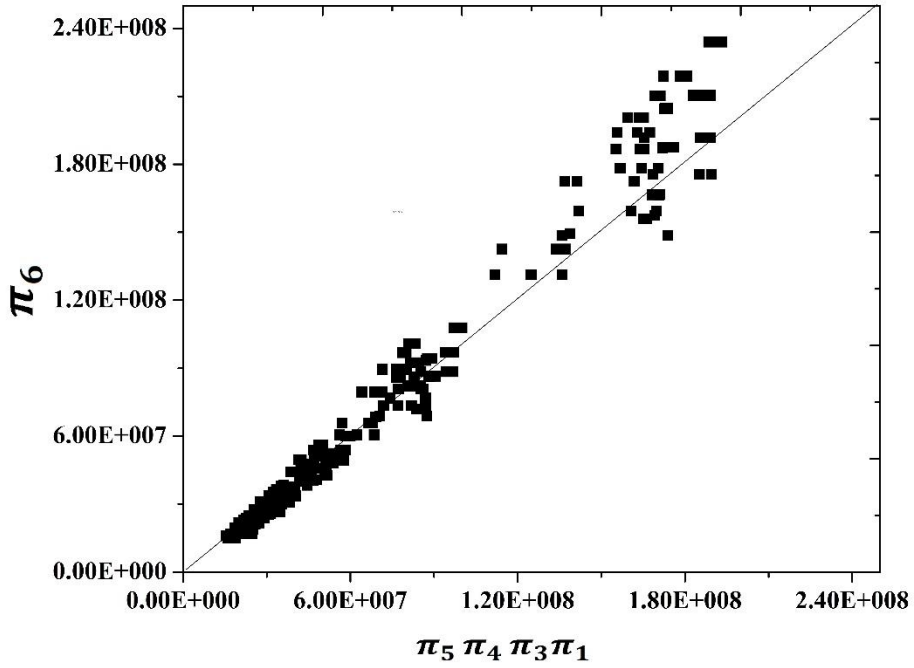

Figure 4.16: $\pi_6\ vs.\ \pi_5\,\pi_4\,\pi_3\pi_1$

Dimensionless number $\pi_3 = \frac{\sigma_s}{\rho u^2 d_h}$ is called $\left(\frac{1}{\text{Channel Weber number}}\right)$. When $\pi_4 = \frac{h_{fg}}{u^2}$ multiplied and divided by $m/2$ (where m is mass of liquid), a non dimensional number called $\left(\frac{0.5}{\text{Two phase Eckert number}}\right)$ is obtained. Eckert number expresses the relation between overall heat transfer in the channel and fluid kinetic energy. The Equation (4.28) is obtained by simplifying Equation (4.27).

$$\frac{h\Delta T_{fw}}{\rho u^3} = 2.319\left(\frac{k\Delta T_{fw}}{\rho u^3 d_h}\right)^{0.425}\left(\frac{1}{We_{ch}}\right)^{0.105}\left(\frac{0.5}{Er_{tp}}\right)^{0.0135}\left(\frac{q"}{\rho u^3}\right)^{0.627} \quad (4.28)$$

$$\frac{h\Delta T_{fw}}{\rho u^3} = 2.3\left(\frac{k\Delta T_{fw}}{\rho u^3 d_h}\right)^{0.425}\left(\frac{1}{We_{ch}}\right)^{0.105}\left(\frac{1}{Er_{tp}}\right)^{0.0135}\left(\frac{q"}{\rho u^3}\right)^{0.627} \quad (4.29)$$

$\frac{h\Delta T_{fw}}{\rho u^3}$ and $\left(\frac{k\Delta T_{fw}}{\rho u^3 d_h}\right)^{0.425}$ in Equation (4.29) are written as $\frac{q"}{\rho u^3}$ and $\left(\frac{q"}{\rho u^3 Nu_{scb}}\right)^{0.425}$ Where $\frac{k\Delta T_{fw}}{d_h} = \frac{h\Delta T_{fw}}{Nu_{scb}} = \frac{q"}{Nu_{scb}}$

$$\frac{q"}{\rho v^3} = 2.3\left(\frac{1}{We_{ch}}\right)^{0.053}\left(\frac{1}{Er_{tp}}\right)^{0.0135}\left(\frac{q"}{\rho u^3 Nu_{scb}}\right)^{0.425}\left(\frac{q"}{\rho u^3}\right)^{0.627} \quad (4.30)$$

$$Nu_{scb}{}^{0.425} = 2.3\left(\frac{1}{We_{ch}}\right)^{0.105}\left(\frac{1}{Er_{tp}}\right)^{0.0135}\left(\frac{q"}{\rho u^3}\right)^{0.425}\left(\frac{q"}{\rho u^3}\right)^{0.627}\left(\frac{\rho u^3}{q"}\right) \quad (4.31)$$

$$Nu_{scb}{}^{0.425} = 2.3\left(\frac{1}{We_{ch}}\right)^{0.105}\left(\frac{1}{Er_{tp}}\right)^{0.0135}\left(\frac{q"}{\rho u^3}\right)^{0.052} \quad (4.32)$$

$$Nu_{scb} = 2.3\left(\frac{1}{We_{ch}}\right)^{0.247}\left(\frac{1}{Er_{tp}}\right)^{0.032}\left(\frac{q"}{\rho u^3}\right)^{0.122} \quad (4.33)$$

$\left(\frac{q"}{\rho u^3}\right)^{0.122}$ in Equation (4.33) is written as $\left(\frac{h_{fg}q"}{h_{fg}\rho u^3}\right)^{0.122} = \left(\frac{q"h_{fg}}{\rho u h_{fg}v^2}\right)^{0.122} = \left(\frac{0.5Bo}{Er_{tp}}\right)^{0.122}$,Where $Bo = \frac{q"}{\rho u h_{fg}}$ is called as Boiling number.

Final form of the present correlation is expressed by Equation (4.34).

$$Nu_{scb} = 5.82\frac{Bo^{0.122}}{We_{ch}{}^{0.247}Er_{tp}{}^{0.154}} \quad (4.34)$$

4.6.1 Significance of dimensionless number $\boldsymbol{\pi_3 = \frac{\sigma_s}{\rho u^2 d_h}}$

Weber number plays an important role in flow boiling heat transfer (Kandlikar et al. 2005). When the bubble is formed in the active nucleation sites, it coheres at the surface of channel wall due to surface tension between the channel wall-vapour interfaces. Surface energy of channel wall tends to pull the molecules of local vapour which is in the form of bubbles causing wetting of the channel surface known as wettability. The wetting of surface is dependent on the contact angle between the channel wall surface (solid-liquid interface) and the bubble. When contact angle increases, the wettability decreases and bubble departs from the surface.

At higher mass flux and heat flux, surface tension between the channel wall and the vapour decreases due to decrease in surface energy. Surface tension in the vapour-liquid interface increases in order to overcome the loss of surface tension between channel wall-vapour interfaces. This attracts the surface of the bubble towards the liquid causing increase in vapor-liquid interface pressure and buoyancy of the bubble. The role of inertial force of the fluid is high for convective heat transfer. In subcooled boiling heat transfer the convective heat transfer is not significant when compared to heat transfer due to agitation and evaporation (Nilanjana et al. 2005). Therefore the inertial force is not significant for

overall heat transfer in the subcooled boiling region and the surface tension force dominates over the inertial force of the liquid. Due to formation of the bubbles, overall heat transfer is reduced because of thin vapour layer of bubbles providing thermal resistance to heat transfer. Hence surface tension of the vapour-liquid interface must be higher than the inertial force of the liquid for bubble to depart at faster rate. Departed bubble is an energy carrier and increases the evaporative heat transfer. The adjacent layers of liquid molecules fill the site from where the bubble has departed.

4.6.2 Significance of dimensionless number $\boldsymbol{\pi_4 = \frac{h_{fg}}{u^2}}$

The dimensionless number $\pi_4 = \frac{h_{fg}}{u^2}$ can be represented in the form $\pi_4 = \frac{0.5}{Er_{tp}}$ .Eckert number is the ratio of overall heat transfer to the kinetic energy of the liquid (Gschwendtner, 2004). When the wall temperature exceeds the saturation temperature of the liquid the heat added will acquire sufficient energy to overcome the intermolecular forces of the molecules. This causes change of phase of local liquid. The clusters of molecules escape as vapour in the form of bubbles. This increases the molar latent heat of vaporization because more heat is supplied to break the intermolecular forces of liquid. Increased latent heat increases the wall temperature and thus decreases the difference between wall temperature and fluid temperature.

4.6.3 Significance of dimensionless number $\boldsymbol{\pi_5 = \frac{q''}{\rho u^3}}$

The dimensionless number $\frac{q''}{\rho u^3}$ is expressed as the ratio of Boiling number to two phase Eckert number $\left(\frac{0.5Bo}{Er_{tp}}\right)$. Boiling number is defined as the ratio of heat flux to heat of evaporation. When heat flux increases, the active nucleation sites also increase. Addition of new nucleation sites influences the rate of heat transfer from the channel wall surface. In the earlier studies, it is noted that the density of active nucleation sites increase approximately as the square of the heat flux. Isolated bubbles are formed on active nucleation sites during nucleate boiling. After bubble inception, the superheated liquid layer which is pushed outward mixes with the subcooled liquid. The bubbles act like a pump in removing hot liquid from the surface and replacing it with subcooled adjacent

liquid (Kandlikar et al. 1999). Heat flux is considered by combining the effect of transient conduction around nucleation sites and micro-layer evaporation below the bubbles.

At higher velocity, fluid kinetic energy increases and the active nucleation sites reduce because the heat is carried away by convection due to decrease in agitation and evaporation. This shows that increase in heat transfer is not much significant and heat flux has a major role in heat transfer than velocity. Hence $\pi_5 = \frac{q''}{\rho u^3}$ is significant in heat transfer mechanism. The latent heat of vaporization and surface tension are governed by heat flux. Hence it can be concluded that heat flux is more significant when compared to surface tension and latent heat of vaporization.

4.6.4 Validation of developed correlation

The developed correlation is validated with the experimental data for water-ethanol mixture as shown in Figure 4.17. The region of applicability of the proposed correlation is heat flux=90.4 kW/m^2, mass flux ranging from 76.67-228.33 kg/m^2-s and inlet temperature from 303-323 K. The MAE of Nusselt number of water calculated from the experiment and those predicted from the present correlation is 10.89% in the investigated range of heat flux, mass flux, channel inlet temperature and ethanol volume fractions. It can be observed that 70 % of experimental data lie within error band of $\pm 15\%$.

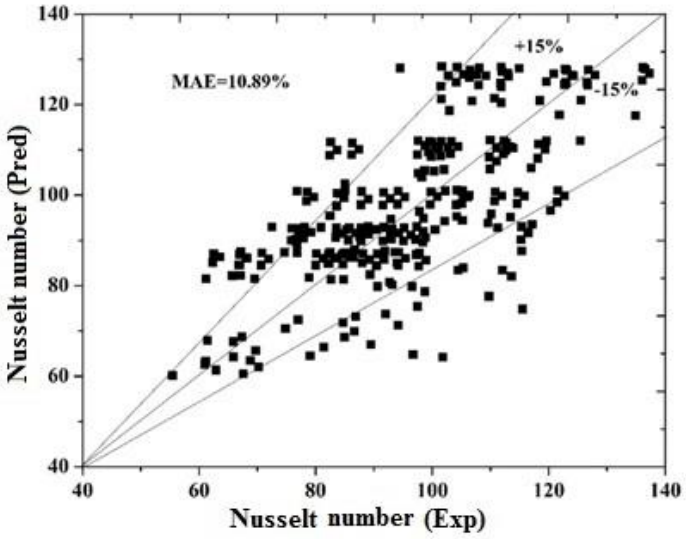

Figure 4.17: Comparison of predicted values from the present correlation with experimental data

The present correlation is also validated with the available literature correlations for water. Papel (1963), Badiuzzaman (1967), Moles et al. (1972) and Baburajan et al. (2013) developed dimensionless heat transfer coefficient correlations for water. Papel developed dimensionless subcooled boiling correlation based on his experimental results as given by Equation (4.35). With water used as test fluid, heat fluxes were varied from 1.33 MW/m^2 to 2.62 MW/m^2, mass fluxes were varied from 1130 kg/m^2-s to 3314 kg/m^2-s and pressure were varied from 0.26 MPa -1.25 MPa.

$$\frac{Nu_{tp}}{Nu_s} = 90BoJa^{-0.84}\left(\frac{\rho_g}{\rho_l}\right)^{0.7} \tag{4.35}$$

Badiuzzaman modified the Papel correlation by incorporating the degree of subcooling as shown by Equation (4.36).

$$\frac{Nu_{tp}}{Nu_s} = 178Bo^{0.75}Ja^{-0.9}\left(\frac{\rho_g}{\rho_l}\right)^{-0.06}\left(\frac{\Delta T_{sub}}{T_{sat}}\right)^{0.45} \tag{4.36}$$

Moles and Shaw also modified Papel correlation by incorporating the effect of Prandtl number as shown by Equation (4.37).

$$\frac{Nu_{tp}}{Nu_s} = 78.5Bo^{0.67}Ja^{-0.5}\left(\frac{\rho_g}{\rho_l}\right)^{-0.03}Pr^{0.45} \tag{4.37}$$

Baburajan et al. (2013) developed the subcooled boiling correlation for hydraulic diameters of 5.5 mm, 7.5 mm and 9.5 mm as shown by Equation (4.38). The mass fluxes were varied from 450 to 935 kg/m^2-s and degree of subcooling were 29℃, 50℃ and 70℃ .

$$\frac{Nu_{tp}}{Nu_s} = 267Bo^{0.86}Ja^{-0.6}Pr^{0.23} \tag{4.38}$$

The single phase term is on the right hand side of Equation (4.35) to Equation (4.38). Dietus Botler Equation is chosen to solve the single phase term in the available literature correlations.

Figures 4.18 to 4.21 show the comparison of Nusselt number of water predicted using the present correlation and those predicted with available literature correlations.

- 70.71% of predicted data lie within $\pm 50\%$ error when compared with those predicted using Papel correlation.

- 75.38 % of predicted data lie within $\pm 30\%$ error when compared with those predicted using Badiuzzaman correlation.
- 67.69 % of predicted data lie within $\pm 40\%$ error when compared with those predicted using Moles-Shaw correlation.
- 66.15% of predicted data lie within $\pm 50\%$ error when compared with those predicted using Baburajan correlation.

The MAE of Nusselt number for water predicted using the present correlation and those predicted with Papel, Badiuzzaman, Moles-Shaw and Baburajan correlations are 41%, 19.61 %, 29.9 % and 43.1% respectively.

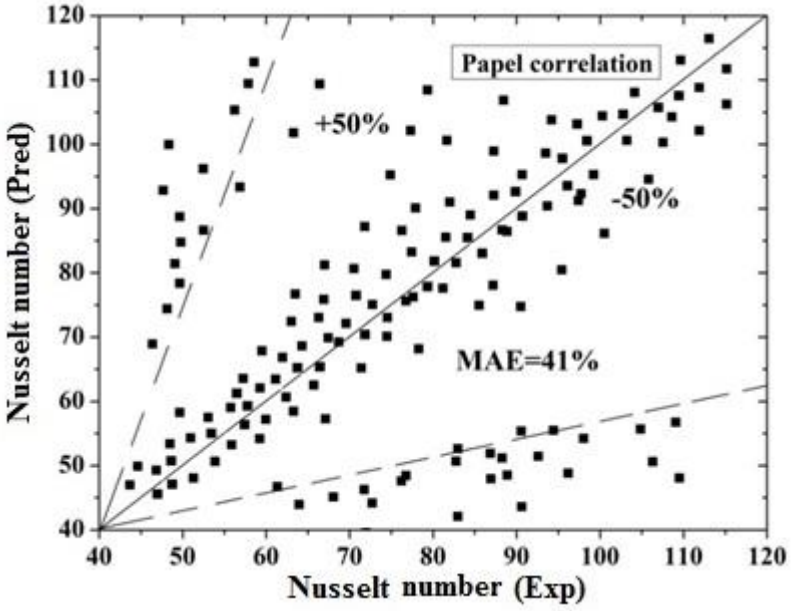

Figure 4.18: Validation of present correlation with Papel correlation.

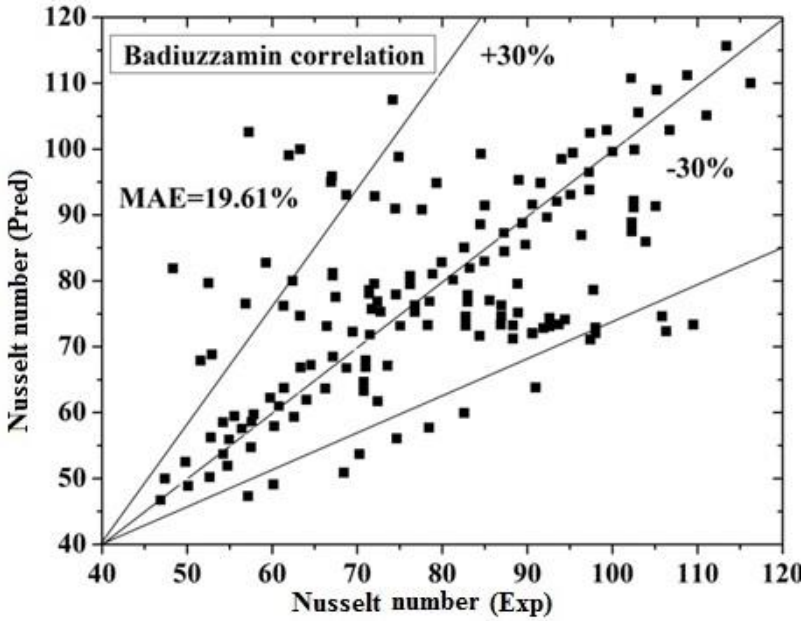

Figure 4.19: Validation of present correlation with Badiuzzamin correlation

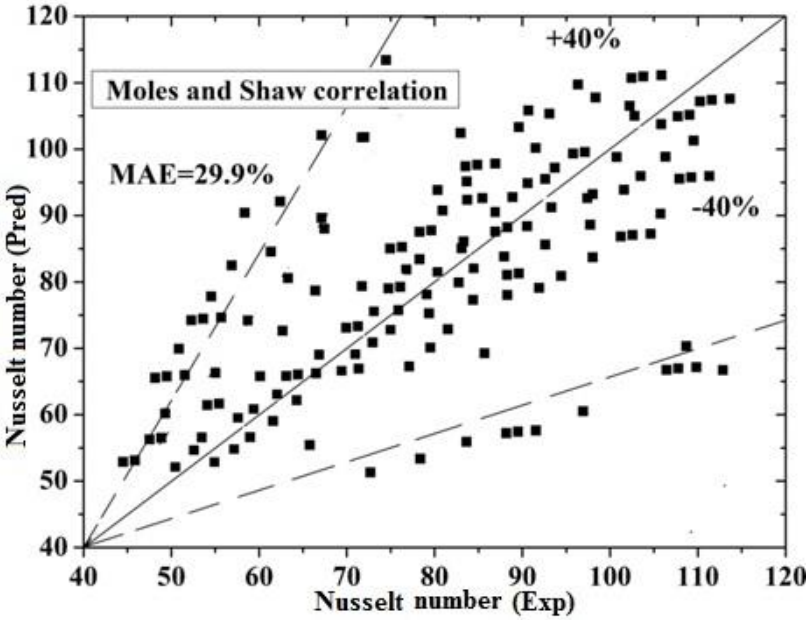

Figure 4.20: Validation of present correlation with Moles-Shaw correlation.

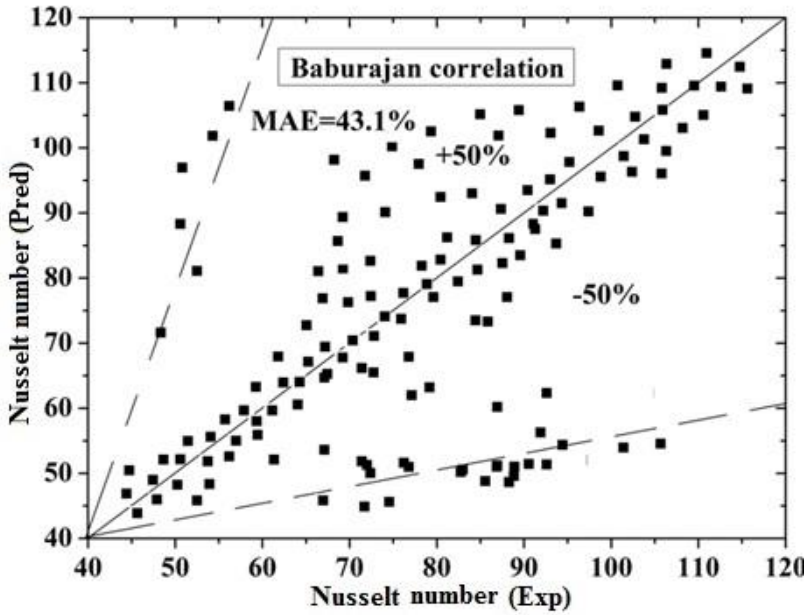

Figure 4.21: Validation of present correlation with Baburajan correlation.

The large deviation is observed because the correlations were developed for high heat fluxes and mass fluxes of water. The predictions from Badiuzzaman correlation compare well with those predicted from present correlation. This is attributed to the presence of degree of subcooling term in the Badiuzzaman correlation. At higher degree of subcooling, the local vapor causes activation of more number of nucleation sites. More number of bubbles moving at a relatively higher velocity and refilling of the sites by adjacent liquid layer create agitation in the liquid.

4.7 WALL HEAT FLUX PARTITIONING

The flow boiling can be divided into two regions, namely partial nucleate boiling region and fully developed nucleate boiling region. The fully developed nucleate boiling region can be further divided into subcooled nucleate boiling region and saturated nucleate boiling region. When the wall temperature exceeds the saturation temperature of the liquid, bubble nucleation occurs. This location is referred as onset of nucleate boiling (ONB). Just downstream of ONB, the bubbles are still tiny that they remain attached to the heater surface. As the bulk liquid temperature increases, the bubbles grow and begin to depart from their sites of origin. These bubbles then slide along the heated surface of the channel

wall and lift off. The location where the bubbles begin to lift off from the heated wall is called the location of onset of Significant Voids (OSV). The bulk liquid temperature attain the saturation temperature of the liquid and the bubbles begin to merge and coalesce with each other. This is called onset of saturated nucleate boiling (OSNB). The region between the ONB and OSV is called partial nucleate boiling. The region between OSV and OSNB is called subcooled nucleate boiling.

Determing the exact value of heat flux required for ONB and OSV is difficult. The region of ONB and OSV can be determined by Unal (1975) correlation as given by Equation (4.39) and (4.40).

$$\frac{h\Delta T_W}{q"} = 0.24 \text{ when } u \geq 0.45\ m/s \tag{4.39}$$

$$\frac{h\Delta T_W}{q"} = 0.11 \text{ when } u < 0.45\ m/s \tag{4.40}$$

Equation (4.40) is preferred because the velocity is found to be less than 0.45 m/s in the present experiment. When $\frac{h\Delta T_W}{q"}$ exceeds 0.11, heat flux value chosen is found to be in the fully developed nucleate boiling region. When $\frac{h\Delta T_W}{q"}$ is less than 0.11, the heat flux is found to be in the partial nucleate boiling region.

4.7.1 Partial nucleate boiling

Bowring (1962) suggested superposition method to determine the heat flux in partial nucleate boiling as given by Equation (4.41) and Equation (4.42). The heat flux supplied is partioned as heat flux due to forced convection and heat flux due to evaporation of the micro layer of the liquid above the wall surface.

$$q_{pb} = q_{fc} + q_{ev} \tag{4.41}$$

$$q_{fc} = h_{fc}(T_{sat} - T_l) \tag{4.42}$$

Single phase forced convective heat transfer coefficient can be calculated by Dietus Botler Equation (4.43).

$$h_{fc} = 0.023 Re^{0.8} Pr^{0.4} \tag{4.43}$$

The evaporative heat flux is considered as fully developed nucleate pool boiling by Bergles and Roshsenow (1964) as given by Equation (4.44). The evaporation above the heated wall is due to the phase change of liquid if it would be in pool boiling condition.

$$q_{ev} = q_{nb} = \mu_l h_{fg} \sqrt{\frac{g(\rho_l - \rho_v)}{\sigma_s}} Pr^{m/n} \left(\frac{C_{p,l}[T_{wall} - T_{Sat}]}{C_s h_{fg}} \right)^{1/n} \quad (4.44)$$

q_{ONB} and ΔT_{wONB} can be predicted by Equation (4.45) and (4.46) as given below:

$$q_{ONB} = q_{nb} \left\{ 1 - \left[\left(\frac{q_{nb}}{q_{fc}} \right)^2 - 1 \right] \left(\frac{q_{fc}}{q_{nb}} \right) \right\} \quad (4.45)$$

$$\Delta T_{wONB} = \left(\frac{q_{ONB}}{5.3 p^{1.156} 1.8^{2.41/p^{0.0234}}} \right)^{p^{0.0234}/2.41} \quad (4.46)$$

Bjorge (1982) suggested using Equation (4.47) to predict the wall super heat during partial nucleate boiling.

$$\Delta T_w = \frac{\Delta T_{wONB}}{\left(1 - \sqrt{\frac{q_{pb}^2 - q_{fc}^2}{q_{nb}^2}} \right)^{1/3}} \quad (4.47)$$

4.7.2 Fully developed nucleate boiling (Subcooled nucleate boiling)

Bowring (1962) developed superposition method to determine the heat flux in fully developed nucleate boiling region as given by Equation (4.48).

$$q_{fdb} = q_{fc} + q_{ev} + q_a \quad (4.48)$$

Agitation heat flux (q_a) results from the thermal boundary layer during bubble growth and lift-off and is given by Equation (4.49). This is due to replacing the adjacent cold liquid in the departed site.

$$q_a = N_a f V_b C_{pl} \Delta T_w \quad (4.49)$$

Nucleation site density (N_a) is calculated by Equation (4.50) and (4.51).

$$N_a = 0.34 \times 10^4 (1 - cos\theta) \Delta T_W^2 \qquad \Delta T_{ONB} < \Delta T_w < 15K \quad (4.50)$$

$$N_a = 0.34 \times 10^4 (1 - cos\theta) \Delta T_W^{5.3} \qquad 15K < \Delta T_w \quad (4.51)$$

Bubble frequency (*f*) is calculated by Equation (4.52)

$$f = \frac{1}{t_w + t_g} \tag{4.52}$$

Where t_w is called bubble waiting period and t_g is called bubble growth period.

Wall superheat in fully developed nucleate boiling (OSV region) can be estimated by Engelberg-Foster and Grief correlation as given by Equation (4.53).

$$\Delta T_{wOSV} = \frac{0.7 q_{fdb}}{h_{fc}} - 7.8 exp[-0.0163(p-1)]\left(0.7 q_{fdb}\right)^{0.25} \tag{4.53}$$

Where, ΔT_{wOSV} is wall super heat at onset of vapour generation.

Sekoguchi et al. (1980) developed an empirical correlation for the wall super heat at commencement of fully developed boiling region as given by Equation (4.54).

$$\Delta T_{wOSV} = 13.5 \frac{h_{fg}}{C_{p,l}} \left(\frac{q*_{avg}}{h_{fg} G}\right)^{0.65} \tag{4.54}$$

Where, $q*_{avg}$ is considered as the average of predicted values of heat flux. The average is calculated by the heat flux value that is considered in the partial nucleate boiling region and the first value of the heat flux which falls under fully developed nucleate boiling region.

Ahmad (1970) developed an empirical correlation assuming the wall temperature at OSV to be equal to the saturation temperature which is represented by Equation (4.55)

$$\frac{h_{OSV} d_h}{k_l} = 2.44 \left(\frac{\rho_l d_h v_l}{\mu_l}\right)^{0.5} \left(\frac{C_{p,l} \mu_l}{k_l}\right)^{0.333} \left(\frac{h_{in}}{h_{fg}}\right)^{0.333} \left(\frac{h_{fg}}{h_l}\right)^{0.333} \tag{4.55}$$

Unal correlation is used to predict the heat flux when the OSV occurs which is given by Equation (4.56).

$$q_{OSV} = \frac{h_{OSV} \Delta T_{w,OSV}}{0.11} \tag{4.56}$$

4.7.3 Estimation of heat flux due to forced convection, evaporation and agitation

The variation of heat flux with wall super heat for water-ethanol mixtures at different ethanol volume fractions and at constant mass flux of 115.33 kg/m^2-s and inlet temperature of 303 K are shown in Figures 4.22 to 4.26. It can be seen that there is significant increase in heat flux at the subcooled flow boiling region when compared with that of forced convective region. Theoretical heat flux are lower than the experimentally determined

heat flux values in the partial nucleate boiling region, but the theoretical heat fluxes are higher than the experimentally determined heat flux values in fully developed nucleate boiling region.

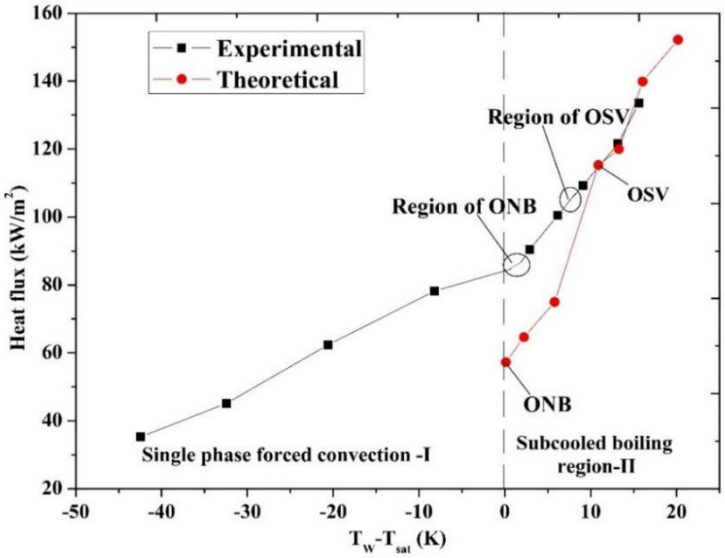

Figure 4.22: Variation of heat flux with wall superheat for water at inlet temperature=303 K.

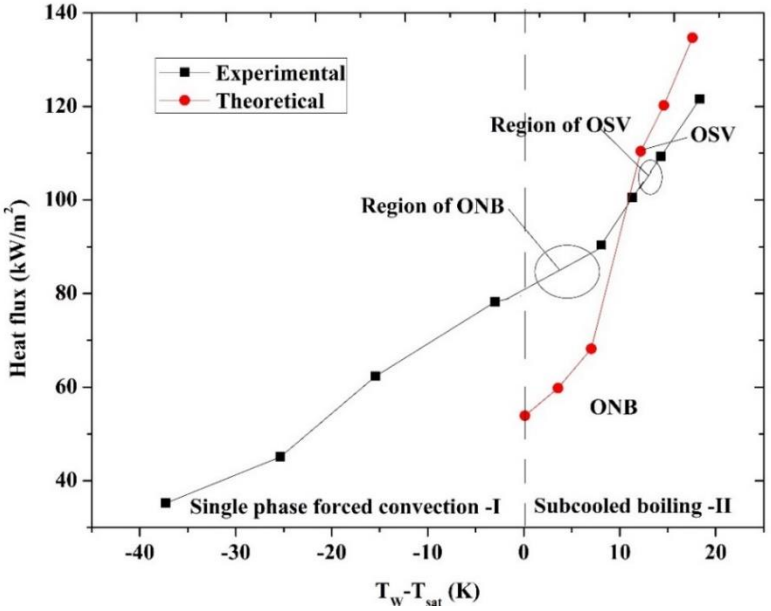

Figure 4.23: Variation of heat flux with wall superheat for water-ethanol mixture of ethanol volume fraction 25% at inlet temperature=303 K.

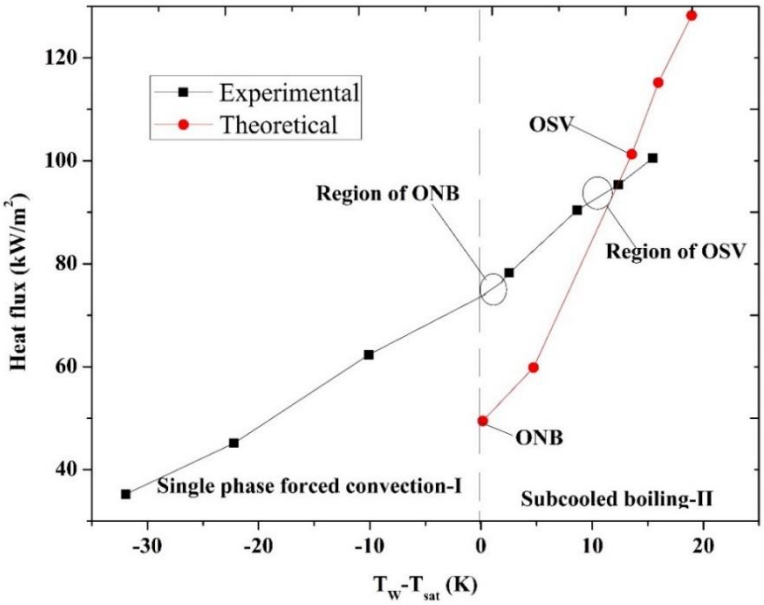

Figure 4.24: Variation of heat flux with wall superheat for water-ethanol mixture of ethanol volume fraction 50% at inlet temperature=303 K.

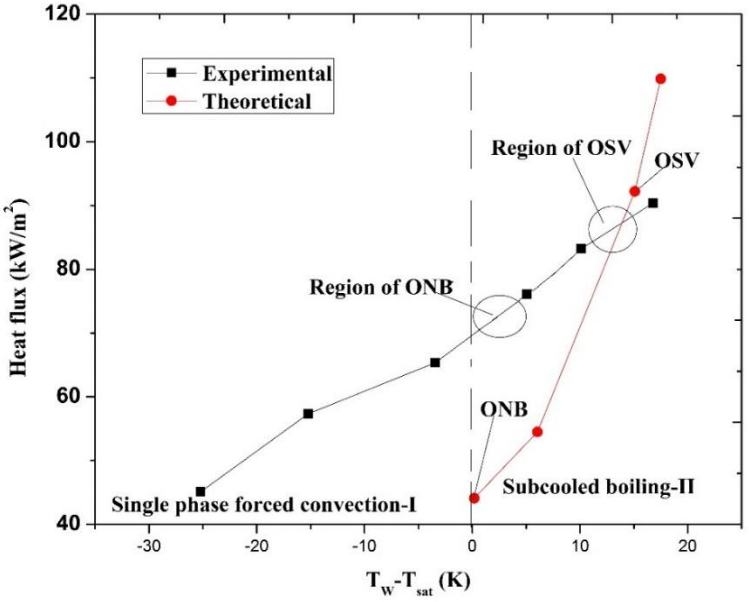

Figure 4.25: Variation of heat flux with wall superheat for water-ethanol mixture of ethanol volume fraction 75% at inlet temperature=303 K.

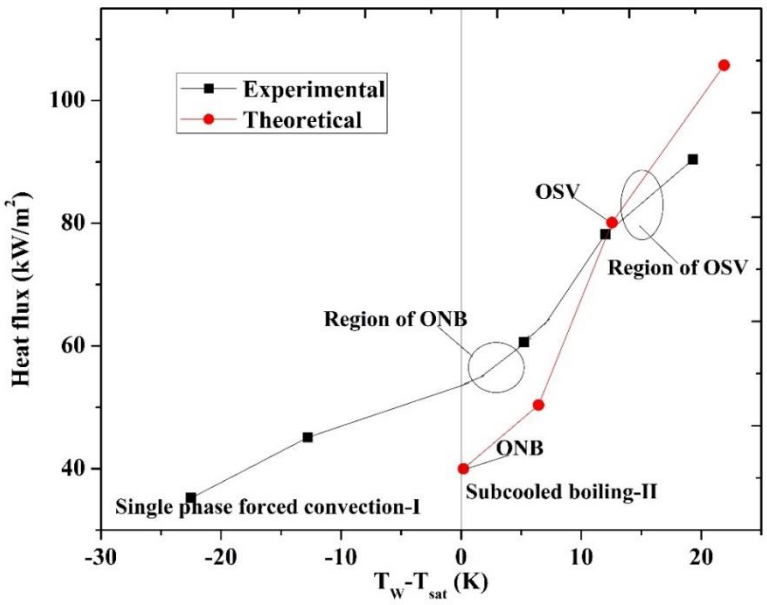

Figure 4.26: Variation of heat flux with wall superheat for ethanol at inlet temperature=303 K.

Figure 4.27 shows the variation of heat flux due to convection, evaporation and agitation with experimentally determined heat flux for water. It can be observed that the heat flux due to forced convection decreases with increase in experimentally determined heat flux in partial nucleate and fully developed nucleate boiling regions. This implies that the effect of mass flux is not significant in these regions. This supports the experimental results presented in section 4.3. Heat flux due to evaporation and agitation increase with increase in heat flux. Fully developed nucleate boiling occurs when heat flux value exceeds 100 kW/m^2. Above this particular value of heat flux, agitation occurs.

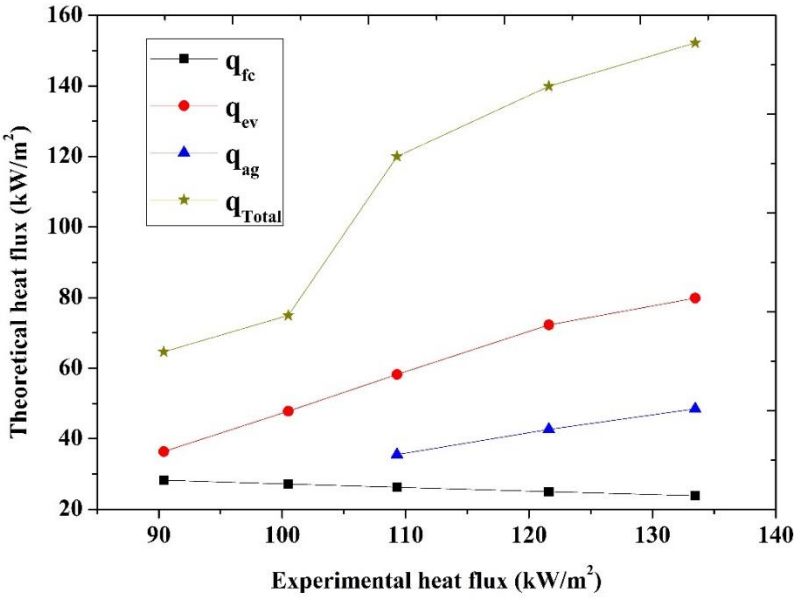

Figure 4.27: Variation of theoretical heat flux with experimentally determined heat flux for water

CHAPTER 5

NUMERICAL ANALYSIS AND MATHEMATICAL MODELING

The numerical results of forced convection and subcooled flow boiling of water-ethanol mixtures are presented in this chapter.

5.1 FORCED CONVECTIVE HEAT TRANSFER COEFFICIENT: MATHEMATICAL MODELLING

5.1.1 Governing equations

The flow is considered to be one dimensional. The wall temperature determined from the experiment is considered as Dirichlet boundary condition.

The continuity equation is given by Equation (5.1)

$$\frac{\partial u}{\partial x} = 0 \tag{5.1}$$

The x-momentum-Navier Stokes equation is given by Equation (5.2)

$$\frac{\partial u}{\partial t} = -\frac{\partial p}{\partial x} + \mu\left(\frac{\partial^2 u}{\partial y^2}\right) \tag{5.2}$$

The energy equation is given by Equation (5.3)

$$C_p \frac{\partial T}{\partial t} = -u\frac{dp}{dx} + k\frac{\partial^2 T}{\partial x^2} + k\frac{\partial^2 T}{\partial y^2} + \mu\left(\frac{du}{dy}\right)^2 \tag{5.3}$$

The pressure drop and velocity in the x-momentum equation is determined by pressure correction method. The determined values of pressure drop and velocity obtained are substituted in the energy equation and solved by the Lax Wendroff method to find the temperature of the fluid. The heat transfer coefficient is determined from the known values of wall temperature, heat flux and determined values of fluid temperature as shown in Equation (5.4).

$$h = \frac{q''}{(T_W - T_f)} \tag{5.4}$$

Specific heat of the mixture is calculated using simple mixing rule. Thermal conductivity and liquid viscosity are calculated by Flippov (1968) and McLaughlin Equation (Ratliff et al. 1971) represented in the Equation (4.20) and Equation (4.21) of section 4.6

5.1.2 Pressure Correction Method

The x-momentum Navier Stokes equation is solved to find the pressure drop values at the points located at the vertices of the grids labelled as $(i+1, j+1), (i+1, j+2)$ etc. The velocity is solved at the grids labeled as $\left(i+\frac{1}{2}, j+\frac{1}{2}\right), (i+\frac{1}{2}, j)$ etc. in a staggered grid formation. The finite difference equation is solved by Equation (5.5):

$$u^{t+1*}_{i+\frac{1}{2},j+1/2} = -\frac{\Delta t}{\Delta x}\left(p^{t*}_{i+1,j+1} - p^{t*}_{i+2,j+1}\right) + \frac{\mu \Delta t}{\Delta y^2}\left(u^{t*}_{i+\frac{1}{2},j} - 2u^{t*}_{i+\frac{1}{2},j+\frac{1}{2}} + u^{t*}_{i+\frac{1}{2},j+1}\right) + u^{t*}_{i+\frac{1}{2},j+\frac{1}{2}} \tag{5.5}$$

Where n denotes the time steps and * denotes the initial assumed values for pressure drop and velocity. Equation (5.6) is written in the form which represents the actual finite difference equation without any guessed values:

$$u^{t+1}_{i+\frac{1}{2},j+1/2} = -\frac{\Delta t}{\Delta x}\left(p^{t}_{i+1,j+1} - p^{t}_{i+2,j+1}\right) + \frac{\mu \Delta t}{\Delta y^2}\left(u^{t}_{i+\frac{1}{2},j} - 2u^{t}_{i+\frac{1}{2},j+\frac{1}{2}} + u^{t}_{i+\frac{1}{2},j+1}\right) + u^{t}_{i+\frac{1}{2},j+\frac{1}{2}} \tag{5.6}$$

By subtracting Equation (5.6) from Equation (5.5), Equation (5.7) is obtained.

$$u^{t+1\prime}_{i+\frac{1}{2},j+1/2} = -\frac{\Delta t}{\Delta x}\left(p^{t'}_{i+1,j+1} - p^{t'}_{i+2,j+1}\right) + \frac{\mu \Delta t}{\Delta y^2}\left(u^{t'}_{i+\frac{1}{2},j} - 2u^{t}_{i+\frac{1}{2},j+\frac{1}{2}} + u^{t'}_{i+\frac{1}{2},j+1}\right) + u^{t\prime}_{i+\frac{1}{2},j+\frac{1}{2}} \tag{5.7}$$

Equation (5.7) represents the corrected values of the velocity. When the actual discretized momentum Equation (5.7) is subtracted from the assumed values of discretized momentum Equation (5.6) with source term $u^{t'}_{i+\frac{1}{2},j} - 2u^{t'}_{i+\frac{1}{2},j+\frac{1}{2}} + u^{t'}_{i+\frac{1}{2},j+1}$ set to zero, Equation (5.8) is obtained:

$$u^{t+1*}_{i+\frac{1}{2},j+\frac{1}{2}} = -\frac{\Delta t}{\Delta x}\left(p^{t'}_{i+1,j+1} - p^{t'}_{i+2,j+1}\right) + u^{t*}_{i+\frac{1}{2},j+\frac{1}{2}} \tag{5.8}$$

By substituting Equation (5.8) in the Equation (5.5), Equation (5.9) is obtained:

$$\left(p^{t\prime}_{i+1,j+1} - p^{t\prime}_{i+2,j+1}\right) = \frac{\Delta t}{\Delta x}\left(u^{t\prime}_{i+\frac{1}{2}',j+\frac{1}{2}} - u^{t+1\prime}_{i+\frac{1}{2}',j+1+\frac{1}{2}}\right) \quad (5.9)$$

The corrected values of pressure drop are solved by Equation (5.9). After obtaining the values of corrected pressure drop and velocity, the actual pressure drop and velocity are solved by the Equations (5.10) and Equation (5.11) respectively:

$$\Delta p = \Delta p^* + \alpha \Delta p' \quad (5.10)$$

$$u = u^* + \alpha_{ur} u' \quad (5.11)$$

Δp^* is the pressure drop of the previous iteration.

$\Delta p'$ is the corrected pressure drop.

u^* is the velocity of the previous iteration.

u' is the corrected velocity.

α_{ur} is the under relaxation factor which is assumed to be 0.5. This is assumed suitably for the convergence criteria.

The inlet velocity is assumed to satisfy the laminar flow condition. The no slip boundary condition for velocity is assumed at the wall. The solution is obtained by marching in the *x*-axis to solve for pressure drop and in the y-axis to solve for velocity. The algorithm is solved by following steps:

Step 1: Pressure drop in the first time step is assumed between the two grid points suitably in Equation (5.5) to solve for the value of velocity for the next time step.

Step 2: The value of velocity obtained from Equation (5.5) is substituted in Equation (5.8) to determine the pressure drop between the two grid points.

Step 3: The pressure drop value obtained from Equation (5.8) is substituted in Equation (5.7) to get corrected velocity for next time step.

Step 4: The corrected pressure drop value is obtained after substituting the corrected velocity value obtained from Equation (5.7) in Equation (5.9). From the corrected pressure drop and assumed pressure drop values the actual pressure drop for first time step is calculated from Equation (5.10). Similarly velocity is also determined from Equation (5.11).

The steps from 1 to 4 are repeated for further time steps until the convergence in the pressure drop value is obtained.

5.1.3 Lax Wandroff Explicit Method

The Lax-Wandrof explicit method is used to find temperature at different nodes in the x and y axes. The Dirichlet boundary condition is specified at the bottom wall of the channel. This temperature is obtained from the Fourier law of heat conduction equation determined from the experiment. The values obtained for pressure drop and velocity from the Navier-Stokes equations are substituted in the energy equation and solved by Equation (5.12). The temperature values are iterated till convergence is achieved.

$$T_{i+1,j+1}^{t+1} = \frac{\Delta t}{\Delta x Cp}\left(p_{i+1,j+1}^{t} - p_{i+2,j+1}^{t}\right) + \frac{k\Delta t}{\Delta x^2 Cp}\left(T_{i,j+1}^{t} - 2T_{i+\frac{1}{2},j+1}^{t} + T_{i+1.j+1}^{t}\right) +$$

$$\frac{k\Delta t}{\Delta y^2 Cp}\left(T_{i+1,j}^{t} - 2T_{i+1.j+1/2}^{t} + T_{i+1.j+1}^{t}\right) + \frac{\Delta t \mu}{\Delta y^2 Cp}\left(u_{i+1,j}^{t} - u_{i+1,j+1}^{t}\right)^2 \qquad (5.12)$$

5.1.4 Grid Independence study

The pressure drop, velocity and temperature are calculated by numerical techniques such as pressure correction method and the Lax Wendroff explicit method. For this analysis, the entire channel is divided into staggered grids as shown in Figure 5.1. The grid independence for the pressure drop and temperature of water is checked for the different grid values as shown in Table 5.1. The change in pressure drop and temperature of water are not very significant. The grid size of 15 X 8 are chosen in the present study.

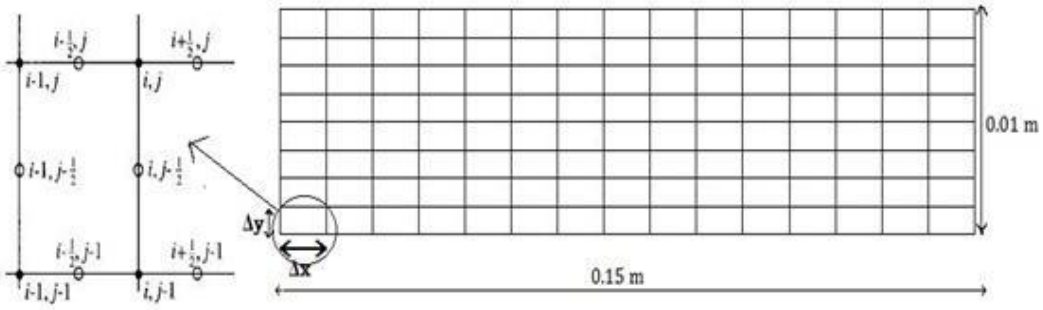

Figure 5.1: Discretization of rectangular channel

The pressure drop values converged around 500th time step and the temperature values converged around 1350th time steps for the grid numbers of 15 X 8 with $\Delta x = 0.01$ m, $\Delta y = 0.00125$ m and $\Delta t = 0.01$s.

Table 5.1 . Grid independence for different grid sizes.

Grid size (i×j)	Number of grids	Δx in m	Δy in m
10X6	60	0.015	0.00167
10X7	70	0.015	0.00143
12X6	72	0.0125	0.00167
10X8	80	0.015	0.00125
12X7	84	0.0125	0.00143
15X6	90	0.01	0.00167
12X8	96	0.0125	0.00125
15X7	105	0.01	0.00143
18X6	108	0.0083	0.00167
15X8	120	0.01	0.00125
18X7	126	0.0083	0.0015

The grid independence study showed negligible change of results for pressure drop values. Hence the same grids are chosen to solve the energy equation for all the values of Reynolds number (mass flux). The pressure drop and velocity obtained from the Navier-Stokes equation are substituted in the energy equation and solved by the Lax Wendroff method to find the temperature of the fluid. The code is developed by using Matlab R2013a programming to solve for heat transfer coeffient which is shown in APPENDIX C.

5.2 FORCED CONVECTIVE HEAT TRANSFER COEFFICIENT: NUMERICAL SIMULATION

The Semi implicit pressure correction technique (SIMPLE) is adopted in ANSYS-FLUENT-15 to solve for heat transfer coefficient of water-ethanol mixture. For the numerical study, only one channel is considered because the channels are assumed to be

symmetrical. ANSYS-ICEM-15 tool is used for modeling the rectangular channel as shown in Figure 5.2.

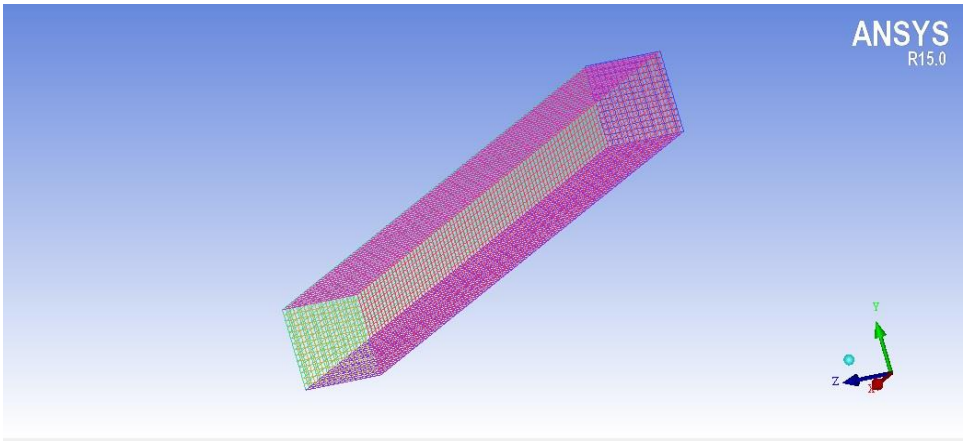

Figure 5.2: Meshed model of rectangular channel.

Major pre-processor settings are energy equations, velocity, wall temperature, heat flux, the fluid properties, flow properties and time steps. SIMPLE is used for solving the x-momentum equation and Lax-Wandroff method is used for solving energy equation. Grid independence study is carried out in present study. It is conducted for 21.78 kW/m^2 heat flux and 0.076 m/s velocity. It is found that there is no significant variation in the value of heat transfer coefficient of water as shown in Table 5.2. Hence the grid size of 15×15×150 are chosen in the present study.

Table 5.2: Grid independence study

Sl.no	Grids along the Width, Height and Length ($W \times H \times L$)	Total no. of cells	Heat transfer coefficient (kW/m^2-K)	Change in heat transfer coefficient (%)
1	$10 \times 10 \times 100$	10000	1.1	--
2	$15 \times 10 \times 100$	15000	1.19	7.56
3	$15 \times 15 \times 100$	22500	1.27	6.72
4	$15 \times 15 \times 150$	33750	1.3	2.3
5	$20 \times 20 \times 150$	60000	1.31	0.769

Mixture properties like liquid density, specific heat, thermal diffusivity are calculated using simple mixing rule. Thermal conductivity and liquid viscosity are calculated by Flippov (1968) and McLaughlin Equation (Ratliff et al. 1971) represented in the Equation (4.20)

and Equation (4.21) of section 4.6. The variation of heat transfer coefficients along the length of the channel for water are shown in Figure 5.3 and 5.4. The variation of heat transfer coefficients of water-ethanol mixture of ethanol volume fraction 25% is shown in Figure 5.5.

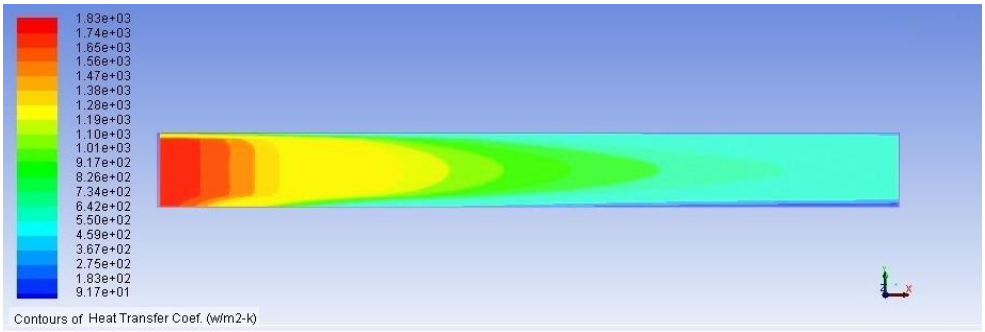

Figure 5.3: Variation of forced convective heat transfer coefficient along the length of the channel for water at heat flux =21.78 kW/m^2 and mass flux=76.67 kg/m^2-s

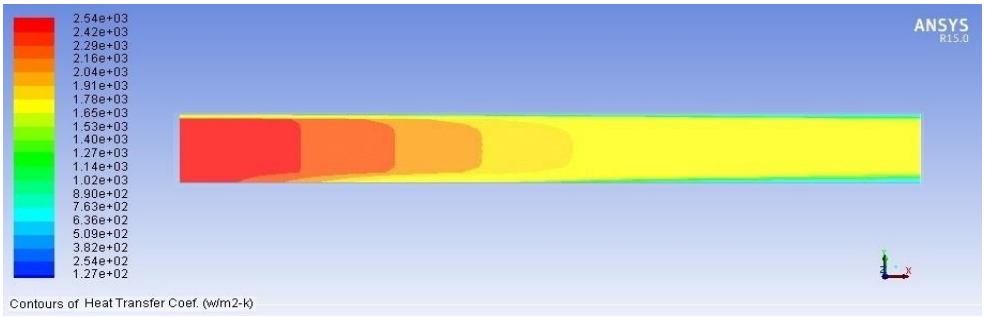

Figure 5.4: Variation of forced convective heat transfer coefficient along the length of the channel for water at heat flux =21.78 kW/m^2 and mass flux=228.33 kg/m^2-s

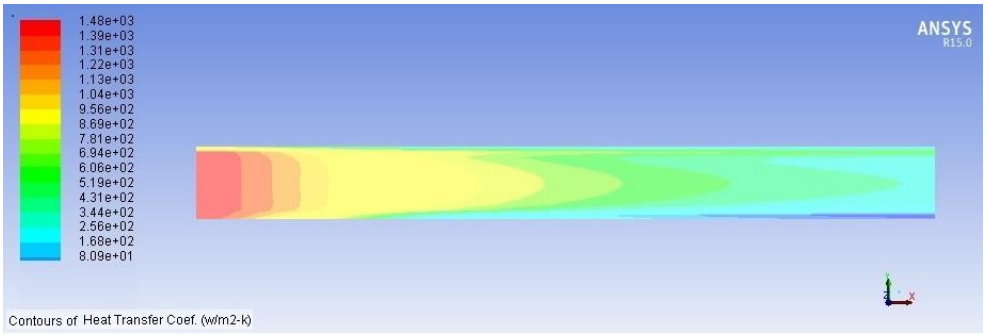

Figure 5.5: Variation of forced convective heat transfer coefficient along the length of the channel for water-ethanol mixture of ethanol volume fraction 25% at heat flux =21.78 kW/m^2 and mass flux=228.33 kg/m^2-s.

It can be seen that the heat transfer coefficient decreases along the length of the channel. This is due to the increase in thermal boundary layer thickness along the length of the channel. Contours of forced convective heat transfer coefficients of water-ethanol mixtures of 50%, 75% and 100% ethanol volume fraction are shown in APPENDIX D.

The results obtained from pressure correction SIMPLE solution method by ANSYS are validated with results obtained from pressure correction-Lax Wandrof Technique by mathematical modeling and experiment. The comparison of numerical and mathematical modeling results of forced convective heat transfer coefficient of water with that of experiment is shown in Figure 5.6.

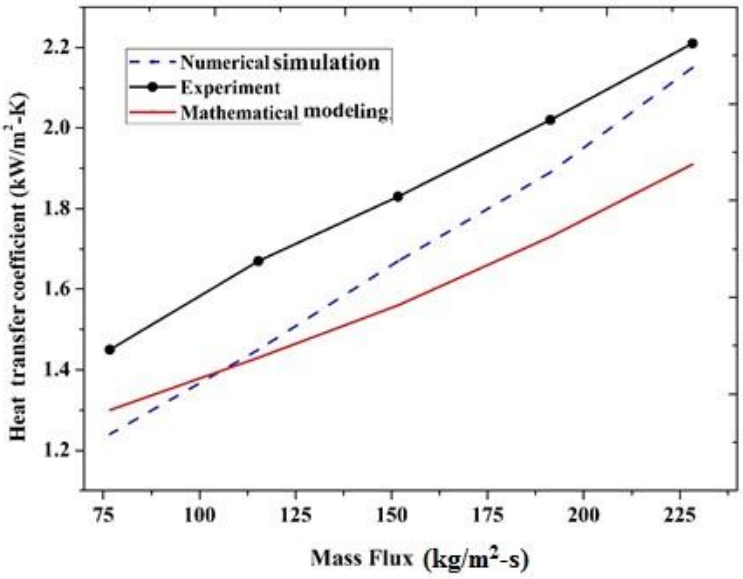

Figure 5.6: Comparison of numerical simulation and mathematical modeling results of heat transfer coefficient with that of experiment

It is found that the forced convective heat transfer coefficient of water obtained from numerical simulation deviated by 17.1% from that of the experiment and 21.3 % from that of mathematical modeling. The variation of forced convective heat transfer coefficient of water-ethanol mixture with ethanol volume fraction is shown in Figure 5.7. The heat transfer coefficient decreases with increase in ethanol volume fraction because of lower thermal conductivity and thermal capacity of ethanol than that of water.

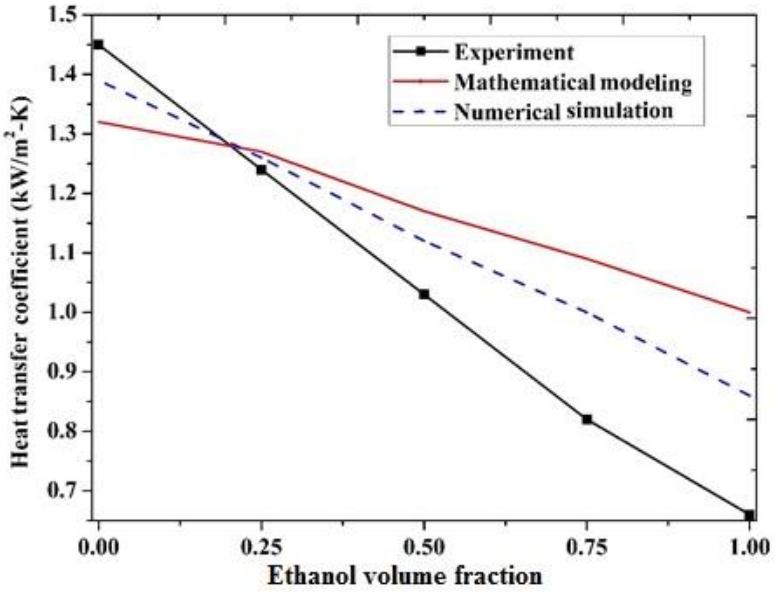

Figure 5.7: Variation of forced convective heat transfer coefficient with ethanol volume fraction at heat flux=21.78 kW/m^2 and mass flux=76.67 kg/m^2-s.

The deviation is due to certain assumptions made during the numerical simulation and mathematical modeling. Single channel analysis is carried out for both the numerical and mathematetical modeling. The momentum and energy equations are simplified to obtain one dimensional flow for mathematical modeling. Mixed type boundary conditions are adopted to solve numerically, where in the experimentally determined wall temperature and wall heat flux are specified. No slip boundary condition and wall temperature (The Dirichlet boundary condition) is specified to determine the velocity, pressure and fluid temperature by mathematical modeling. Unlike the experiment, in mathematical modeling and numerical simulation, the heat flux and wall temperature specified as boundary conditions are considered to be constant.

5.3 SUBCOOLED FLOW BOILING HEAT TRANSFER COEFFICIENT: MATHEMATICAL MODELING

The available numerical methods for the prediction of two-phase flows with discrete interfaces can be classified into surface and volume methods (Sussman and Elbridge , 2000). Surface methods mark and track the interface explicitly, either (i) with a set of marker particles or line segments or (ii) by associating the interface with a set of nodal

points. Surface methods maintain sharp interfaces for which the exact position is known throughout the calculation (Gueyffier, 1999). The disadvantage of these methods is that special critiques needs to be employed to deal with interfaces which are exposed to large deformations or stretching. In volume methods, the different fluids are marked by an indicator function which may in turn be a volume fraction or a level set (Gerlach, 2006 and Welch et al. 2000). The advantage of these methods is their ability to deal with arbitrarily shaped interfaces and to cope up with large deformations as well as interface rupture and coalescence in a natural way.

The thermophysical and thermodynamic properties of the subcooled boiling fluid are determined by incorporating bubble void fraction (α) by simple mixture rule. The thermodynamic and thermophysical properties are substituted in the x-momentum and energy equation to determine the values of pressure drop, velocity and temperature of the fluid. From the temperature values, the subcooled flow boiling heat transfer coefficient is determined and compared with that of experimental results. The code is developed by using Matlab R2013a programming to solve for heat transfer coeffient which is shown in APPENDIX C.

5.3.1 The numerical scheme adopted to solve for bubble void fraction

The sample image of bubble formation for water at heat flux=90.4 kW/m^2, mass flux=76.67 kg/m^2-s and inlet temperature=303 K is shown in Figure 5.8. The conservative form of scalar convection equation for the bubble void fraction is given by Equation (5.13) (Tomasz and Tadeusz, 2008). The equation is considered to be first order hyperbolic equation.

$$\frac{\partial \alpha}{\partial t} = u \frac{\partial \alpha}{\partial x} \tag{5.13}$$

The Crank Nicolson implicit scheme is used as technique for discretization.

$$\frac{\alpha_i^{t+1} - \alpha_i^t}{\Delta t} = u_{in} \left\{ \frac{\left(\frac{\alpha_{i+1}^{t+1} + \alpha_{i+1}^t}{2} \right) - \left(\frac{\alpha_i^{t+1} + \alpha_i^t}{2} \right)}{\left(\frac{\Delta x}{2} \right)} \right\} \tag{5.14}$$

Algebraic equations are obtained from Equation (5.14) is solved to determine bubble void fraction by using Tridiagonal Matrix Algorithm (TDMA). The bubble void fraction is

solved in the control surface as upwind, donor and accepter cells with the face values in between the interfaces of grid as shown in Figure 5.9

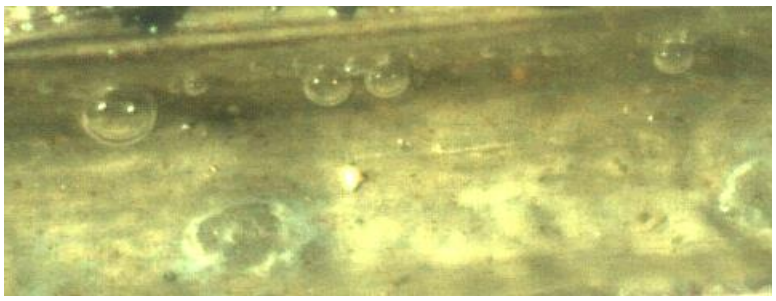

Figure 5.8: Bubble formation of water at Heat flux=90.4 kW/m^2 and mass flux=76.67 kg/m^2-s.

Initially the values are assumed suitably varying from 0 to 1, depending upon occupation of bubbles in the channel surface. The bubble void fraction with values more than one and less than zero are obtained. Hence the corrector-predictor steps are involved to solve these void fractions. The new amount of fluid to be convected over the face is determined by subtracting the unboundedness error from the original amount of fluid convected over the face (Ubbink, 1999).

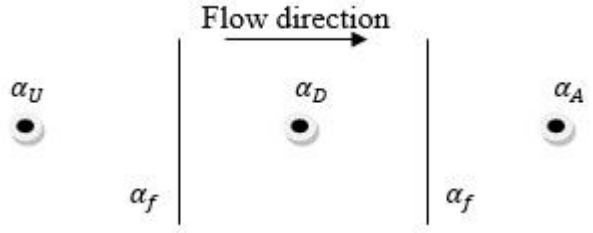

Figure 5.9: Control area to solve bubble void fraction.

5.3.2 Prediction of α in grid centre by corrector predictor method

Following steps are followed when $\alpha_D$values obtained exceed 1 or negative.

$$\beta_f = \left\{ min\left\{ \frac{\cos(2\theta_f + 1)}{2} \right\}, 1.0 \right\} \tag{5.15}$$

$\beta_f$is called weighing factor. The weighing factor incorporates the unboundedness error while calculating the bubble void fraction at the grid center and the face.

$$\Delta\alpha = \frac{{\alpha_A}^t + {\alpha_A}^{t+1}}{2} - \frac{{\alpha_D}^t + {\alpha_D}^{t+1}}{2} \tag{5.16}$$

$$\beta_f' = min\frac{E^-(2+C_f-2C_f\beta_f)}{2C_f(\Delta\alpha^*-E^-)},\ \beta_f \qquad \text{When } \Delta\alpha^* > E^- \tag{5.17}$$

$$\beta_f' = 0, \qquad \text{When } \Delta\alpha^* < E^- \tag{5.18}$$

$$E^- = \max\left\{-\alpha_D^{t+\delta t}, 0\right\} \text{ when } \alpha_D^{t+1} < 0 \tag{5.19}$$

$$E^+ = \max\left\{\alpha_D^{t+\delta t} - 1, 0\right\} \text{ When } \alpha_D^{t+1} > 1 \tag{5.20}$$

$$\beta_f' = min\frac{E^-(2+C_f-2C_f\beta_f)}{2C_f(-\Delta\alpha^*-E^+)},\ \beta_f \qquad \text{When } -\Delta\alpha^* > E^+ \tag{5.21}$$

$$\beta_f' = 0, \qquad \text{When } -\Delta\alpha^* < E^+ \tag{5.22}$$

$$\beta_f^* = \beta_f \sim \beta_f{}' \tag{5.23}$$

The corrected weighting factor β_f^* should be always less than or equal to the previous weighting factor. Otherwise the contribution of the downwind cell starts to increase and so also the degree of unboundedness increases. The lower limit on β_f^* remains zero and this is applied to Equation (5.23) to obtain bounds for β_f'.

$$\alpha^{**}{}_f = \left(1-\beta_f^*\right)\left[\frac{\alpha_D^t+\alpha_D^{t+\delta t}+E^-}{2}\right] + \left[\frac{\alpha_A^t+\alpha_A^{t+\delta t}+E^-}{2}\right] \tag{5.24}$$

or

$$\alpha^{**}{}_f = \left(1-\beta_f^*\right)\left[\frac{\alpha_D^t+\alpha_D^{t+\delta t}+E^+}{2}\right] + \left[\frac{\alpha_A^t+\alpha_A^{t+\delta t}+E^+}{2}\right] \tag{5.25}$$

Where α_f^{**} is the new face value and $E^-$and E^+ are the magnitude of the unbounded void value.

$$\alpha_f^* = \alpha_f^{**} \pm \frac{E^-}{c} \tag{5.26}$$

or

$$\alpha_f^* = \alpha_f^{**} \pm \frac{E^+}{c} \tag{5.27}$$

$$\alpha_f^{"} = \left(1-\beta_f\right)\frac{\alpha_D^t+\alpha_D^{t+\delta t}}{2} + \beta_f\frac{\alpha_A^t+\alpha_A^{t+\delta t}}{2} \tag{5.28}$$

Equation (5.29) is used for calculating α_D for next time step and is given as:

$$\alpha_D^c = \frac{2\alpha_f^*+\beta_f\alpha_D^t-\alpha_D^t-\beta_f\alpha_A^t-\beta_f\alpha_A^{t+\Delta t}}{(1-\beta_f)} \tag{5.29}$$

5.3.3 Prediction of α in face centre by corrector predictor method

Following steps are followed when α_f(face values) obtained exceed 1 or negative.

$$\widetilde{\alpha_D} = \frac{\alpha_D - \alpha_U}{\alpha_A - \alpha_U} \tag{5.30}$$

$$\widetilde{\alpha_f} = \frac{\alpha_f - \alpha_U}{\alpha_A - \alpha_U} \tag{5.31}$$

$$\tilde{\alpha}_{fBC} = min\left\{\frac{\widetilde{\alpha_D}}{c}, 1.0\right\} \quad \text{When } 0 \leq \tilde{\alpha}_D \leq 1 \tag{5.32}$$

$$\tilde{\alpha}_{fBC} = \widetilde{\alpha_D} \quad \text{When } \tilde{\alpha}_D < 0, \widetilde{\alpha_D} > 1 \tag{5.33}$$

$$\widetilde{\alpha_{fQuick}} = min\left\{\frac{8c\tilde{\alpha}_D + (1-c)(6\widetilde{\alpha_D} + 3)}{8}\right\} \quad \text{When } 0 \leq \tilde{\alpha}_D \leq 1 \tag{5.34}$$

$$\widetilde{\alpha_{fQuick}} = \tilde{\alpha}_D \quad \text{When } \tilde{\alpha}_D < 0, \widetilde{\alpha_D} > 1 \tag{5.35}$$

The above derivation for the volume of fluid method is a resolution scheme to be carried out only in one-dimension.

$$\alpha_f^c = \beta_f \tilde{\alpha}_{fBC} + (1 - \beta_f)\tilde{\alpha}_{fQuick} \tag{5.36}$$

Where $\tilde{\alpha}_{fBC}$ is bubble void fraction in face center to satisfy boundedness criteria. $\tilde{\alpha}_{fQuick}$ is bubble void fraction in face center to satisfy conservative criteria by QUICK scheme.

When α is more than 1 or less than 0 in the grid face and grid centre, the average values obtained from Equation (5.28) and Equation (5.36) are considered for the new value at the grid face.

5.3.4 Mixture rule

The viscosity, specific heat and thermal conductivity are determined by simple mixture rule as given by Equation (5.37), (5.38) and (5.39).

$$\mu = \alpha\mu_{vm} + (1 - \alpha)\mu_{lm} \tag{5.37}$$

$$k = \alpha k_{vm} + (1 - \alpha)k_{lm} \tag{5.38}$$

$$C_p = \alpha C_{pvm} + (1 - \alpha)C_{plm} \tag{5.39}$$

5.3.5 Governing equations

The continuity equation is represented by Equation (5.40)

$$\frac{\partial u}{\partial x} = 0 \tag{5.40}$$

The x-momentum-Navier Stokes equation is represented by Equation (5.41)

$$\frac{\partial u}{\partial t} = -\frac{\partial p}{\partial x} + \mu\left(\frac{\partial^2 u}{\partial y^2}\right) \tag{5.41}$$

The energy equation is represented by Equation (5.42)

$$C_p \frac{\partial T}{\partial t} = -u\frac{dp}{dx} + k\frac{\partial^2 T}{\partial x^2} + k\frac{\partial^2 T}{\partial y^2} + \mu\left(\frac{du}{dy}\right)^2 \tag{5.42}$$

The wall temperature which is determined from the experiment is considered as the boundary condition. The x-momentum is solved mathematically to determine the pressure drop. The pressure drop is substituted in the energy equation to determine the fluid temperature. After determining the temperature of the fluid from the energy equation, the heat transfer coefficient is determined from the heat flux, temperature of the fluid and bottom wall of the channel by Equation (5.43).

$$h = \frac{q''}{(T_W - T_f)} \tag{5.43}$$

The velocity and pressure drop are calculated by applying Pressure correction method. This calculates the pressure drop between each node along the x-axis and variation of velocity in each node along the y-axis. The temperature at each grid along x and y axes are determined using the Lax-Wandrof explicit method.

5.3.6 Pressure Correction Method

The x-momentum Navier Stokes equation is solved to find the pressure drop values at the points located at the vertices of the grids labelled as $(i+1, j+1), (i+1, j+2)$ etc. The velocity is solved at the grids labeled as $\left(i+\frac{1}{2}, j+\frac{1}{2}\right), (i+\frac{1}{2}, j)$ etc. in a staggered grid formation. The finite difference equation is solved by Equation (5.44):

$$u_{i+\frac{1}{2},j+1/2}^{t+1*} = -\frac{\Delta t}{\Delta x}\left(p_{i+1,j+1}^{t*} - p_{i+2,j+1}^{t*}\right) + \frac{\mu \Delta t}{\Delta y^2}\left(u_{i+\frac{1}{2},j}^{t*} - 2u_{i+\frac{1}{2},j+\frac{1}{2}}^{t*} + u_{i+\frac{1}{2},j+1}^{t*}\right) + u_{i+\frac{1}{2},j+\frac{1}{2}}^{t*} \tag{5.44}$$

Where n denotes the time steps and * denotes the initial assumed values for pressure drop and velocity. Equation (5.45) is written in the form which represents the actual finite difference equation without any guessed values:

$$u_{i+\frac{1}{2},j+1/2}^{t+1} = -\frac{\Delta t}{\Delta x}\left(p_{i+1,j+1}^{t} - p_{i+2,j+1}^{t}\right) + \frac{\mu \Delta t}{\Delta y^2}\left(u_{i+\frac{1}{2},j}^{t} - 2u_{i+\frac{1}{2},j+\frac{1}{2}}^{t} + u_{i+\frac{1}{2},j+1}^{t}\right) + u_{i+\frac{1}{2},j+\frac{1}{2}}^{t} \quad (5.45)$$

By subtracting Equation (5.45) from Equation (5.44), Equation (5.46) is obtained.

$$u_{i+\frac{1}{2},j+1/2}^{t+1\prime} = -\frac{\Delta t}{\Delta x}\left(p_{i+1,j+1}^{t\prime} - p_{i+2,j+1}^{t\prime}\right) + \frac{\mu \Delta t}{\Delta y^2}\left(u_{i+\frac{1}{2},j}^{t} - 2u_{i+\frac{1}{2},j+\frac{1}{2}}^{t\prime} + u_{i+\frac{1}{2},j+1}^{t\prime}\right) + u_{i+\frac{1}{2},j+\frac{1}{2}}^{t\prime} \quad (5.46)$$

Equation (5.46) represents the corrected values of the velocity. When the actual discretized momentum Equation (5.46) is subtracted from the assumed values of discretized momentum Equation (5.45) with source term $u_{i+\frac{1}{2},j}^{t\prime} - 2u_{i+\frac{1}{2},j+\frac{1}{2}}^{t\prime} + u_{i+\frac{1}{2},j+1}^{t\prime}$ set to zero, Equation (5.47) is obtained:

$$u_{i+\frac{1}{2},j+\frac{1}{2}}^{t+1*} = -\frac{\Delta t}{\Delta x}\left(p_{i+1,j+1}^{t\prime} - p_{i+2,j+1}^{t\prime}\right) + u_{i+\frac{1}{2},j+\frac{1}{2}}^{t*} \quad (5.47)$$

By substituting Equation (5.47) in the Equation (5.46), Equation (5.48) is obtained:

$$\left(p_{i+1,j+1}^{t\prime} - p_{i+2,j+1}^{t\prime}\right) = \frac{\Delta t}{\Delta x}\left(u_{i+\frac{1}{2},j+\frac{1}{2}}^{t\prime} - u_{i+\frac{1}{2},j+1+\frac{1}{2}}^{t+1\prime}\right) \quad (5.48)$$

The corrected values of pressure drop are solved by Equation (5.48). After obtaining the values of corrected pressure drop and velocity, the actual pressure drop and velocity are solved by the Equations (5.49) and Equation (5.50) respectively:

$$\Delta p = \Delta p^{*} + \alpha \Delta p' \quad (5.49)$$

$$u = u^{*} + \alpha_{ur} u' \quad (5.50)$$

Δp^{*} is the pressure drop of the previous iteration.

$\Delta p'$ is the corrected pressure drop.

u^{*} is the velocity of the previous iteration.

u' is the corrected velocity.

α_{ur} is the under relaxation factor which is assumed to be 0.8. This is assumed suitably for the convergence criteria.

The inlet velocity is assumed to satisfy the laminar flow condition. The no slip boundary condition for velocity is assumed at the wall. The solution is obtained by marching in the *x*-axis to solve for pressure drop and in the y-axis to solve for velocity. The algorithm is solved by following steps:

Step 1: Pressure drop in the first time step is assumed between the two grid points suitably in Equation (5.44) to solve for the value of velocity for the next time step.

Step 2: The value of velocity obtained from Equation (5.44) is substituted in Equation (5.47) to determine the pressure drop between the two grid points.

Step 3: The pressure drop value obtained from Equation (5.47) is substituted in Equation (5.46) to get corrected velocity for next time step.

Step 4: The corrected pressure drop value is obtained after substituting the corrected velocity value obtained from Equation (5.46) in Equation (5.48). From the corrected pressure drop and assumed pressure drop values the actual pressure drop for first time step is calculated from Equation (5.49). Similarly velocity is also determined from Equation (5.50).

The steps from 1 to 4 are repeated for further time steps until the convergence in the pressure drop value is obtained.

5.3.7 Lax Wandroff Explicit Method

The Lax-Wandrof explicit method is used to find temperature at different nodes in the x and y axes. The Dirichlet boundary condition is specified at the bottom wall of the channel. This temperature is obtained from the Fourier law of heat conduction equation determined from the experiment. The values obtained for pressure drop and velocity from the Navier-Stokes equations are substituted in the energy equation and solved by Equation (5.51).

$$T_{i+1,j+1}^{t+1} = \frac{\Delta t}{\Delta x Cp}\left(p_{i+1,j+1}^{t} - p_{i+2,j+1}^{t}\right) + \frac{k\Delta t}{\Delta x^2 Cp}\left(T_{i,j+1}^{t} - 2T_{i+\frac{1}{2},j+1}^{t} + T_{i+1.j+1}^{t}\right) + \frac{k\Delta t}{\Delta y^2 Cp}\left(T_{i+1,j}^{t} - 2T_{i+1.j+1/2}^{t} + T_{i+1.j+1}^{t}\right) + \frac{\mu\Delta t}{\Delta y^2 Cp}\left(u_{i+1,j}^{t} - u_{i+1,j+1}^{t}\right)^2 \quad (5.51)$$

5.3.8 Grid independence study

The pressure drop, velocity and temperature are calculated by numerical techniques such as pressure correction method and the Lax Wendroff explicit method. The grid independence for the pressure drop of water at heat flux=90.4 kW/m^2 and mass flux=76.67 kg/m^2-s and inlet temperature=303 K is checked. The change in pressure drop and temperature of water are not very significant. The grid size of 15 X 8 are chosen in the present study.

5.3.9 Subcooled flow boiling heat transfer coefficient and Bubble void fraction

The variation of bubble void fraction and heat transfer coefficients of mixtures with different ethanol volume fractions are shown in Figure 5.10.

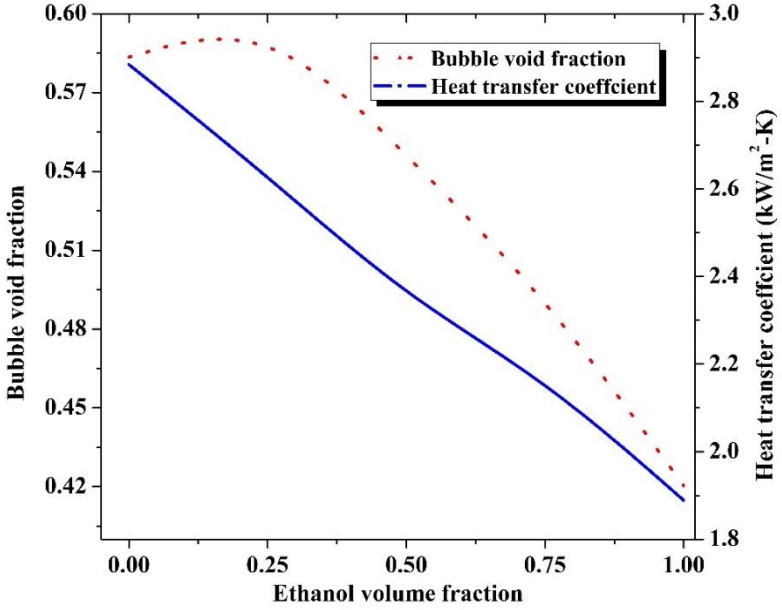

Figure 5.10: Variation of Subcooled flow boiling heat transfer coefficient and bubble void fraction with ethanol volume fraction

Out of 1459 frames 15 frames are considered to solve for bubble void fraction and heat transfer coefficients. This procedure is followed for water-ethanol mixture of different ethanol volume fractions (25%, 50%, 75% and 100%). It can be seen that bubble void fraction and subcooled flow boiling heat transfer coefficient decreases with increase in ethanol volume fraction. The bubble void fraction is obtained from the bubbles that are

formed on the surface. The bubble void fraction is determined from the still images at various frames. The still images depict the bubbles which are attached to the wall surface. Inititially heat transfer coefficient decreases with the bubble formation. This is because the bubble acts as a vapour blanket and thus prevents the heat transfer from the wall to the surrounding liquid. But it is seen that when the bubble departs from the surface the heat transfer coefficient increases. The bubble condenses into the subcooled part of the flowing liquid and acts as an energy carrier and thus increases the heat transfer coefficient. The formation of bubbles decrease with increase in ethanol volume fraction. The reason for the decrease in bubble formation with increase in ethanol volume fraction is supported from the bubble dynamic study given in section 6.4. Variation of heat transfer coefficient with ethanol volume fraction is shown in Figure 5.11.

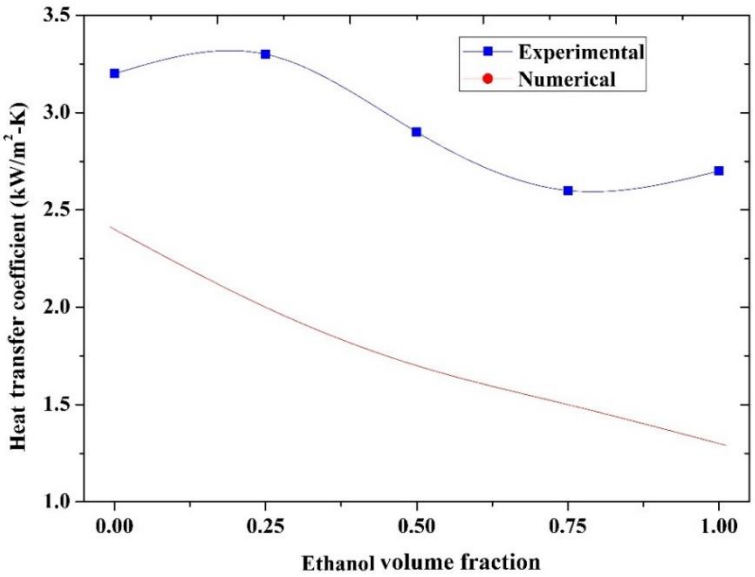

Figure 5.11: Comparison of Numerical result with that of the Experiment at heat flux=90.4 kW/m^2.

It is seen that the experimentally determined heat transfer coefficient is highest for 25% ethanol volume fraction and lowest for 75% ethanol volume fraction. But the numerically determined heat transfer coefficient decreases with addition of ethanol to water. The average deviation of 24.13 % is observed for subcooled flow boiling heat transfer coefficient of water-ethanol mixture when compared with that of experiment. The reason

being that, only the bubble void fraction is determined and substituted in the thermophysical and thermodynamic properties and effect of Marangoni convection is not considered. The deviations is observed due to following assumptions.

1. Flow is assumed to be one dimensional, hence change in velocity in the axial direction is negligible. Velocity changes only along normal direction as per law of velocity profile.
2. Effect of nucleation and hydrodynamic instabilities during the subcooled flow boiling are not considered in the simulation.
3. Uniform wall temperature boundary condition is assumed at the channel wall surface. The change in heated wall temperature does not change with time steps.
4. The thermodynamic and thermophysical properties are obtained from bubble void fraction from the mixture rule. These properties are assumed to be constant with change in time steps.
5. Effect of vapour generation rate, forces due to lift, drag and dispersion is not incorporated in the *x*-momentum and energy equations because the heat transfer coefficient is determined from the bubble volume of fraction which are obtained from still images.
6. Mixture composition vapour phase is assumed to be constant and same as liquid phase composition.

CHAPTER 6

RESULTS AND DISCUSSION ON BUBBLE DYNAMICS

The experimental results of bubble dynamics of water-ethanol mixture are presented in this chapter. The results include the bubble departure diameter, waiting period, growth period and also the bubble images at different test conditions. Bubble dynamic data are correlated based on mechanistic approach.

6.1 BUBBLE DEPARTURE DIAMETER

6.1.1 Size distribution of bubble departure diameter

The bubble departure diameter is one of the important parameters to understand boiling phenomenon. The departure diameter, growth period and waiting period are dependent on nucleation sites (Frederic et al. 2014). Average of 20 to 30 bubbles are considered during departure from 3 to 4 sites to measure the bubble departure diameter. The size distribution of these bubbles follows the Gaussian distribution curve as shown in Figure 6.1. The size distribution is given in Equation (6.1).

$$f(size) = \frac{N(d_i)}{\sum_{i=1}^{\infty}[N(d_i)(d_{i+1}-d_i)]} \tag{6.1}$$

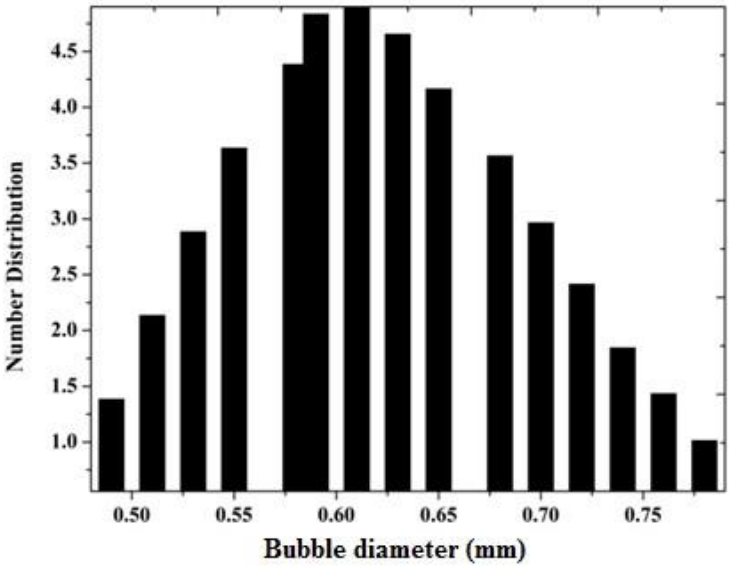

Figure 6.1: Size distribution for bubble departure diameter of water at heat flux=90 kW/m^2 and mass flux=76.67 kg/m^2-s.

6.1.2 Validation of bubble departure diameter

Despite several efforts over many years, there are only a few correlations for bubble departure diameter. Fritz derived a simple correlation for bubble departure diameter which was a balance between surface tension and buoyancy force (Marko and Bostjan, 2012). Few correlations were proposed with considerations of pressure, superheat and wettability effects. Cole and Rohsenow (1969) correlated bubble departure diameter for various fluids at low pressure which is given by Equation (6.2).

$$d_{dep} = C\sqrt{\frac{\sigma_s}{\rho(\rho_l - \rho_v)}}\left(\frac{\rho_l C_{pl} T_{Sat}}{\rho_g h_{fg}}\right)^{5/4} \tag{6.2}$$

Some researchers developed different approach to determine the bubble departure diameter based on heat transfer mechanisms. Kurul and Podowski (1970) derived the correlation for bubble departure diameter by balancing the heat supplied to the wall with the heat used to grow a bubble by evaporating underlying micro layers which is represented by Equation (5.3).

$$d_{dep} = 0.00014 + 10^{-4} T_{sub} \tag{6.3}$$

Zuber and Forster (1954) included the effect of non-uniform temperature field and gave the bubble radius as represented by Equation (6.4).

$$d_{dep} = \frac{4b}{\sqrt{\pi}} Ja\sqrt{\alpha_l t} \tag{6.4}$$

In the present work, Equation (6.5) is used to nondimensionalise the bubble departure diameter and is applicable for both inertia controlled and diffusion controlled stages (Mikic and Roshnew, 1969).

$$d^+ = \frac{2r_{dep}}{B^2/A} \tag{6.5}$$

Where constant A and B are defined as,

$A = \left(\frac{b\,\Delta T h_{fg}\rho_v}{T_{sat}\rho_l}\right)^{0.5}$ $B = \left(\frac{12}{\pi} Ja^2 \alpha_l\right)^{0.5}$ $b = \frac{\pi}{7}$ for bubble growth on the surface of channel wall.

Comparison of measured bubble departure diameter in dimensionless form with the available literature correlations is shown in Figure 6.2.

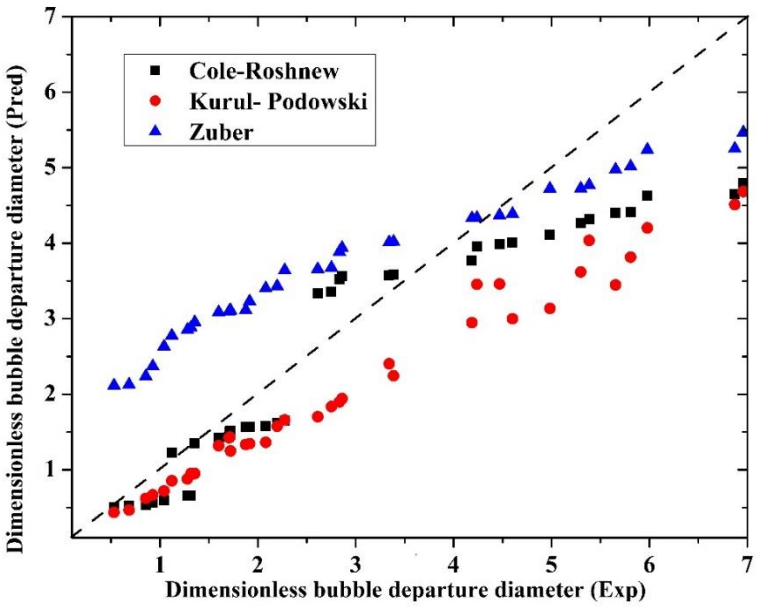

Figure 6.2 : Validation of bubble departure diameter.

Cole-Roshnew Correlation predicts the experimental data with mean absolute error (MAE) of 31.4% and 85% of experimental data are under predicted by the correlation. Kurul-Podowski correlation under predicts the experimental data with MAE of 38.1%. Zuber correlation predicts the experimental data with MAE of 32.9% and 65% of experimental data are over predicted. Cole-Roshnew correlation is based on force balance approach and Kurul-Podowski and Zuber correlations are based on heat balance approach. The force balance approach predicts the present experimental data better when compared to heat balance approach.

6.1.3 Effect of heat flux and mass flux

Figure 6.3 shows the variation of dimensionless bubble departure diameter with mass flux at different heat flux. It is observed that the bubble departure diameter decreases with increase in mass flux and decreases with increase in heat flux. Sugrue et al. (2014) had conducted subcooled flow boiling experiment for water in a vertical channel. They also found that bubble departure diameter decreased with increase in mass flux and heat flux.

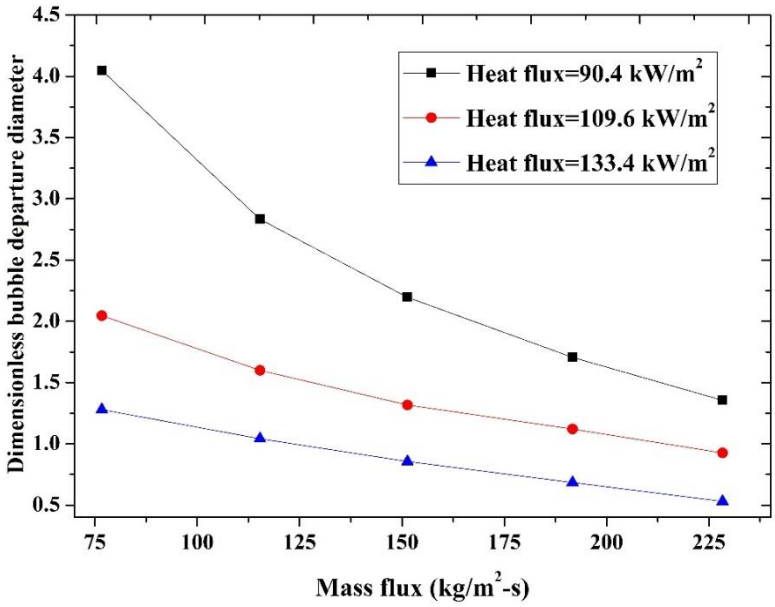

Figure 6.3: Variation of dimensionless bubble departure diameter with mass flux for water at different heat flux and at inlet temperature=303 K.

When the bubble is formed in the active nucleation sites, it coheres at the channel wall due to surface tension between the channel wall-vapour interfaces. Surface energy of channel wall tends to pull the molecules of local vapour causing wetting of the channel surface known as wettability. The wetting of surface is dependent on the contact angle between the channel wall surface (solid-vapour interface) and the bubble. When contact angle increases, the wettability decreases and bubble departs from the surface. At higher heat flux, mass flux and at lower inlet temperature of the fluid, the surface tension between the channel wall and the vapour decreases due to decrease in surface energy. The surface energy decreases at higher heat flux, mass flux and at lower inlet temperature of water because (i) Buoyancy, inertia and pressure forces increase due to increase in evaporation at higher heat flux. This pulls the bubble away from the channel wall surface and decreases the surface tension between the solid-vapour interfaces. (ii) At higher mass flux, the bulk liquid pushes the bubble downstream and this also causes decrease in surface tension between the solid-vapour interfaces.

Surface tension in the vapour-liquid interface increases in order to overcome the loss of surface tension between channel wall-vapour interfaces. This attracts the surface of

the bubble towards the liquid causing increase in vapor-liquid interface pressure and buoyancy of the bubble. Initially, the formation of bubbles reduces the overall heat transfer due to thin vapour layer of bubbles providing thermal resistance. But the surface tension of the vapour-liquid interface is higher than the inertial force of the liquid and the bubbles depart at faster rate. This reduces the bubble departure diameter and thus increases the heat transfer coefficient. Departed bubble acts as an energy carrier and increases the overall heat transfer coefficient of the liquid. This phenomenon is observed at higher heat flux and higher mass flux.

At higher heat flux, heat transfer coefficient increases due to early bubble departure and formation of more number of active nucleation sites. But at higher mass flux, the bubble departs at early stage and active nucleation site formation is reduced due to decrease in wall temperature. Therefore, effect of increase in heat flux on heat transfer coefficient is more significant when compared with that of mass flux.

6.1.4 Effect of inlet temperature

Figure 6.4 shows the variation of dimensionless departure diameter with mass flux at different inlet temperature.

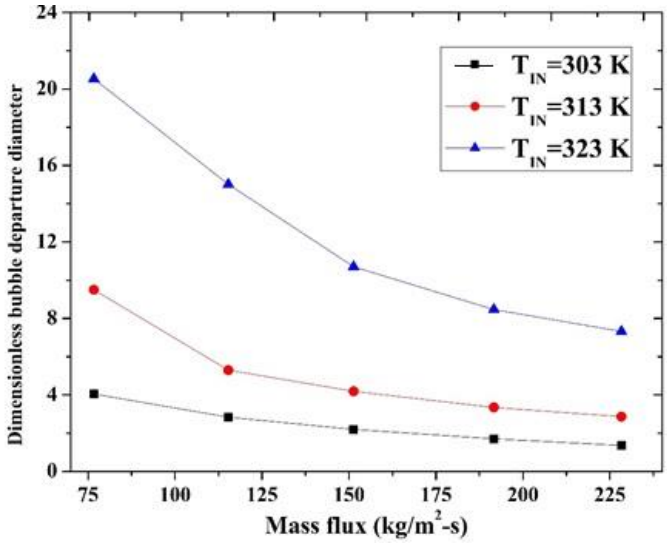

Figure 6.4: Variation of dimensionless bubble departure diameter with mass flux for water at different inlet temperature and at heat flux = 90.4 kW/m^2.

It is seen that bubble departure diameter increases with increase in inlet temperature, because at higher inlet temperature the bubbles adhere to wall due to decrease in surface tension between the liquid-vapour interfaces. Su et al. (2010) conducted numerical investigation on bubble dynamics during flow boiling of water. In their research it was found that the bubble departure diameter decreased with increase in subcooling, i.e decrease in inlet fluid temperature.

6.2 BUBBLE GROWTH PERIOD AND WAITING PERIOD

The photographic images of bubble growth of water at different heat flux, mass flux and inlet temperature are shown in Figure 6.5 to 6.8. In the images some of the bubbles are larger in size. They are the coalesced bubbles and are not considered for measuring the bubble departure diameter. The photographic images of bubble formation for water-ethanol mixtures at constant heat flux of 90.4 kW/m^2, mass flux of 115.33 kg/m^2-s and inlet temperature of 303 K are shown in Figures 6.9 to 6.12. The bubble images of water-ethanol mixture at different test conditions are shown in APPENDIX E.

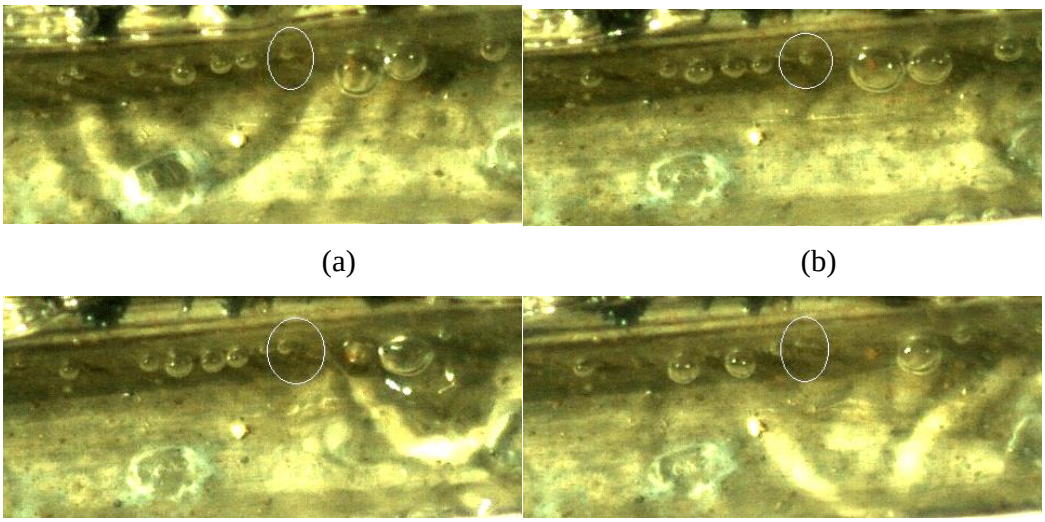

(a) (b)

(c) (d)

Figure 6.5: Bubble growth and waiting period for water at heat flux=90.4 kW/m^2, inlet temperature=303 K and mass flux = 228.3 kg/m^2-s (a) Bubble nucleation at 0 ms (b) Bubble in growth stage at 6.23 ms (c) Bubble departure at 12.45 ms (d) Next bubble nucleation at 28.9 ms after the departure.

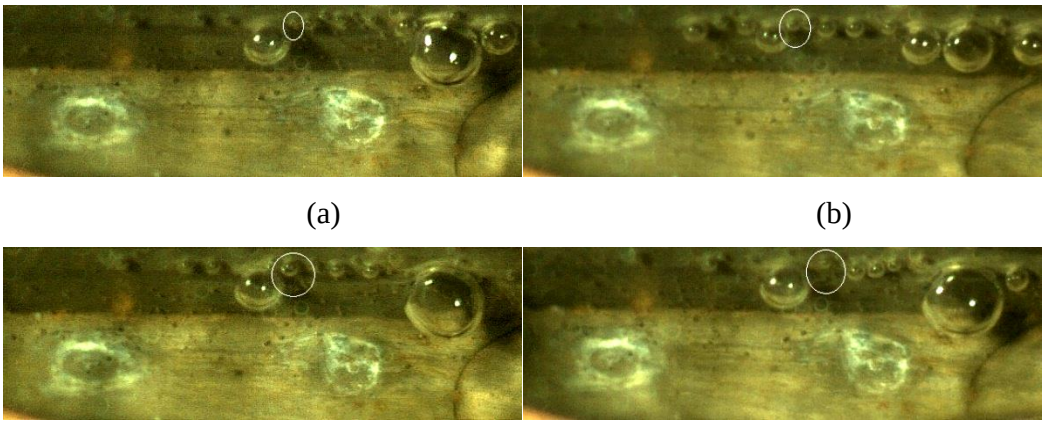

(a) (b)

(c) (d)

Figure 6.6: Bubble growth and waiting period for water at heat flux=133.47 kW/m^2 , inlet temperature=303 K and mass flux = 76.67 kg/m^2-s (a) Bubble nucleation at 0 ms (b) Bubble in growth stage at 3.24 ms (c) Bubble departure at 6.48 ms (d) Next bubble nucleation at 18.54 ms after the departure.

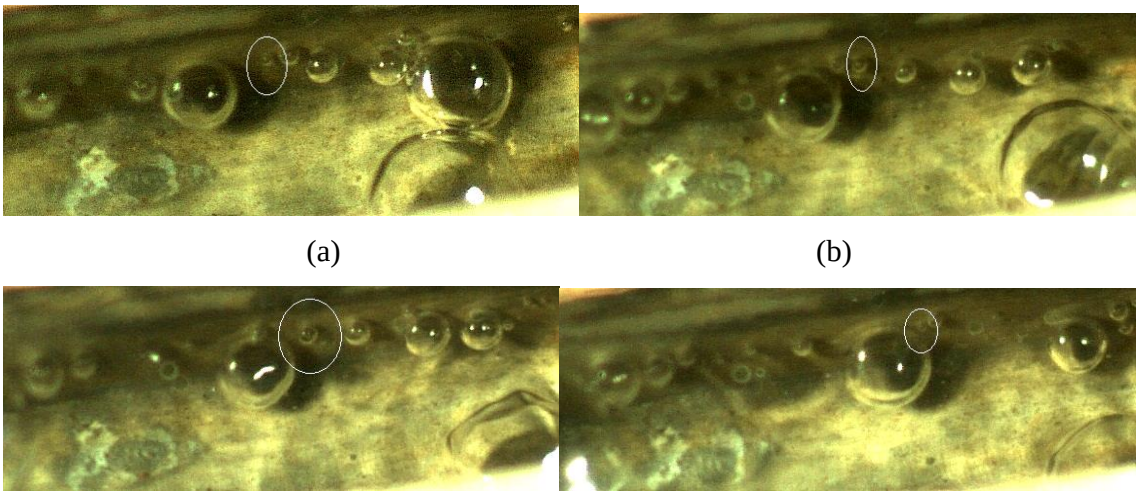

(a) (b)

(c) (d)

Figure 6.7: Bubble growth and waiting period for water at heat flux=133.47 kW/m^2 , inlet temperature=303 K and mass flux = 228.33 kg/m^2-s (a) Bubble nucleation at 0 ms (b) Bubble in growth stage at 2.39 ms (c) Bubble departure at 4.78 ms (d) Next bubble nucleation at 13.97 ms after the departure.

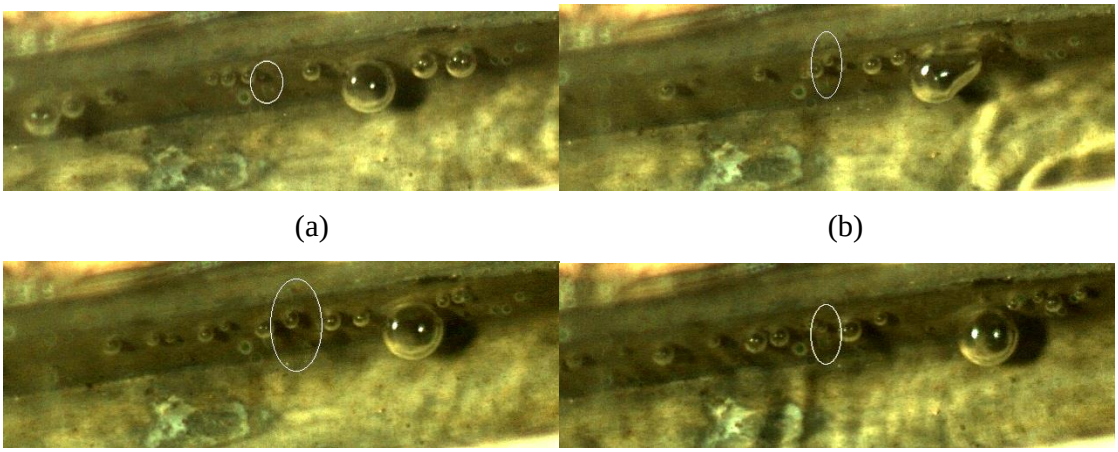

(a) (b)

(c) (d)

Figure 6.8: Bubble growth and waiting period for water at heat flux=133.47 kW/m^2 , inlet temperature=313 K and mass flux =76.67 kg/m^2-s (a) Bubble nucleation at 0 ms (b) Bubble in growth stage at 5.45 ms (c) Bubble departure at 10.89 ms (d) Next bubble nucleation at 26.57 ms after the departure.

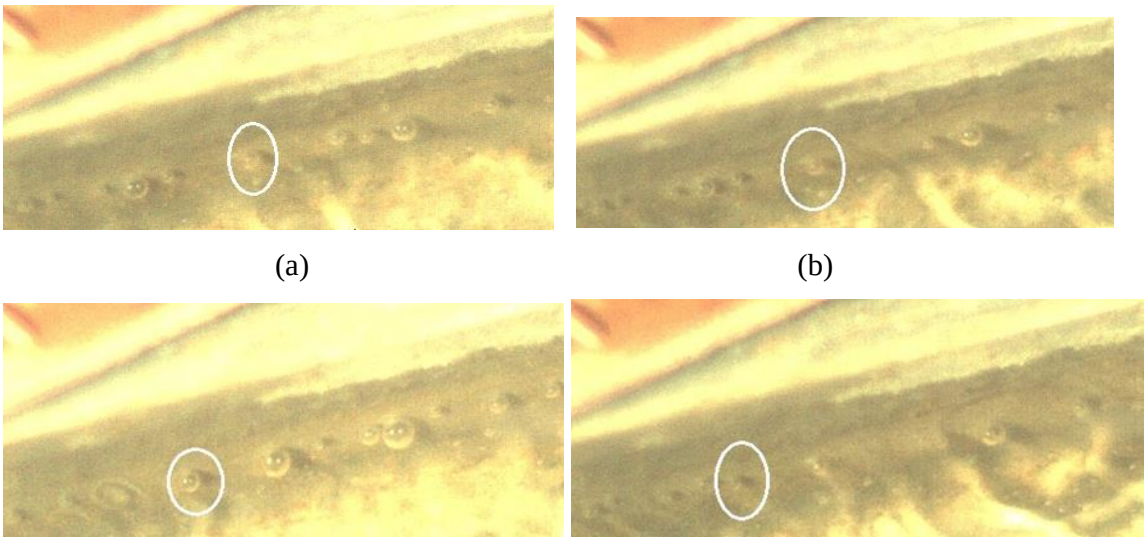

(a) (b)

(c) (d)

Figure 6.9: Bubble growth and waiting period for water-ethanol mixture of ethanol volume fraction 25% at heat flux=90.4 kW/m^2, inlet temperature=303 K and mass flux = 115.33 kg/m^2-s (a) Bubble nucleation at 0 ms (b) Bubble in growth stage at 5.18 ms (c) Bubble departure at 10.35 ms (d) Next bubble nucleation at 26.72 ms after the departure.

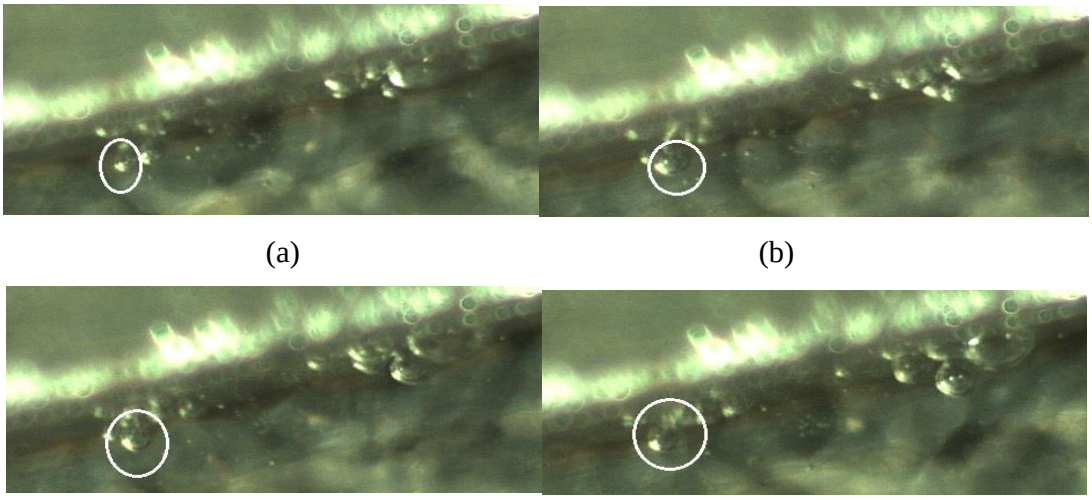

(a) (b)

(c) (d)

Figure 6.10: Bubble growth and waiting period for water-ethanol mixture ethanol volume fraction 50% at heat flux=90.4 kW/m^2, inlet temperature=303 K and mass flux= 115.33 kg/m^2-s (a) Bubble nucleation at 0 ms (b) Bubble in growth stage at 10.44 ms (c) Bubble departure at 15.47 ms (d) Next bubble nucleation at 32.62 ms after the departure.

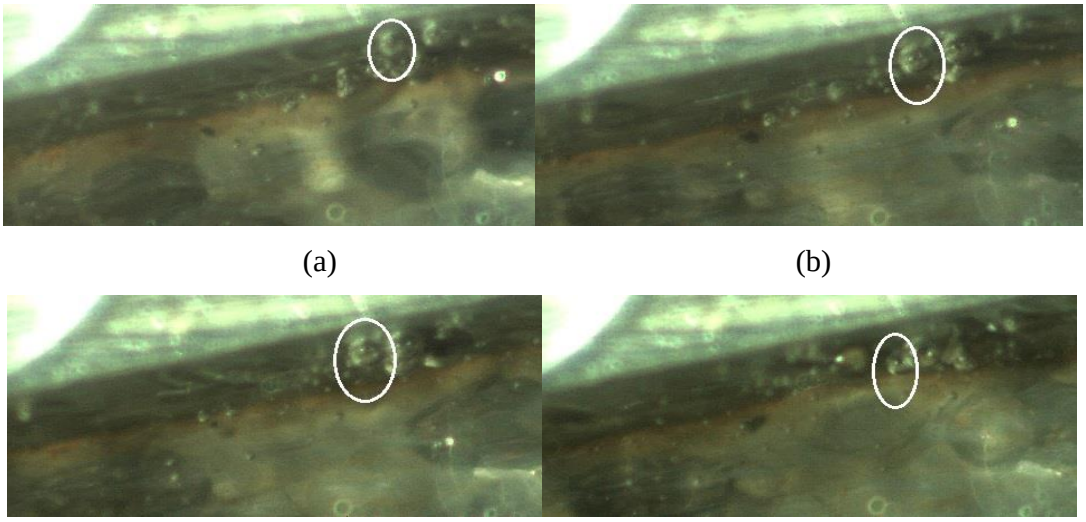

(a) (b)

(c) (d)

Figure 6.11: Bubble growth and waiting period for water-ethanol mixture of ethanol volume fraction 75% at heat flux=90.4 kW/m^2, inlet temperature=303 K and mass flux = 115.33 kg/m^2-s (a) Bubble nucleation at 0 ms (b) Bubble in growth stage at 13.68 ms (c) Bubble departure at 18.73 ms (d) Next bubble nucleation at 37.84 ms after the departure.

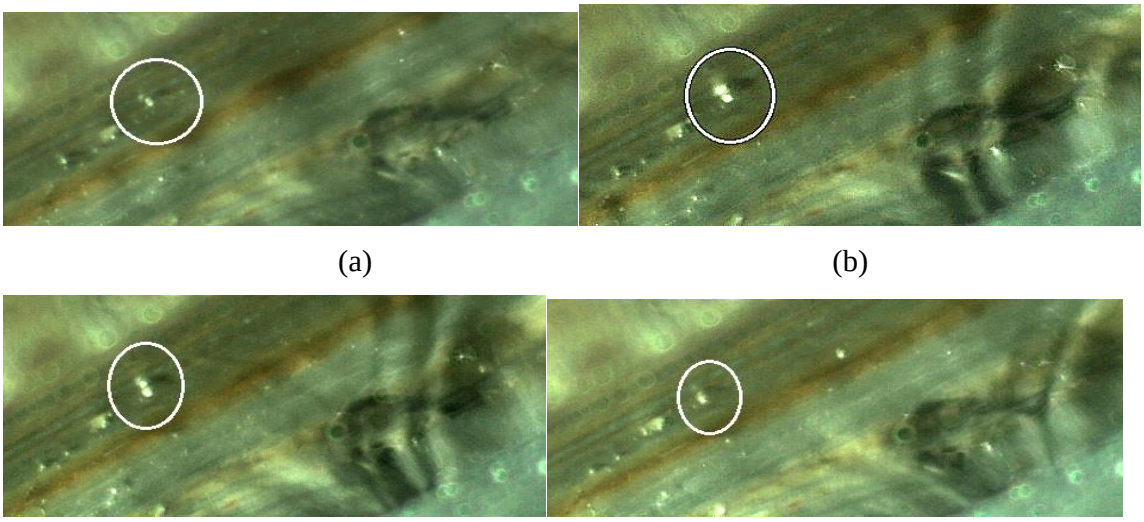

(a) (b)

(c) (d)

Figure 6.12: Bubble growth and waiting period for ethanol at 90.4 kW/m^2 and mass flux=115.33 kg/m^2-s and inlet temperature=303 K. (a) Bubble nucleation at 0 ms (b) Bubble in growth stage at 12.36 ms (c) Bubble departure at 18.75 ms (d) Next bubble nucleation at 33.62 ms after the departure.

6.2.1 Effect of heat flux and mass flux on bubble growth period

Figure 6.13 shows the variation of dimensionless bubble growth period (t^+) with mass flux for different heat flux.

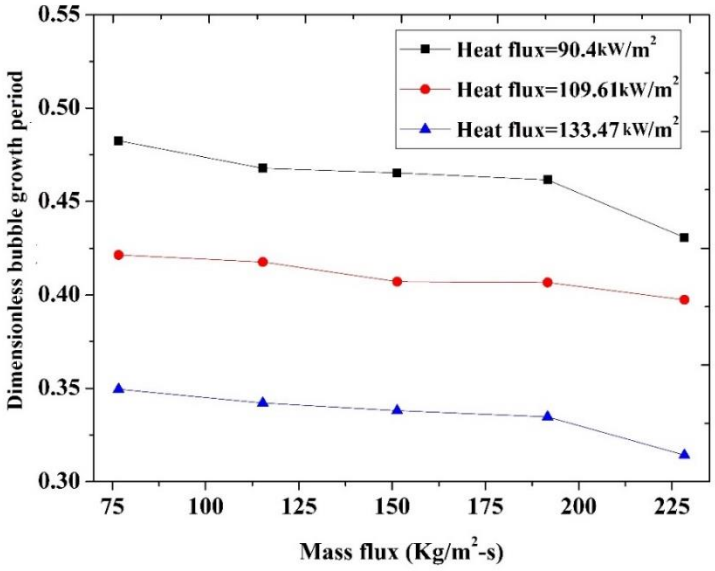

Figure 6.13: Variation of dimensionless bubble growth period with mass flux for water at different heat flux.

The time period from bubble nucleation to departure is called growth period. The time period from the bubble departure to the next bubble nucleation is called waiting period. In the present experiment the bubble growth period is measured by number of frames required to capture the bubble from its nucleation to departure. Bubble waiting period is measured by number of frames required to capture the next bubble to nucleate from the same site from which the previous bubble had departured. The number of frames required for bubble growth and nucleation of next bubble is divided by the total number of frames in one second to obtain bubble growth and waiting periods. The value reported is the average value of 20 to 30 bubbles from 3 to 4 sites.

The dimensionless bubble growth period is obtained by dividing the bubble growth period with the total period. The total period is the sum of growth period and waiting period. It can be seen that the growth period decreases with increase in heat flux and mass flux. But the influence of heat flux is observed to be more significant than mass flux. At higher heat flux and mass flux sufficient amount of energy is acquired by the fluid and it overcomes intermolecular force of the molecules causing change in phase of liquid locally. This causes bubbles to depart from the surface and thus reduces the bubble growth period.

6.2.2 Effect of inlet temperature on bubble growth period

Variation of dimensionless bubble growth period with mass flux for various inlet temperature is shown in Figure 6.14. It can be observed that the bubble growth period increases with increase in inlet temperature. Higher inlet temperature reduces the heat transfer coefficient due to increase in thermal boundary layer thickness and thus causing increase in growth period. At higher inlet temperature the bubbles adhere to wall because of decrease in surface tension between the liquid-vapour interfaces and thus increases the bubble growth period.

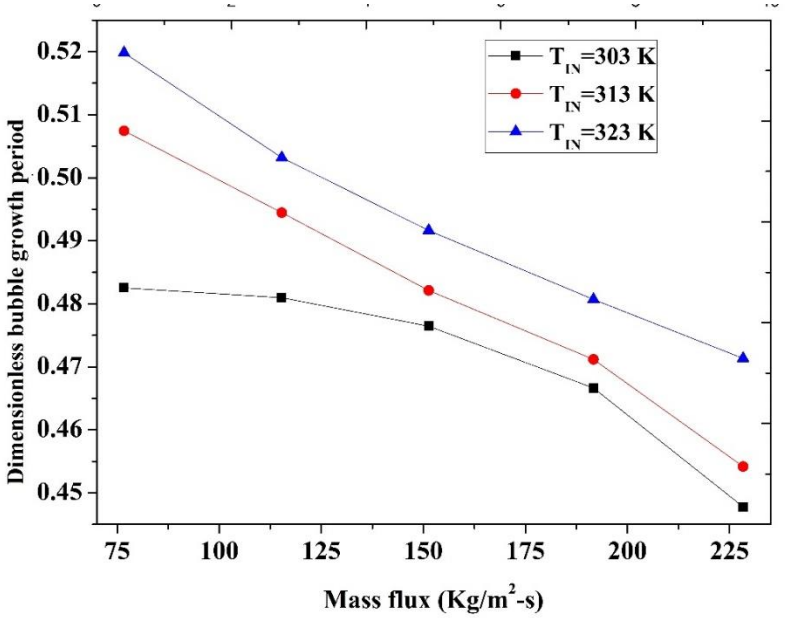

Figure 6.14: Variation of dimensionless bubble growth period with mass flux for water at different inlet temperature.

6.2.3 Relation between bubble growth period and bubble waiting period

The variation of dimensionless bubble diameter with dimensionless growth period of bubble for different mass flux is shown in Figure 6.15. Dimensionless bubble diameter is obtained by dividing the instantaneous bubble diameter during the growth stage to bubble departure diameter. Dimensionless growth period is obtained by dividing the instantaneous time during the growth stage to time taken for bubble to depart. The dimensionless bubble diameter increases with increase in dimensionless time. During the bubble growth period a high rate of energy is extracted from the heater surface, which leads to significant temperature drop beneath the bubble (Surgue et al. 2014). The clusters of water molecules escape as vapour in the form of bubbles at faster rate. This reduces the size of bubble due to early growth and departure. The early bubble departure decreases the bubble growth period and bubble departure diameter size and thus increases the heat transfer coefficient. After the departure of bubble, the molar latent heat of vaporization increases. Hence more heat is available to break the intermolecular force of liquid in the same site and decreases the waiting period of bubble and heat transfer coefficient. Therefore the bubble growth period (t_g) increases with increase in waiting period (t_w) as shown in Figure 6.16.

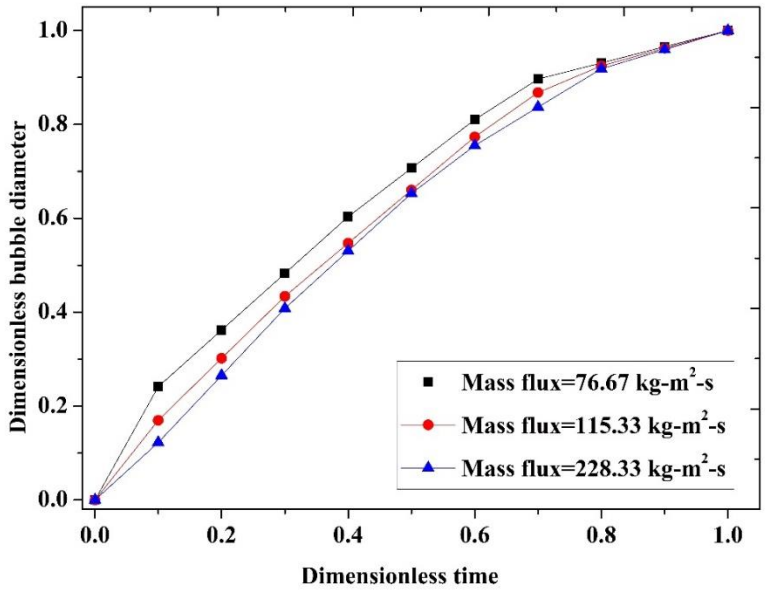

Figure 6.15: Variation of dimensionless bubble departure diameter with dimensionless time for water.

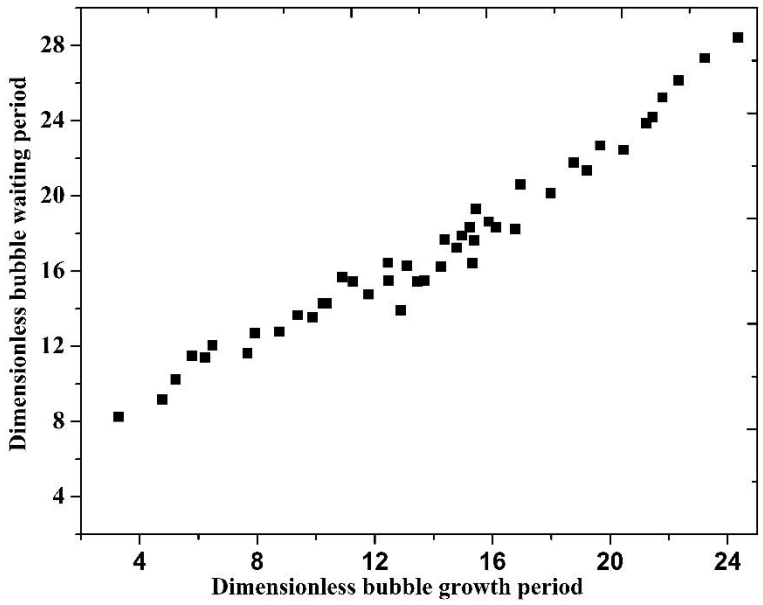

Figure 6.16: Variation of dimensionless waiting period of bubbles with dimensionless growth period of bubbles for water.

6.3 EFFECT OF ETHANOL VOLUME FRACTION ON BUBBLE DEPARTURE DIAMETER

The variation of dimensionless bubble departure diameter with ethanol volume fraction at various inlet temperature and mass flux is shown in Figure 6.17 (a). It is observed that the bubble departure diameter decreases with the addition of ethanol to water inititially upto 25% ethanol volume fraction, but with further addition of ethanol, the bubble departure diameter increases. This is the reason for highest values of heat transfer coefficient for mixture with 25% ethanol volume fraction and lowest for mixture with 75% ethanol volume fraction as shown in Figure 6.17(b).

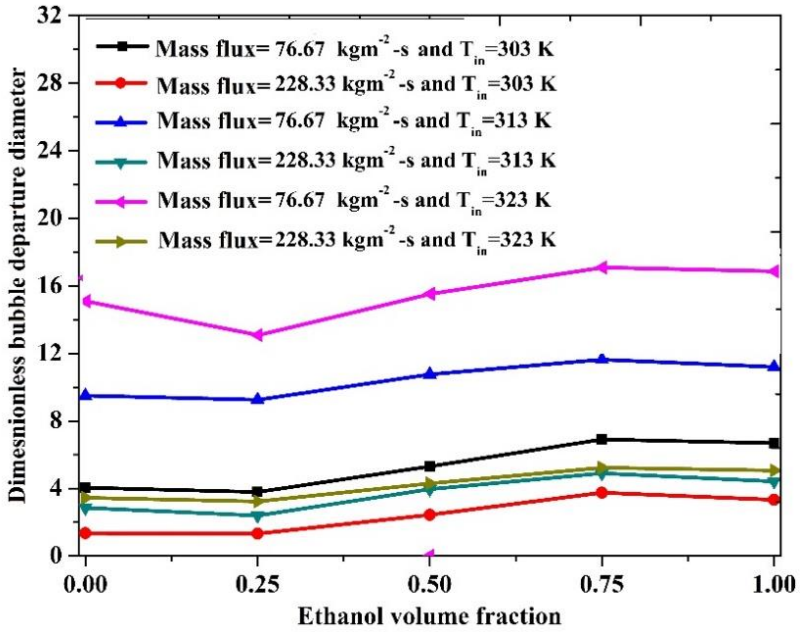

Figure 6.17 (a): Variation of dimensionless bubble departure diameter with ethanol volume fraction.

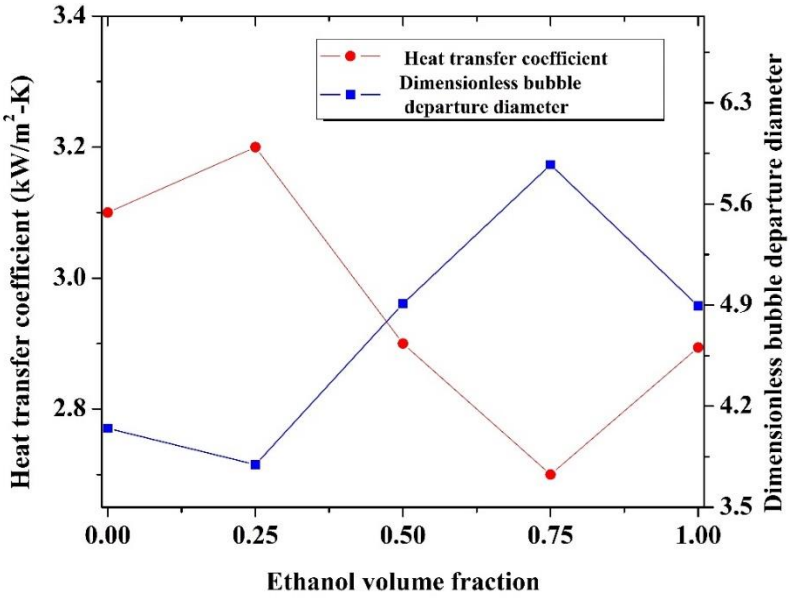

Figure 6.17 (b): Variation of dimensionless bubble departure diameter and subcooled flow boiling heat transfer coefficient with ethanol volume fraction.

Thermal conductivity and thermal capacity of ethanol is lower than that of water. Molar entropy of vaporization of ethanol is marginally higher than water. Entropy is due to the molecules that are held together in liquid by polar attractions and hydrogen bonding. Hence more energy is required to pull these molecules of liquid. Molar latent heat of vaporization is slightly greater which actually results in higher heat transfer coefficient of ethanol (James Green, 2011). But Trouton's rule states that due to lower boiling point of ethanol, it has lower molar enthalpy of vaporization when compared with that of water (Lyklema, 1999). Hence the addition of ethanol to water delays the departure of bubbles, thus decreasing heat transfer to the surrounding liquid causing an increase in bubble departure diameter. Delay in departure increases the time gap between departure of first bubble and nucleation of next bubble resulting in decrease of active nucleation sites and thus the bubble formation. Therefore, the subcooled flow boiling heat transfer coefficient decrease and bubble departure diameter increase at mixtures with 50% and 75% ethanol volume fraction. But in contrast the active nucleation sites are highest for 25% and lowest for 75% ethanol volume fraction as shown in Figure 6.18 (a) to Figure 6.18 (e). The reason for such phenomena can also be explained by force balance approach during the bubble departure.

At 25% ethanol volume fraction, the surface tension force dominates force developed due to unsteady bubble growth and quasi-static drag force which are parallel to flow direction. Surface tension force between the liquid-vapour interface is larger when compared to other volume fractions. This leads to early departure of the bubble. The early bubble departure reduces the waiting period and thus increases the bubble frequency. The increased frequency of the bubble increases the heat transfer to the subcooled portion of the liquid because the departed bubbles act as an energy carrier.

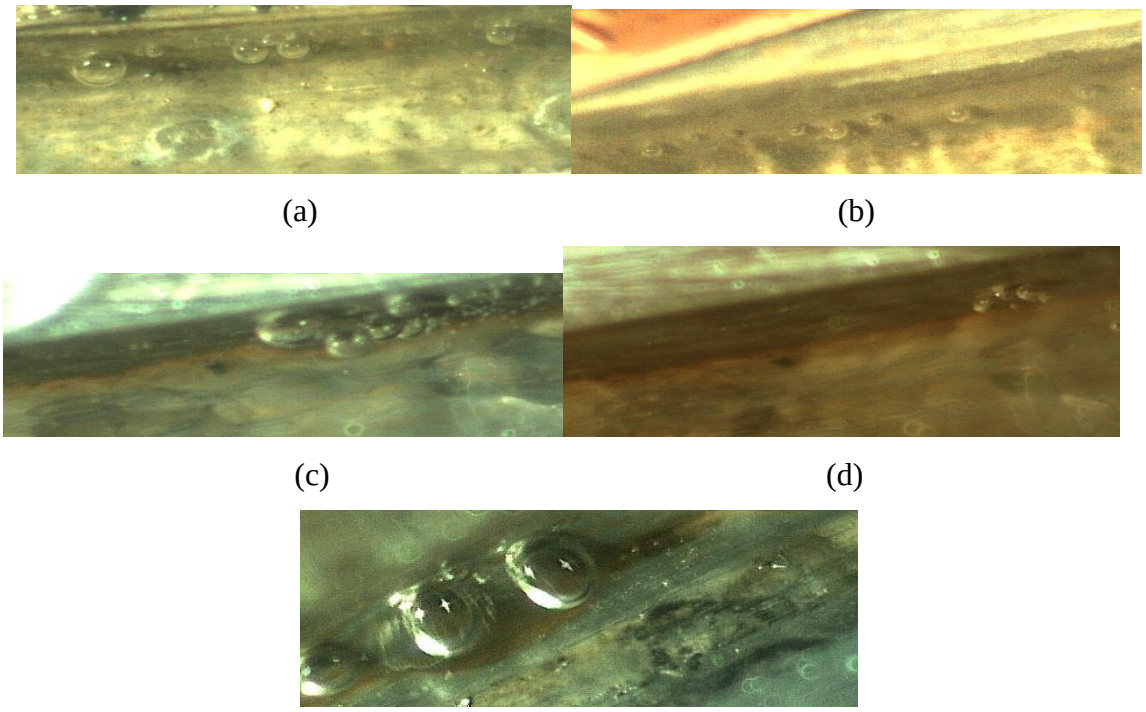

(a) (b)

(c) (d)

(e)

Figure 6.18: Bubble formation at heat flux=90.4 kW/m^2, inlet temperature=303 K and mass flux=76.67 kW/m^2. (a) water (b) 25% ethanol volume fraction (c) 50% ethanol volume fraction (d) 75% ethanol volume fraction (e) ethanol.

6.4 FORCE BALANCE

Klausner et al. (1993) and Zeng et al. (1993) conducted force balance which included the effect of various forces acting on a bubble. These forces are due to surface tension, contact pressure, unsteady drag, unsteady growth, lift, and buoyancy. These forces significantly

affected the bubble departure and bubble lift off. In the present work, their approach is used to calculate these forces acting on the bubble.

The forces acting on the bubble in the parallel and normal direction to flow are given by Equations (6.7) and (6.8) respectively.

$$\sum F_x = F_{sx} + F_{qs} + F_{du}cos\theta \tag{6.7}$$

$$\sum F_y = F_{sy} + F_{sL} + F_b + F_h + F_{cp} + F_{du}sin\theta \tag{6.8}$$

Force due to surface tension in parallel direction is given by Equation (6.9)

$$F_{sx} = -1.25 d_{dep} \sigma_s \frac{\pi(\alpha_a - \beta_r)}{\pi^2 - (\alpha_a - \beta_r)^2} \tag{6.9}$$

α_a and β_r are advancing and receding angles. These angles can be estimated through $\alpha_a = \theta + 10$ and $\beta_r = \theta - 10$ (Yeoh et al. 2005). Quasi static force acting on the bubble in parallel direction can be calculated by Equation (6.10).

$$F_{qs} = \frac{1}{2} C_D \rho_L \Delta U^2 r_{dep}^2 \tag{6.10}$$

C_D is drag coefficient and is determined by Zuber and Ishii correlation (1979) as given by Equation (6.11).

$$C_D = \frac{2}{3}\left(\frac{g(\rho_l - \rho_g)}{\sigma_s}\right)^{0.5} \tag{6.11}$$

Force due to unsteady growth can be calculated by using Equation (6.12)

$$F_{du} = -\rho_l \pi {r_{dep}}^2 \left(\frac{3}{2} C_s \frac{dr}{dt} + r_{dep} \frac{d^2 r}{dt^2}\right) \tag{6.12}$$

where r_{dep} is the bubble departure radius, ΔU is the relative velocity between the bubble and flowing liquid. In the present work, the average of 20 sliding bubbles is considered with respect to time. The bubble velocity is calculated by measuring the distance of a bubble for the time interval between the two images. The displacement of bubble is obtained by subtracting bubble center of two successive images. Gray-scale centroid method is applied to calculate the coordinate of bubble center based on gray image. The bubble velocity is calculated by Equation (6.13).

$$u_{bub} = \frac{x_{c1} - x_{c2}}{\Delta t} \tag{6.13}$$

The bubbles included are (i) departed and sliding and (ii) departed, sliding and lift-off bubbles.

Force due to surface tension in normal direction is calculated by Equation (6.14)

$$F_{sy} = -d_{dep}\sigma_s \frac{\pi}{\alpha-\beta} (cos\beta_r - cos\alpha_a) \quad (6.14)$$

The dynamic actions on the vapour-liquid interface within the quasi-static regime permit the application of the Young-Laplace equation for a departing bubble yielding upward force due to contact pressure (Frederic et al. 2013) as given by the Equation (6.15).

$$F_{cp} = \frac{\pi d_{dep}^2}{4} \frac{2\sigma}{r_r} \quad (6.15)$$

r_r is radius of curvature of the bubble at the reference point on the surface, i.e, radius of curvature at the base of the bubble. The radius of curvature is considered as $r_r = 5r_{dep}$ (Klausner et al. 1993). The radius that is in contact with the surface quantifies capillary force.

For the calculation of force due to buoyancy spherical bubble assumption is used and is given by Equation (6.16). This is an approximation since the contact with the surface truncates the bubble (Frederic et al. 2013).

$$F_b = \frac{4}{3}\pi r_{dep}^3 (\rho_l - \rho_g) g \quad (6.16)$$

The hydrostatic and lift forces are calculated by Equation (6.17) and (6.18).

$$F_h = \frac{9}{8}\rho_l \Delta U^2 \frac{\pi d_{dep}^2}{4} \quad (6.17)$$

$$F_{sl} = \frac{1}{2} C_L \rho_L \Delta U^2 r_{dep}^2 \quad (6.18)$$

Where C_L= 0.8 *G*s.

*G*s is the dimensionless shear rate given by the gradient dv/dy and is calculated by Equation (6.19).

$$Gs = \frac{du}{dy}\frac{r_d}{\Delta v} \quad (6.19)$$

Gradient du/dy can be calculated from the universal velocity profile for turbulent flow which is given by Equation (6.20).

$$\frac{u}{u_\tau} = 2.43\ ln\ y^+ + 5 \quad (6.20)$$

The velocity profile in Equation (6.20) is assumed to be the average time velocity distribution at channel surface of the wall. The value of y^+ in the present experiment

exceeds 30 which is found to be in the logarithmic layer. The friction velocity is substituted in Equation (6.19) to find the gradient du/dy.

The growth of a bubble is influenced by forces acting in parallel and normal directions to the horizontal heating surface. For horizontal subcooled flow boiling, forces acting on the bubble in the parallel direction influence the bubble sliding on the heated wall, whereas, the forces acting in the normal direction causes the bubble lift-off. Jakob number plays a vital role to understand the relation between the force balance and heat transfer. Jakob number is the ratio of sensible heat to latent heat. Forced convection is dependent on the sensible heat and subcooled boiling is dependent on the local latent heat. During subcooled flow boiling the forced convection is dominated by evaporation and agitation. Hence the heat transfer coefficient decreases with increase in Jakob number. The variation of ratio of parallel force to the normal force (F_x/F_y) with Jakob number is shown in Figure 6.19. It is seen that at Jakob number lower than 20, (F_x/F_y) is found to be higher than 1. At Jakob number above 20, (F_x/F_y) is found to be lower than 1.

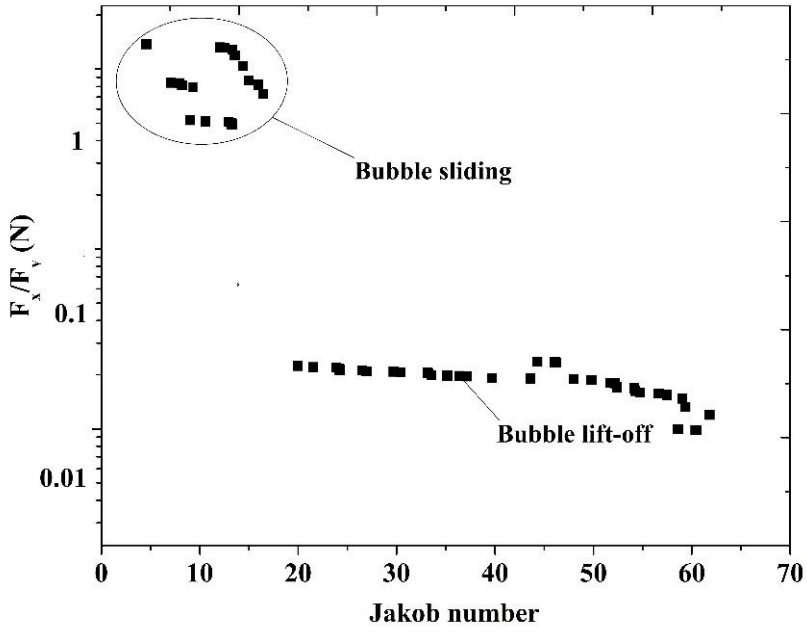

Figure 6.19: Variation of (F_x/F_y) with Jakob number.

When (F_x/F_y) is less than 1, it is observed that bubble departed and lifted off from the heated surface of channel wall but did not slide. When (F_x/F_y) is greater than 1, the bubble departed from the surface of the channel wall and slide. The detached bubbles grew slightly during sliding along the heated surface of the channel. But when the bubble lifts off, it condenses immediately into the subcooled portion of the liquid. Thus the rate of condensation will be higher than the rate of evaporation when compared with that of bubble sliding. Hence bubble sliding has higher heat transfer than the bubble lift off. Tomio et al (2012) also observed similar results.

Bubble causes change in the flow field which results in the variation of quasi-steady drag force (F_{qd}) and surface tension force acting on it. These forces are balanced by unsteady growth rate (F_{du}). Due to the initial immobility and the very small growth rate of bubble in subcooled liquid, change in F_{qs} is not much significant. The breaking of the force balance in flow direction is caused by the sudden variation of the surface tension force between the wall and the liquid interface. The bubble contact diameter and the contact angles change due to the evaporation in the triple-phase line region at the bubble root during bubble growth. The force balance in flow direction is broken by the disturbance from the main flow which alters the contact diameter and the contact angle, leading to the change of the surface tension force (Sathish Kandlikar et al. 2002). This is achieved at higher mass flux and therefore the bubble departs at early stage. The bubble begins to slide along the heated wall. Even though the force balance acting on the bubble in flow direction suddenly brakes, it will recover soon due to the adaptive surface tension force caused by the flexibility of the bubble-liquid interface. This causes the bubble to slide. The bubble lift-off after departure without sliding does not cause significant increase in heat transfer because the bubble gets condensed into the subcooled liquid in the outer region of boundary layer. But during sliding the bubble movement causes the micro layer evaporation beneath the bubble and carries as energy carrier. This increases the temperature gradient beneath the bubble to cause an increase in heat transfer. During bubble lift-off the sum of hydrodynamic pressure and surface tension force will be lower than contact pressure force, shear lift force, unsteady growth force and buoyancy force (Liaofei et al. 2015).

The Jakob number increases with increase in ethanol volume fraction. Therefore increase in ethanol volume fraction decreases the heat transfer coefficient. But in contrast, for mixture with 25% ethanol volume fraction bubble sliding is observed similar to that of water. Therefore marginal increase in heat transfer coefficient is observed at this mixture composition when compared with that of water. However, the bubble lift off occurs without sliding for 75% ethanol volume fraction and ethanol.

6.5 HYDRODYNAMIC INSTABILITY

Flow instabilities are undesirable in flow boiling. Flow oscillations affect the local heat transfer coefficient. The two kinds of flow instabilities which are identified in subcooled flow boiling are nucleation instability and oscillatory instability.

6.5.1 Nucleation Instability

The nucleation instability is caused by vaporization of the local liquid which results in increase in specific volume of the local liquid. The finite amount of wall superheat is required to initiate bubble nucleation at the heated surface. Under this condition, the bubbles grow and eject into the subcooled portion of the flow. This process will cool the remaining liquid and the heated surface of channel wall, until the required degree of super heat is reestablished for further nucleation. It depends mainly on the geometry of the system and fluid properties. Therefore it may be observed that nucleation instability increases at higher ethanol volume fraction resulting in obtaining lower heat transfer coefficient.

6.5.2 Oscillatory instability

When a bubble is formed and departed from the heated surface, disturbance occurs in the flow. In the mixture, ethanol being volatile component evaporates first. Bubble formed due to evaporation of this volatile component compresses the surrounding liquid while growing and then leaves the wall surface. The compressible volume created due to compression of the bubble into the surrounding fluid due to motion. The inertia of the flow from the compressible volume will cause reduction in local pressure at the heated inlet of the channel. This causes to and fro motion in the channel surface leading to compression of vapor boundary layer. The rarefaction wave also passes through the surface, thus

expanding and contracting the thermal boundary layer. Usually, this phenomenon is observed at higher volume fractions and higher inlet temperatures.

6.6 CORRELATION DEVELOPMENT BASED ON BUBBLE DYNAMICS DATA

The subcooled flow boiling heat transfer coefficient is a function of $\rho, \Delta U, d_{dep}, \mu, k, f, N_a$ and σ_s i.e, $h = f(\mu, \rho, \Delta U, d_{dep}, k, f, N_a, \sigma_s)$. The properties and parameters chosen are combined as dimensionless numbers by Buckingham's π-theorem. These dimensionless numbers are:

$\pi_1 = \frac{\sigma_s}{\rho \Delta U^2 d_{dep}}$, $\pi_2 = \frac{d_{deb} f}{\Delta U}$, $\pi_3 = N_a d_{deb}^2$ and $\pi_4 = \frac{h d_{dep}}{k}$,

Equation (4.51) and Equation (4.52) are used to determine the active nucleation site density of bubbles (N_a).

$$N_a = 0.34 \times 10^4 (1 - cos\theta) \Delta T_W^2 \qquad \Delta T_{ONB} < \Delta T_w < 15K \tag{4.51}$$

$$N_a = 0.34 \times 10^4 (1 - cos\theta) \Delta T_W^{5.3} \qquad 15K < \Delta T_w \tag{4.52}$$

Bubble frequency (*f*) is calculated by Equation (4.53)

$$f = \frac{1}{t_w + t_g} \tag{4.53}$$

These numbers can be expressed as $\pi_4 = f(\pi_1, \pi_2, \pi_3)$. The independent dimensionless numbers (π_1, π_2 and π_3) which significantly influence the dependent dimensionless number (π_4) are chosen for developing the correlation. The variation of π_4 due to addition of independent dimensionless numbers are shown in Figure 6.20 to Figure 6.22. MAE is 6.14 % for π_4 vs. π_2. MAE is 5.88 % for π_4 vs. $\pi_2 \pi_3$, 5.51 % for π_4 vs. $\pi_2 \pi_3 \pi_1$.

$\pi_2 = \frac{d_{deb} f}{\Delta U}$ *and* $\pi_3 = N_a d_{deb}^2$ are key factors. This shows that the bubble departure diameter and bubble frequency are the dominating factors in the present correlation. The correlation is obtained after the regression analysis as shown in Equation (6.21). Final form of the correlation is given by Equation (6.22).

$$\frac{h d_{dep}}{k} = 41.02 \left(\frac{\sigma_s}{\rho \Delta U^2 d_{dep}} \right)^{0.022} \left(\frac{d_{deb} f}{\Delta U} \right)^{0.031} (N_a d_{deb}^2)^{0.011} \tag{6.21}$$

$$Nu_{sub,b} = 41.02 \, \frac{{St_{rl}}^{0.031} {Na*}^{0.011}}{{We_{dep}}^{0.022}} \tag{6.22}$$

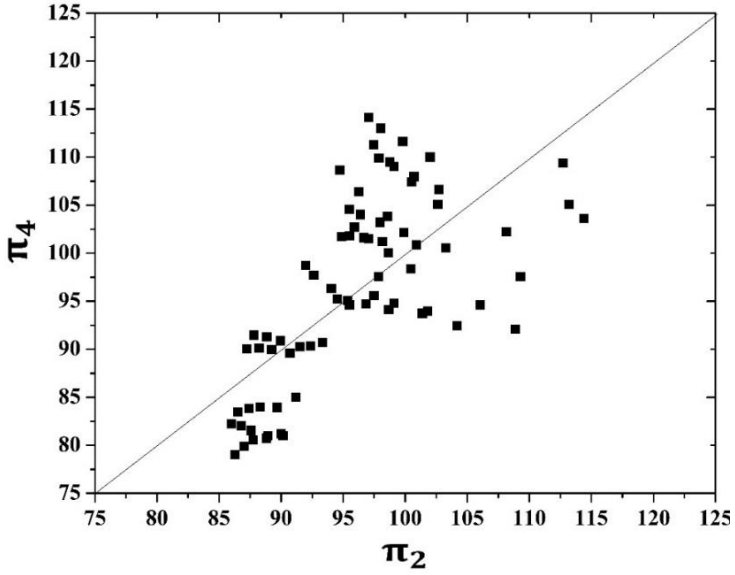

Figure 6.20: $\pi_4 \, vs. \, \pi_2$

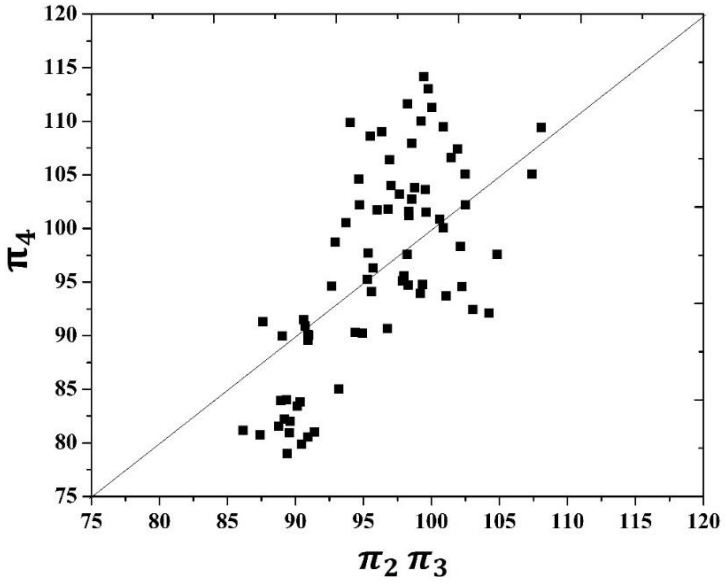

Figure 6.21: $\pi_4 \, vs. \, \pi_2 \, \pi_3$

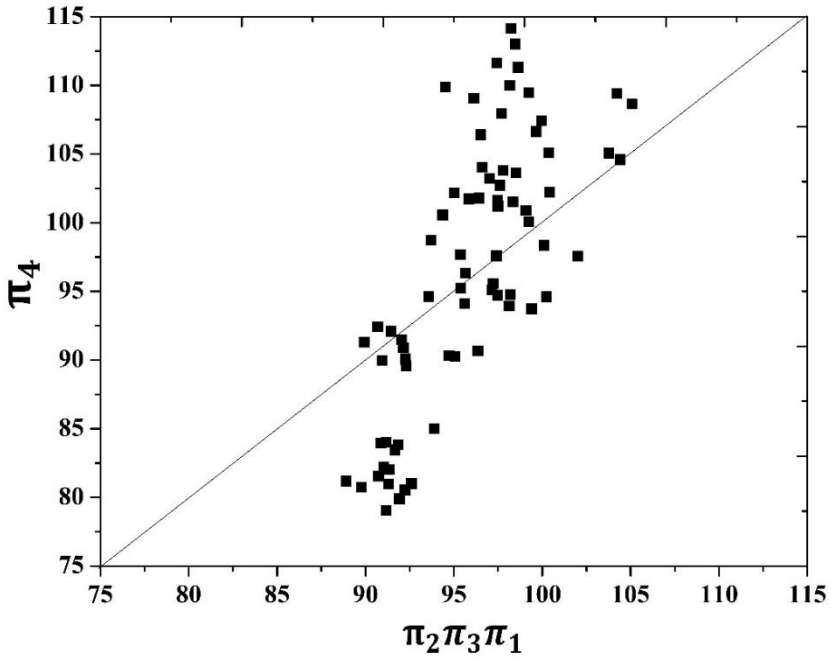

Figure 6.22: $\pi_4\ vs.\ \pi_2\ \pi_3\ \pi_1$

6.6.1 Significance of dimensionless number $\boldsymbol{\pi_2 = \frac{d_{deb}f}{\Delta U}}$

$\pi_2 = \frac{d_{deb}f}{\Delta U}$ is termed as bubble strouhal number. The heat transfer coefficient decreases with increase in bubble departure diameter. In contrary, the term departure diameter is in the numerator. The decrease in bubble departure is dominated by increase in bubble frequency. Heat transfer coefficient increases with increase in bubble frequency. Bubble frequency increases due to decrease in both the bubble waiting period and the bubble growth period. Increase in bubble departure diameter reduces the bubble velocity due to resistance offered by the bubble inertia to the flow. Thus these phenomena significantly affects the heat transfer process. The effect of strouhal number at higher volume fraction leads to oscillatory instability.

6.6.2 Significance of dimensionless number $\boldsymbol{\pi_3 = N_a d_{deb}^2}$

The pre-existing gas nuclei in the sites causes heterogeneous nucleation. The volume of air trapped in a cavity depends on the magnitude of surface tension, contact angle, shape of the cavity, and the experimental conditions, such as system pressure, liquid temperature, and temperature of the heated surface. The wall temperature at which nucleate boiling

begins strongly depends on the availability of cavities with trapped gases. Thus, as cavities become fewer and fewer and their size decreases, the nucleation temperatures will approach homogeneous nucleation temperature (Sathish Kandlikar et al. 2007). Therefore degassing removes the trapped gases in the liquid and it is assumed that there are no pre-existing trapped gases in the liquid. The nucleation site density is assumed to be homogenous in the present study.

The forced convective heat flux, evaporative heat flux and agitation heat flux cause the phase change of the liquid in the sites causing homogeneous nucleation. The agitation heat flux is usually present in the onset of vapour generation (OSV) region of fully developed nucleate boiling regime during the subcooled flow boiling. The phase change causes the bubble generation and these two phenomena affect the heat transfer in the liquid. Phase change is due to the latent heat transfer from wall to the surface and the departed bubble acts as an energy carrier. The early bubble departure decreases the size of the bubble and the bubble moves away quickly. This is observed at higher heat flux and mass flux. At higher mass flux, the bubble departs at early stage, but active nucleation site formation is reduced due to decrease in wall temperature. Therefore, effect of increase in heat flux on heat transfer coefficient is more significant when compared with that of mass flux. Therefore the product of the active nucleation site density and the bubble departure diameter are the significant parameters for heat transfer.

6.6.3 Comparison of bubble dynamic approach with heat transfer approach

The correlation developed using the bubble dynamic data is compared with the correlation developed using heat transfer approach is shown in Figure 6.23. It is observed that 70 % of the predicted data lie within $\pm 15\%$ error when compared with those predicted using heat transfer approach correlation. The MAE of Nusselt number for water predicted using the bubble dynamic approach and those predicted with heat transfer approach is 11.38%.

- The Nusselt number of water calculated from the experiment and those predicted from the bubble dynamic data is shown in Figure 6.24. It is found that 70.33 % of predicted data lie within $\pm 15\%$ error when compared with those predicted with

experimental data. The MAE of Nusselt number for water predicted using the bubble dynamic correlation and those predicted with experimental data is 7.53 %.

- The MAE of Nusselt number of water calculated from the experiment and those predicted from the heat transfer approach correlation is 10.89% as shown in Figure 4.21. It can be seen that the bubble dynamic approach predicts the heat transfer coeffient better when compared with heat transfer approach.

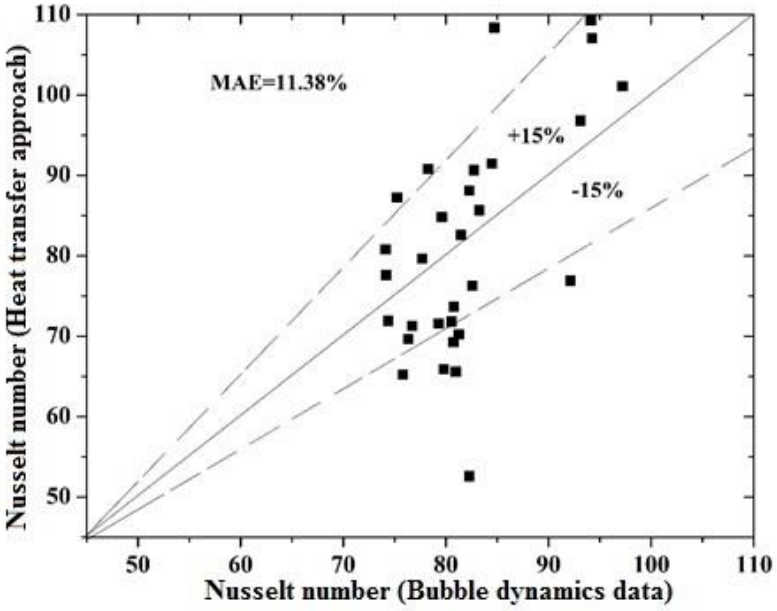

Figure 6.23: Comparison of correlation based on heat transfer approach with the correlation based on bubble dynamic approach.

The higher accuracy can be attributed to the following reasons: The heat flux increases with increase in wall superheat for both forced convection and subcooled boiling region. But the increase in heat flux is higher in the subcooled boiling region. The boiling curves closely merge into a single curve for different values of mass fluxes. During the commencement of onset of nucleate boiling (ONB), bubbly flow occurs. In bubbly flow, the liquid micro layer film is formed due to evaporation. The bubbly flow also continues in highly subcooled onset of vapour generation (OSV) region. The micro layer acts as a blanket preventing the decrease in wall temperature. The increase in mass flux decreases

the wall temperature in forced convection region but the wall superheat do not vary significantly due to increase in mass flux at subcooled boiling region.

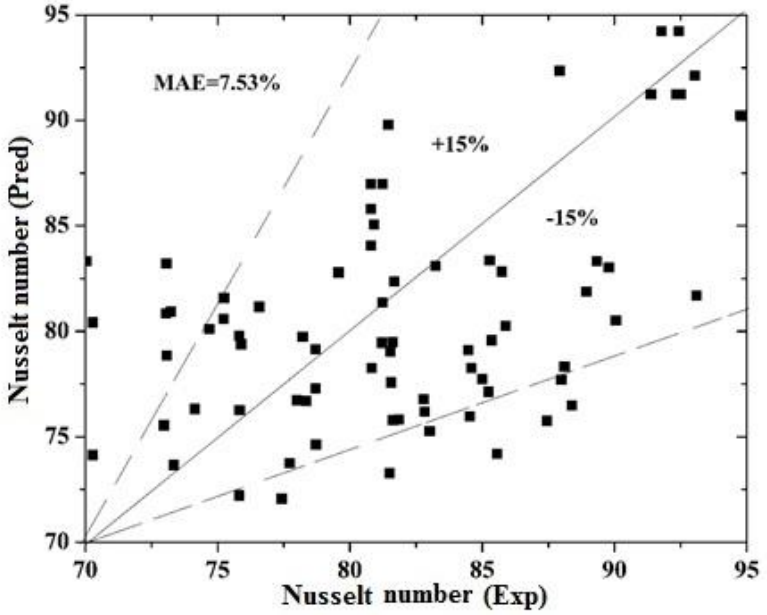

Figure 6.24: Comparison of correlation based on bubble dynamics data with the experimental data.

As the mass flux increases, the wall temperature decreases due to i) diffusion of the bubbles which are departed from corners and ii) formation of lesser activated nucleation sites at the bottom wall of the channel. Decrease in wall temperature decreases the wall superheat. This shows that increase in mass flux has negligible influence on heat transfer in this region. During ONB the bubble formation commences. The active nucleation sites occur due to micro layer evaporation in the corner of bottom wall of the channel. However, flow in the middle portion of the channel is subcooled. Higher mass flux contributes towards convective mode of heat transfer, but the convective heat transfer is dominated by vapour turbulence in the flow. The bubble is subjected to variation of surface tension force, causing the bubble to depart from the surface and thus drags the adjacent warm layer of fluid. This causes local vapour momentum forces to act in the flow. These local vapour momentum forces dominate the convective mode of heat transfer to increase the heat transfer coefficient.

At higher heat flux, the buoyancy and inertial force are significant than surface tension force. The bubbles detach and depart from the corner and enter the subcooled region. With further increase in heat flux, the vapour generation commences. This region is highly subcooled region. This results in the increase in activated nucleation sites and also flow of surrounding fluid into the nucleation sites. The higher heat flux also leads to early departure of the bubbles from the sites, thus increasing the bubble frequency. The bubble frequency increases due to decrease in waiting period and growth period of the bubbles. This causes vapour turbulence and agitation, which causes the heat flux contribution towards the subcooled boiling heat transfer and dominates the forced convective heat transfer. Therefore, the heat transfer coefficient increases with increase in heat flux and mass flux, but increase in mass flux is insignificant to increase the subcooled flow boiling heat transfer coeffient as shown in Figures 4.8(a) and 4.8 (b).

From the above explained phenomena, it can be concluded that the nucleation sites, bubble frequency and bubble departure diameter play major role in heat transfer. Hence due to the presence of nucleation sites and bubble departure diameter terms in the correlation developed by bubble dynamic data, the prediction accuracy is better when compared with that of heat transfer approach.

CHAPTER 7

CONCLUSIONS AND SCOPE OF FUTURE WORK

This research work was primarily conducted to understand the aspects of subcooled flow boiling heat transfer to water-ethanol mixture. Forced convective and subcooled flow boiling heat transfer coefficients of water-ethanol mixtures have been reviewed, experimentally investigated and analysed. Numerically determined heat transfer coefficients were compared with that of the experiment. Bubble dynamics in subcooled flow boiling of water-ethanol mixture was investigated through visualization using high speed camera. Correlations based on heat transfer approach and bubble dynamic data were developed for subcooled flow boiling Nusselt number of water-ethanol mixtures. The following conclusions can be made on the results of this study.

7.1 FORCED CONVECTION AND SUBCOOLED FLOW BOILING

- Heat transfer coefficient of water-ethanol mixture increases with increase in heat flux and mass flux in forced convection and subcooled flow boiling regions. The effect of mass flux is significant in forced convection region and the effect of heat flux is significant in subcooled flow boiling region.
- Forced convective heat transfer coefficient of water-ethanol mixture decreases with increase in ethanol volume fraction.
- Increase in inlet temperature decreases the heat transfer coefficient in both the regions for water-ethanol mixture.
- It is observed that the subcooled flow boiling heat transfer coefficient increases with the addition of ethanol to water inititially upto 25% ethanol volume fraction, but at 50% and 75% ethanol volume fractions the heat transfer coefficient reduces. The pure ethanol has marginally higher value than the mixture of ethanol volume fraction 75%.

- It is found that $\pi_3 = \frac{\sigma_s}{\rho v^2 d_h}, \pi_4 = \frac{h_{fg}}{v^2}$ and $\pi_5 = \frac{q''}{\rho v^3}$ are the key factors in the correlation for subcooled flow boiling Nusselt number based on heat transfer approach.
- The Badiuzzaman correlation which consists of subcooling term agrees well with the present correlation in the investigated range of heat flux, mass flux and inlet temperature.
- From the wall heat flux partition analysis, it is found that the heat flux due to forced convection decreases with increase in heat flux at partial and fully developed nucleate boiling regions for water-ethanol mixtures.
- From the numerical analysis it is concluded that the addition of ethanol to water decreases the forced convective and subcooled flow boiling heat transfer coefficient of the water-ethanol mixture.
- The average deviation between the experimentally determined and numerically determined subcooled flow boiling heat transfer coefficient of water ethanol-mixture is 24.13%.

7.2 BUBBLE DYNAMICS

- The size of the bubble departure diameter is highest for mixture of ethanol volume fraction 75% and lowest for mixture of ethanol volume fraction 25%.
- The bubble growth period and waiting period increase with decrease in heat flux and mass flux and with increase in channel inlet temperature.
- The two types of bubble behavior are observed after nucleation are: (i) Lift-off from the bottom wall of the channel surface followed by rapid collapse in subcooled bulk liquid at lower heat flux, and at higher ethanol volume fraction. (ii) Sliding along the bottom wall of the channel surface for a distance and lifting off from the channel wall surface. This is observed at higher heat flux for water and 25% ethanol volume fraction. The effect of mass flux on the bubble sliding or lift-off is not significant.

- When (F_x/F_y) is less than 1, it is observed that bubble departed and lifted off from the heated surface of channel wall but did not slide. When (F_x/F_y) is greater than 1, the bubble departed from the surface of the channel wall and slide.
- It is observed that the prediction accuracy of correlation based on bubble dynamic data is better than that based on heat transfer approach.

7.3 SUGGESTIONS FOR FUTURE WORK

- The present experiment may be extended upto critical heat flux to determine the heat transfer coefficient in the different regimes of boiling. The experiment can be conducted with different binary mixtures.
- The forces acting on the bubbles during subcooled boiling liquid in low-aspect ratio and microchannels may be identified. Repeating these experiments with different binary mixtures for a wide range of aspect ratios would further expand understanding the channel geometries which influences the bubble departure.
- The recently discovered confinement pressure effects deserve extensive experimentation to determine the degree to which these effects influence the flows. Such studies should attempt to demonstrate the additional nucleation due to bubble induced water hammer propagation and add to the dataset of bubble growth rates for a broader range of channels cross-sections and bubble pressures.
- The development of fiber optic sensors will further extend the experimental parameter set to include slug velocity, size, and growth rates as well as allow the first maps in time and space of liquid temperature and void fraction. Such maps would be extremely valuable in understanding the flow instabilities during the boiling.

REFERENCES

Ahmad, S. Y., (1970). "Axial distribution of bulk temperature and void fraction in a heater channel with inlet subcooling", *J. of Heat Transfer* ASME 92: 595-609.

Anthony, J. (2011). "Multi-Objective Design Optimization of Electric Vehicle Battery Cooling Plates Considering Thermal and Pressure Objective Functions"**:** Queens University, Ontario Canada.

Anthony, J and Yong, K.J. (2011). "Design optimization of electric vehicle battery cooling plates for thermal performance". *J. of Power Source* 196, 10359–10368.

Anthony, J and Yong, K.J. (2014). "Influence of operating conditions on the optimum design of electric vehicle battery cooling plates", *J. of Power Sources* 245; 644-655.

Baburajan, Bisht, G.S., Gupta, S.K. and Prabhu, S.V., (2013). "Measurement of subcooled boiling pressure drop and local heat transfer coefficient in horizontal tube under LPLF conditions", *Nucl. Engg. and Design* 255: 169–179.

Badiuzzaman, M. (1967). "Correlation of subcooled boiling data", *Pak. Eng* 7 : 759–764.

Bergles, A.E. and Rohsenow, W.M. (1964). "The Determination of Forced-Convection Surface-Boiling Heat Transfer", *J. of Heat Transfer*, ASME 86:365-372.

Bibeau, E.L and Salcudean, M. (1994). "A study of bubble ebullition in forced-convective subcooled nucleate boiling at low pressures", *Int. J. of Heat Mass Transfer* 37, 2245–2259.

Bjorge, R. W., Hall, G. R., and Rohsenow, W. M., (1982) "Correlation of Forced Convection Boiling Heat Transfer Data," *Int. J. of Heat and Mass Transfer* 25:753–757.

Bowring, R. W (1962). "Physical Model, Based on Bubble Detachment and Calculation of Steam Voidage in the Subcooled Region of a Heated Channel", *Inst. for Atom energie Rep.* HRP- I O, Oslo, Norway 3.

Chen, J. C, (1966,) "A Correlation for Boiling Heat Transfer to Saturated Fluids In Convective Flow," *Indus. and Engg. Chemistry, Process Design and Development* 5: 322-329.

Chin, P., Fu, B.R. and Tsou, M.S. (2012). “Boiling heat transfer and critical heat flux of ethanol–water mixtures flowing through a diverging microchannel with artificial cavities”, *Int. J. of Heat and Mass Transfer* 55: 1807–1814.

Claudi, M. C., (2010). “Flow boiling heat transfer in single channel vertical diameter of small diameter”, Doctoral Thesis, Department of energy technology, Royal institute of technology, Stockholm, Sweden, 47-49.

Cole, R., and Rohsenow, W. (1969). “Correlation of Bubble Departure Diameters for Boiling of Saturated Liquids”, *AIChE Chem. Engg.* Progress Symposium 65: 211–220.

Collier and Thome (1994). “Convective Boiling and Condensation”, McGraw Oxford University, 3: 170-175.

Deam, J.R, and Mattox, R.N., (1970). “Interfacial tension in hydrocarbon systems”, *J. of Chem. Engg. Data*, Wiley Publication : 15, 216– 222.

Flippov, L.P., (1968). “Research of liquid thermal conductivity at Moscow university”, *Int. J. of Heat Mass transfer:* 11, 331-345.

Frederic, J. Lesage and Francis Marois (2013). “Experimental and numerical analysis of quasi-static bubble size and shape characteristics at detachment”, *Int. J. of Heat and Mass Transfer* 64: 53–69.

Frederic, J. Lesage, James, S. Cotton., Anthony J. Robinson (2013). Modeling of quasi-static adiabatic bubble formation, growth and detachment for low Bond numbers, *Chem. Engg. Science* 104: 742–754.

Frederic, J. Lesage, James, S. Cotton and Robinson, A. J., (2014). “A mathematical model for predicting bubble growth for low Bond and Jakob number nucleate boiling”, *Chem. Engg. Science* 112: 35-46.

Fu, X., Zhang, P., Huang, C.J. and Wang, R.Z. (2010). “Bubble growth, departure and the following flow pattern evolution during flow boiling in a mini-tube”, *Int. J. of Heat and Mass Transfer* 53; 4819-4831.

Gerlach, D., (2006)."Comparison of volume-of-fluid methods for surface tension-dominant two-phase flows." *Int. J. of Heat and Mass Transfer* 49: 740-754.

Gorenflo, D., Knabe, V., and Beiling, V., (1986). "Bubble Density on Surfaces with Nucleate Boiling—Its Influence on Heat Transfer", Proc. 8th International Heat Transfer Conference, San Francisco 4, 1995-2000.

Gschwendtner, M.R. (2004). "Experimental investigations on the heat transfer from a moving wall in the case of a rotating cylinder", University of the Federal Armed Forces in Munich / Germany.

Gueyffier, D. (1999). "Volume-of-fluid interface tracking with smoothed surface stress methods for three-dimensional flows." *J. of Comp. physics* 152: 423-456.

Gungor, K.E. and Winterton, R.H.S., (1986), "A general correlation for flow boiling in tubes and annuli*", Int. J. of Heat Mass Transfer* 29: 351-358.

Gunther, F.C, (1951). "Photographic study of surface-boiling heat transfer to water with force convection", *J. of Heat Transfer*; ASME 73, 115–123.

Hajmohammadi, M.R., Salimpour M.R., Saber, M. and Campo, A. (2013). "Detailed analysis for the cooling performance enhancement of a heat source under a thick plate", *Energy Conversion and Management*, 76: 691-700.

Inigo, A., Unai, F.G., Jose, A.R., Javier, S., and Ekaitz, Z. (2013). "Li-Ion Batteries for Automotive Applications", Congress on Numerical Methods in Engineering; Bilbao, Spain, 25-28 June.

James, A.G., Sheeba, J.I. and Richard, H. H. (2011). "Molecular interpretation of Trouton's and Hildebrand's rules for the entropy of vaporization of a liquid", *J. of Chem. Thermodynamics*, 43: 117-130.

Kandlikar, S.G. (1998), "Boiling heat transfer with binary mixture: Part-I, A theoretical modeling for pool boiling", J. of Heat Transfer, ASME 120: 380-387.

Kandlikar, S.G., Masahiro, S. and Vijay, K.D. (1999). "Handbook of phase change:, Taylor and Francis: 79-98.

Kandlikar, S.G. (1998). “Heat Transfer characteristics in partial boiling, fully developed boiling”, *J. of Heat Transfer* 120: 395-401.

Kandlikar, S.G. (2002). “Fundamental issues related to flow boiling in minichannels and microchannels”, *Exp. Thermal and Fluid Science,* 26: 389-407.

Kandlikar, S.G. and Mark, E. S. (2004). “Contact angles and interface behavior during rapid evaporation of liquid on a heated surface”, *Int. J. of Heat and Mass Transfer* 45: 3771–3780.

Kandlikar, S.G., (2004). “Heat transfer mechanisms during flow boiling in microchannels”, *J. of Heat transfer,* ASME 26, 8-16.

Kandlikar, S.G., Das, S.K, Balakrishnan, A.R. (2005). “Analysis of pool boiling heat transfer: effect of bubbles sliding on the heating surface”, *Int. J. of Heat and Mass Transfer* 48: 1543–1553.

Kandlikar, S.G. and Clifford N. H. (2009). “Liquid Cooled Cold Plates for Industrial High-Power Electronic Devices—Thermal Design and Manufacturing Considerations”, *Heat Transfer Engineering*, Taylor and Francis 30: 918–930.

Kurul, N. and Podowski, M.Z. (1990). Multi-dimensional effects in forced convection subcooled boiling. Proceedings of the 9th Heat Transfer conference, Jerusalem, Isreal, Hemisphere Publishing Corporation 2: 21–26.

Klausner, J.F., Mei, R., Bernhard, D.M., Zeng, L.Z. (1993). “Vapor bubble departure in forced convection boiling”, *Int. J. of Heat and Mass Transfer* 36, 651–662.

Kleine, S. J., and McClintock, F. A (1953). “Describing Uncertainties in Single-Sample Experiments,” Mech. Eng, 75: 3–8.

Liaofei, Y., Li, J. and Xu (2015), “Mingchen Experimental investigation on bubble sliding during subcooled flow boiling in microchannel”, *Exp. Thermal and Fluid Science* 68: 435–441.

Lixin, C. and Dieter, M. (2006). “Review of two-phase flow and flow boiling of mixtures in small and mini channels”, *Int. J. of Multiphase Flow*: 32, 183–207.

Lokendra, R. (2010). “Second Law Analysis of a Liquid Cooled Battery Thermal Management System for Hybrid and Electric Vehicles”, Faculty of Engineering and Applied Science, University of Ontario Institute of Technology.

Lyklema, J., (1999), “The surface tension of pure liquids Thermodynamic components and corresponding states, Colloids and Surfaces”, Physicochemical and Engineering Aspects, 156: 413–421.

Marko, M. and Bostjan, K. (2012). “Bubble Departure Diameter Prediction Uncertainty,” *Science and Technology of Nuc. Inst.*, 7. doi:10.1155/2012/863190.

Mcneil, D.A., Raeisi, A.H., Kew, P.A. and Bobbili, P.R. (2010). “A comparison of flow boiling heat transfer in in-line mini pin fin and plane channel flows”, *Applied Thermal Engg.* 30:2412.

Mikic, B.B. and Roshsenow, W.M (1969). “A new correlation of pool boiling data including effect of heating surface characteristics”, *J. of Heat Transfer* ASME 91: 245-250.

Minxia, L., Chaobin, D., and Eiji, H. (2012). “Flow boiling heat transfer of HFO1234yf and R32 refrigerant mixtures in a smooth horizontal tube: Part I. Experimental investigation”, *Int. J. of Heat and Mass* Transfer 55: 3437–3446.

Minxia, L., Chaobin, D., and Eiji, H. (2013). “Flow boiling heat transfer of HFO1234yf and R32 refrigerant mixtures in a smooth horizontal tube: Part II. Prediction method”, *Int. J. of Heat and Mass* Transfer 64: 591-608.

Moharana, M.K., Peela, N.R., Khandekar, S., Kunzru , D. (2011). “Distributed hydrogen production from ethanol in a micro fuel processor: Issues and challenges,” *Renewable and Sustainable Energy Reviews*, 15, 524–533.

Moharana, M.K., Rohan, M., Nemad, E., Khandekar, S. (2013). “Phase change heat transfer of ethanol-water mixtures: towards development of a distributed hydrogen generator”, Proceedings of the ASME Summer Heat Transfer Conference, HT-2013, July 14–19 Minneapolis, Minnesota, USA.

Moles, F.D and Shaw, F.G., (1972), "Boiling heat transfer to subcooled liquids under condition of forced convection", *Trans. Inst. Chem. Eng,* 50: 76–84.

Mukherjee, Kandlikar, S.G., and Edel, J.Z (2011). "Numerical study of bubble growth and wall heat transfer during flow boiling in a microchannel", *Int. J. of Heat and Mass* Transfer 54; 3702-3718.

Liu, Z. and Winterton, R. H. S. (1991). "A General Correlation for Saturated and Subcooled Flow Boiling in Tubes and Annuli Based on a Nucleate Pool Boiling Equation", *Int. J. of Heat Mass Transfer* 34: 2759-2766.

Nilanjana, B., Gopinath, R.W. and Vijay K.D. (2002). "Onset of Nucleate Boiling and Active Nucleation Site Density During Subcooled Flow Boiling", *J. of Heat transfer*, ASME 124: 717-728.

Nilanjana, B., Gopinath, R.W. and Vijay K.D. (2005), "Wall Heat Flux Partitioning During Subcooled Flow Boiling: Part 1—Model Development". *J. of Heat transfer,* ASME, 127, 31-140.

Nilanjana, B., Gopinath, R.W. and Vijay K.D. (2005). "Wall Heat Flux Partitioning during Subcooled Flow Boiling: Part II—Model Validation", *J. of Heat Transfer*, ASME, 127:141-148.

Okawa, T., Ishida, T., Kataoka, I., and Mori, M. (2005). "Bubble rise characteristics after the departure from a nucleation site in vertical up flow boiling of subcooled water", *Nucl. Engg. and Design* 235: 1149–1161.

Papel, S.S., (1963). "Subcooled Boiling Heat Transfer Under Forced Convection in a Heated Tube", Technical Note : D-1583, NASA, Cleveland, OH.

Paz, M.C., Conde, M., Suarez, E and Concheiro, M., (2015). "On the effect of surface roughness and material on the subcooled flow boiling of water", Experimental study and global correlation, *Exp. Thermal and Fluid Science* 64: 114–124.

Ratcliff, G. A. and Khan, M. A., (1971), "Prediction of the viscosities of liquid mixtures by a group solution model", *Canadian J. of Chem. Engg.*, Wiley Publication 49: 125–129.

Reinhold, M. and Thomas, S. (2006). "Bubble and boundary layer behavior in subcooled flow boiling", *Int. J. of Thermal Sciences* 45: 257-268.

Robert, C. R., John, M. P. and Thomas K.S., (1972). "The properties of gases and liquids": McGraw-Hill Book Company, 533.

Ronghua, C., Wenxi, T., Su, G.H., Suizheng, Q., Yuki, I. and Yoshiaki, O. (2010)." Numerical investigation on bubble dynamics during flow boiling using moving particle semi-implicit method", *Nuclear Engg. and Design* 240: 3830-3840.

Rouhollah, A., Tatsuya, U. and Tomio, O. (2012). "Bubble dynamics at boiling incipience in subcooled upward flow boiling", *Int. J. of Heat and Mass Transfer,* 55: 488-497.

Said, Al-Hallaj., Siddique, A., Khateeb, Mohammed., M. Farid, Robert Selman, J. (2004). "Design and simulation of a lithium-ion battery with a phase change material thermal management system for an electric scooter", *J. of Power Sources,* 128: 292–307.

Sarafraz, M.M, Peyghambarzadeh, S.M., Vaeli, N. (2012). Subcooled flow boiling heat transfer of ethanol aqueous solutions in vertical annulus space. *Chem Ind Chem Eng* Q 18:315–327.

Sarma, P.K., Srinivas ,V., Sharmab, K.V., Subrahmanyam ,T and S. Kakac., (2008). "A correlation to predict heat transfer coefficient in nucleate boiling on cylindrical heating elements", *Int. J. of Thermal Sciences* 47: 347–354.

Sekoguchi, K., Tanaka, O., Esaki, S., and Imasaka, T., (1980). "Prediction of void fraction in subcooled and low quality boiling regions," *Bulletin of the JSME* 23:1475-1482.

Stephan, K and Abdelsalam, M., (1978). "Heat-transfer correlations for natural convection boiling", *Int. J. of Heat and Mass Transfer* 23: 73-87.

Sugrue, R, Buongiorno.J and McKrell.T. (2014). "An experimental study of bubble departure diameter in subcooled flow boiling including the effects of orientation angle, subcooling, mass flux, heat flux, and pressure", *Nucl. Engg. and Design* 279: 182–188.

Su G.H, Ronghua Chen, Wenxi Tian , Suizheng Qiu, Yuki Ishiwatari, Yoshiaki Oka (2014). “Numerical investigation on bubble dynamics during flow boiling using moving particle semi-implicit method”, *Nucl. Engg. and Design*, 240, 3830–3840.

Sussman, M. and Elbridge, G.P. (2000) "A coupled level set and volume-of-fluid method for computing 3D and axisymmetric incompressible two-phase flows." *J. of computational physics* 162: 301-337.

Tannaz, H. and Suresh V. G. (2009). “Effects of channel dimension, heat flux, and mass flux on flow boiling regimes in microchannels”, *Int. J. of Multiphase flow* 35: 349-362.

Thanh, H.T., Souad. H., Bernard, D., Sebastien, F. (2014).” Experimental investigation on the feasibility of heat pipe cooling for HEV/EV lithium-ion battery”. *Applied Thermal Engineering* 63: 551-558.

Thorncroft, G.E., Klausner.J.F. and Mei.R. (1998). “An experimental investigation of bubble growth and detachment in vertical up flow and down flow boiling”, *Int. J. of Heat Mass Transfer* 41: 3857–3871.

Tomasz, W. and Tadeusz, K. (2008).” Comparison of CICSAM and HRIC high-resolution schemes for interface capturing”, *J. of Theoretical and Applied Mechanics* 46 (2): 325-345

Tomio O., Rouhollah A. and Tatsuya Ueno. (2012) Bubble dynamics at boiling incipience in subcooled upward flow boiling, *Int. J. Heat Mass Transfer* 55:488-497.

(2012) 488–497.Tomasz, W. and Tadeusz, K. (2008). “Comparison of CICSAM and HRIC high-resolution schemes for interfaces capturing”, *J. of Theoretical and Applied Mechanics* 46: 325-345.

Tong, L.S and Tang, Y.S (1997). Text book on: “Boiling Heat Transfer and Two Phase flow”, Taylor and Francis, 2: 248-265.

Ubbink, O. and Issa, R.I. (1999). “A Method for Capturing Sharp Fluid Interfaces on Arbitrary Meshes”, *J. of Comp. Physics*, 153: 26–50.

Unal, H. C., (1975). “Determination of the initial point of net vapor generation in flow boiling systems”, *Int. J. of Heat and Mass Transfer* 18:1095-1099.

Vijay K. D, Hari, Abharjith and Ding, L. (2007). “Bubble Dynamics and Heat Transfer during Pool and Flow Boiling”, *Heat Transfer Engineering*, Taylor and Francis, 28: 608–624.

Vijay K. D., Wu, J. and Jianliang, Q. (2007). "Numerical simulation of subcooled nucleate boiling by coupling level-set method with moving-mesh method." *Numerical Heat Transfer, Part B: Fundamentals* 51: 535-563.

Wang, C., Wang, H. and Gao, P. (2014). “Experimental study of boiling incipience in vertical narrow rectangular channel”, *Ann Nucl Energy* 66:152–160.

Weiwei, C. and Fang, X. (2014). “A Note on the Chen Correlation of Saturated Flow Boiling Heat Transfer”, *J. of Refrigeration* 48:100–104.

Welch, Samuel W.J., and John, W. (2000). "A volume of fluid based method for fluid flows with phase change." *J. of comp. physics* 160: 662-682.

Wolverine Tube INC (2003). “Boiling Heat Transfer on Extended Surface”, Engg. data handbook 3: Chapter 9.1-9.38.

Yeoh, G.H and Tu, J.Y. (2005). “A unified model considering force balances for departing vapour bubbles and population balance in subcooled boiling flow”, *Nucl. Engg. and Design* 235: 1251–1265.

Yuan, W., Khellil, S. and Souad, H. (2012), “Flow boiling in high-aspect ratio mini- and micro-channels with FC-72 and ethanol”, *Exp. Thermal and Fluid Science* 36: 93–106.

Yan, F. F. (2013). Thesis on: “Experimental Investigations of Flow Boiling Heat Transfer and Flow Instability in a Horizontal Micro tube with an Inlet Orifice”, Concordia University, Montreal, Quebec, Canada.

Yovanovich, M.M. and Muzychka, Y.S. (2004). “Laminar Forced Convection Heat Transfer in the Combined Entry Region of Non-Circular Ducts”, *J. of Heat Transfer* 124: 54-61.

Zeitoun, O and Shoukri, M. (1996). “Bubble behavior and mean diameter in subcooled flow boiling”, *J. of Heat Transfer* ASME 118: 110–116.

Zeng, L.Z., Klausner, J.F., Bernhard, D.M., Mei, R. (1993). “A unified model for the prediction of bubble detachment diameters in boiling systems. II. Flow boiling”, *Int. J. of Heat and Mass Transfer* 36: 2271–2279.

Zuber, N. and Forster, H.K., (1954). “Growth of a vapor bubble in a superheated liquid”, *J. of Applied Physics* 5: 474-479.

Zuber, N., and Ishii, M., (1979). “Drag coefficient and relative velocity in bubbly, droplet and particulate flows”, *AIChE Journal* 25: 843–855.

http://www.lytron.com/Cold-Plates

APPENDIX A

UNCERTAINTY

Table A.1: Uncertainty for mass flow measurement

Mass flow rate (kg/s)	Uncertainty in mass flow (%)	Uncertainty in mass flux (%)
0.0077	2.21	0.272
0.0113	2.21	0.402
0.0152	2.3	0.517
0.0192	2.4	0.627
0.0228	2.32	0.773

Table A.2: Uncertainty values for heat flux and heat transfer coefficient of water at inlet temperature=303 K.

Heat flux(W/m^2)	Heat transfer coefficient (kW/m^2-K)	Uncertainty in heat flux (%)	Uncertainty in heat transfer coefficient (%)
21780	1.452	3.18	2.29
21780	1.676	3.66	1.98
21780	1.876	4.10	1.77
21780	2.08	4.54	1.6
21780	2.223	4.85	1.49
28750	1.632	3.57	3.81
28750	1.908	4.18	3.26
28780	2.107	4.61	2.95
28750	2.365	5.18	2.63
28750	2.587	5.66	2.40
35110	1.816	3.98	5.52
35110	2.215	4.85	4.52
35110	2.413	5.29	4.15
35110	2.689	5.89	3.73
35110	2.845	6.23	3.52
48490	2.112	4.63	6.55
48490	2.446	5.36	5.66

Heat flux(W/m^2)	Heat transfer coefficient (kW/m^2-K)	Uncertainty in heat flux (%)	Uncertainty in heat transfer coefficient (%)
48490	2.754	6.04	5.03
48490	2.964	6.5	4.67
48490	3.181	6.97	4.35
61330	2.445	5.36	7.16
61330	2.632	5.77	6.65
61330	3.079	6.75	5.69
61330	3.276	7.18	5.34
61330	3.433	7.53	5.1
78300	2.828	6.2	8.11
78300	3.041	6.67	7.54
78300	3.499	7.67	6.56
78300	3.563	7.82	6.44
78300	3.834	8.41	5.98
90400	3.567	7.82	7.24
90400	3.817	8.37	6.76
90400	4.113	9.03	6.28
90400	4.478	9.82	5.77
90400	4.602	10.09	5.61
100500	3.142	6.91	9.12
100500	3.421	7.52	8.37
100500	3.785	8.32	7.57
100500	4.082	8.97	7.01
100500	4.386	9.64	6.53
109340	4.17	9.15	7.49
109340	4.365	9.58	7.16
109340	4.652	10.21	6.72
109340	4.934	10.83	6.33
109340	5.189	11.39	6.02
120130	4.87	10.66	7.09
120130	5.124	11.21	6.74
120130	5.378	11.77	6.42
120130	5.673	12.41	6.08
120130	5.821	12.74	5.93
133470	5.43	11.92	7.02

Heat flux(W/m^2)	Heat transfer coefficient (kW/m^2-K)	Uncertainty in heat flux (%)	Uncertainty in heat transfer coefficient (%)
133470	5.632	12.36	6.77
133470	5.892	12.93	6.47
133470	6.094	13.37	6.26
133470	6.235	13.68	6.12

APPENDIX B

FORCED CONVECTION AND SUBCOOLED FLOW BOILING

B.1. Variation of heat flux and heat transfer coefficient with wall super heat for water-ethanol mixture

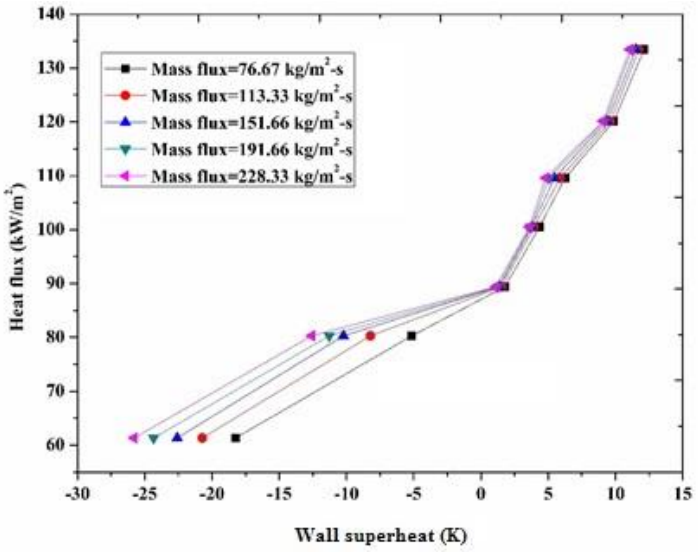

Figure B.1: Variation of heat flux with wall superheat for water at inlet temperature=313 K.

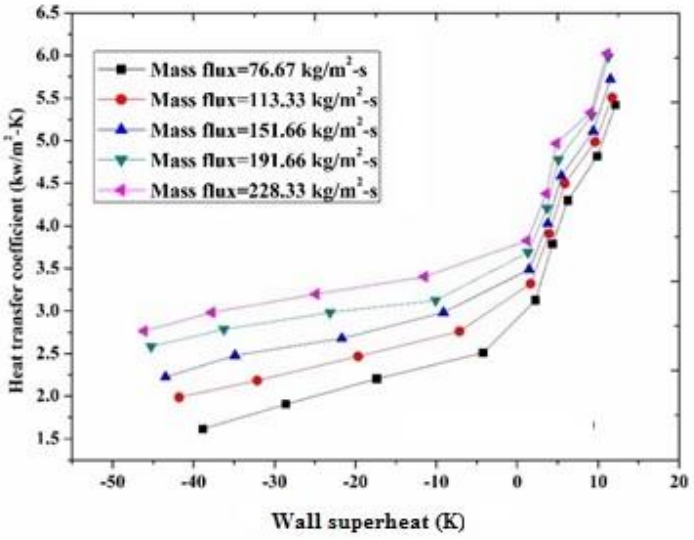

Figure B.2: Variation of heat transfer coefficient with wall superheat for water at inlet temperature=313 K.

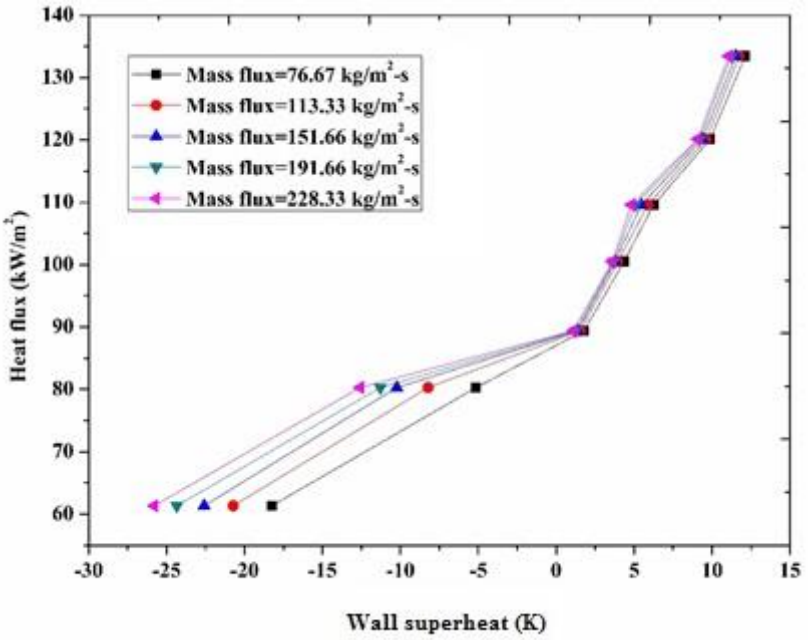

Figure B.3: Variation of heat flux with wall superheat for water at inlet temperature=323 K.

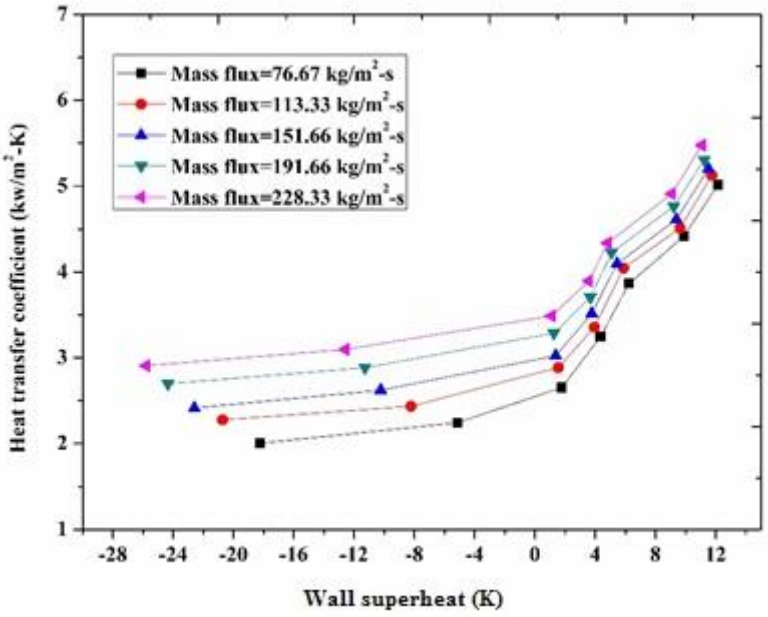

Figure B.4: Variation of heat transfer coefficient with wall super heat for water at inlet temperature=323 K.

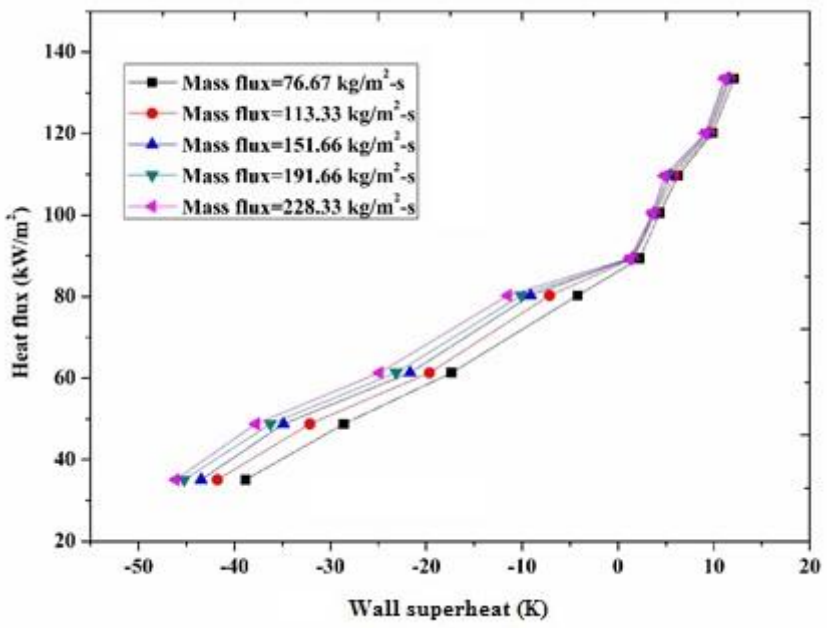

Figure B.5: Variation of heat flux with wall superheat for water-ethanol mixture of ethanol volume fraction 25% at inlet temperature=313 K.

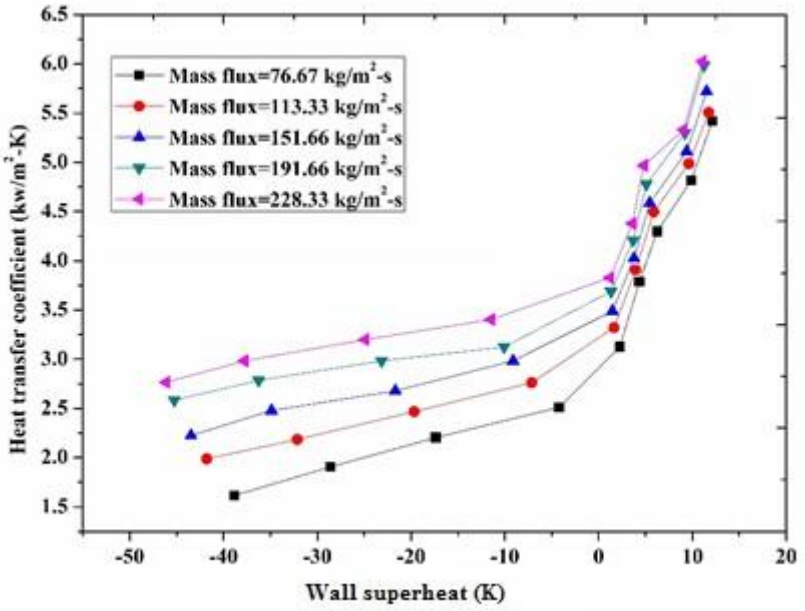

Figure B.6: Variation of heat transfer coefficient with wall super heat for water-ethanol mixture of ethanol volume fraction 25% at inlet temperature=313 K.

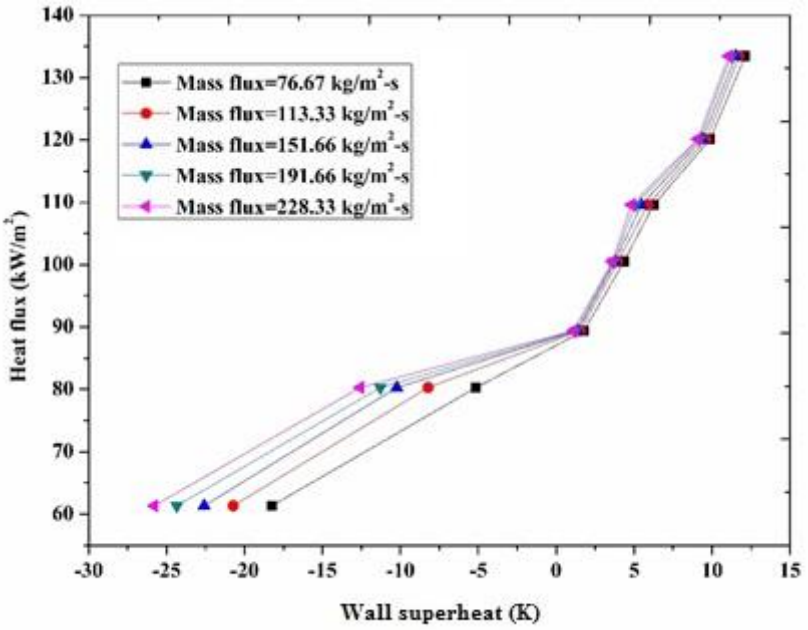

Figure B.7: Variation of heat flux with wall superheat for water-ethanol mixture of ethanol volume fraction 25% at inlet temperature=323 K.

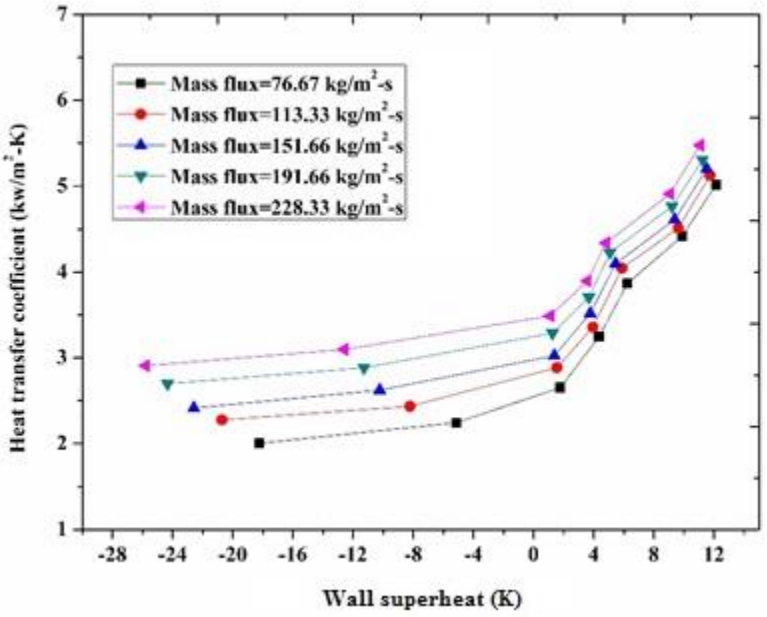

Figure B.8: Variation of heat transfer coefficient with wall super heat for water-ethanol mixture of ethanol volume fraction 25% at inlet temperature=323 K.

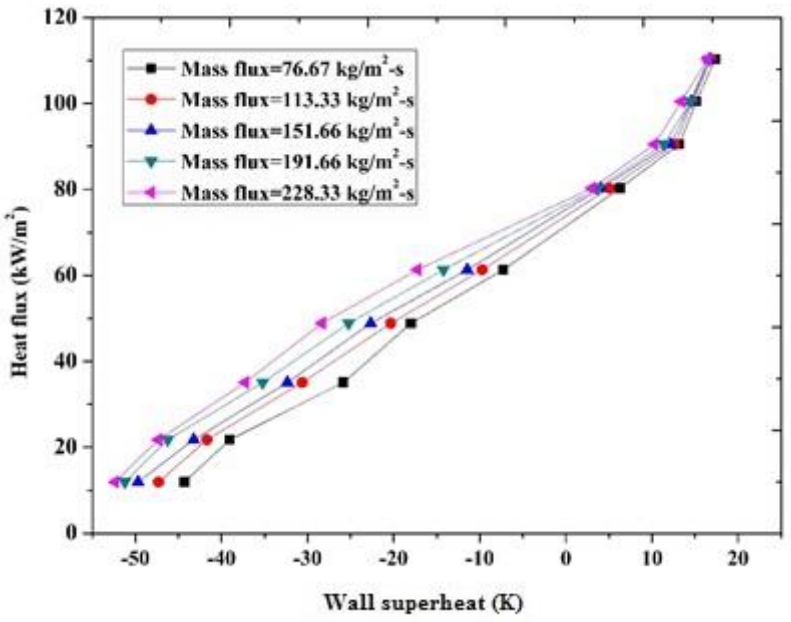

Figure B.9: Variation of heat flux with wall superheat for water-ethanol mixture of ethanol volume fraction 50% at inlet temperature=303 K.

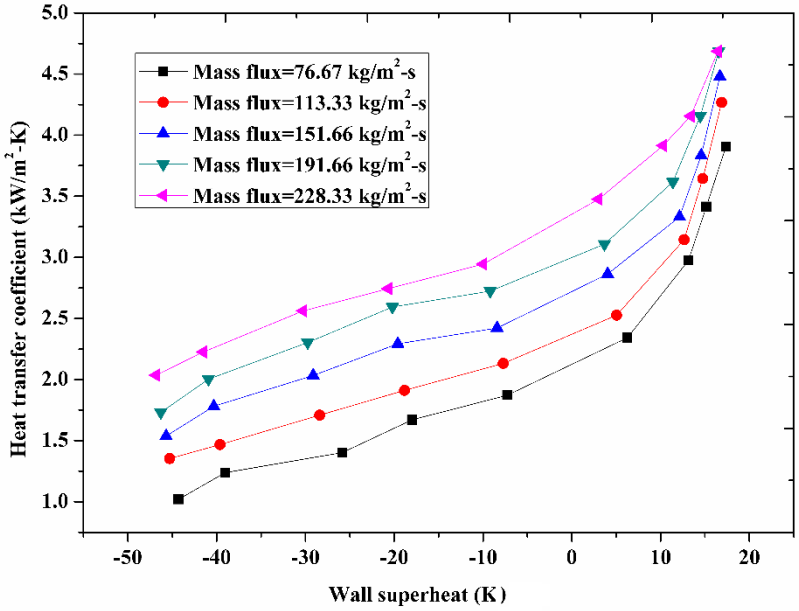

Figure B.10: Variation of heat transfer coefficient with wall super heat for water-ethanol mixture of ethanol volume fraction 50% at inlet temperature=303 K.

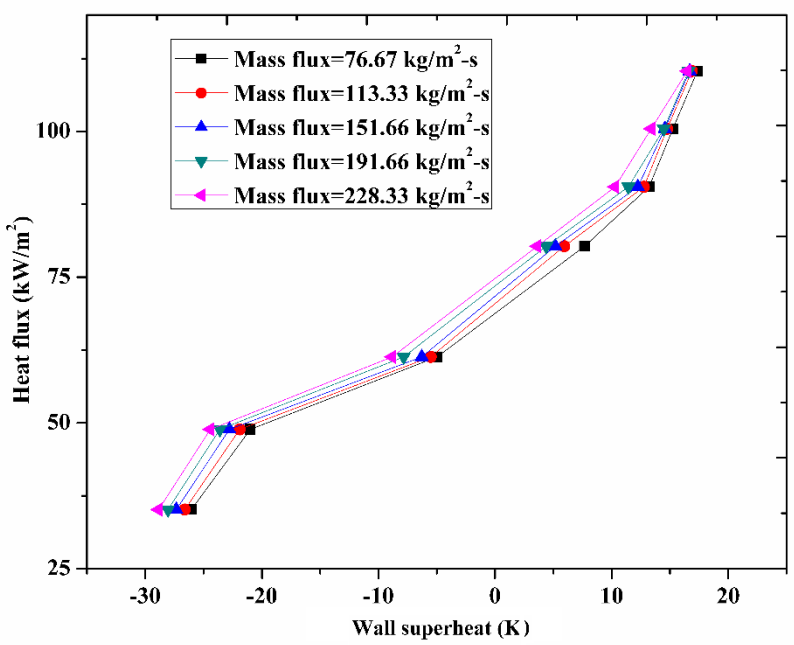

Figure B.11: Variation of heat flux with wall superheat for water-ethanol mixture of ethanol volume fraction 50% at inlet temperature=313 K.

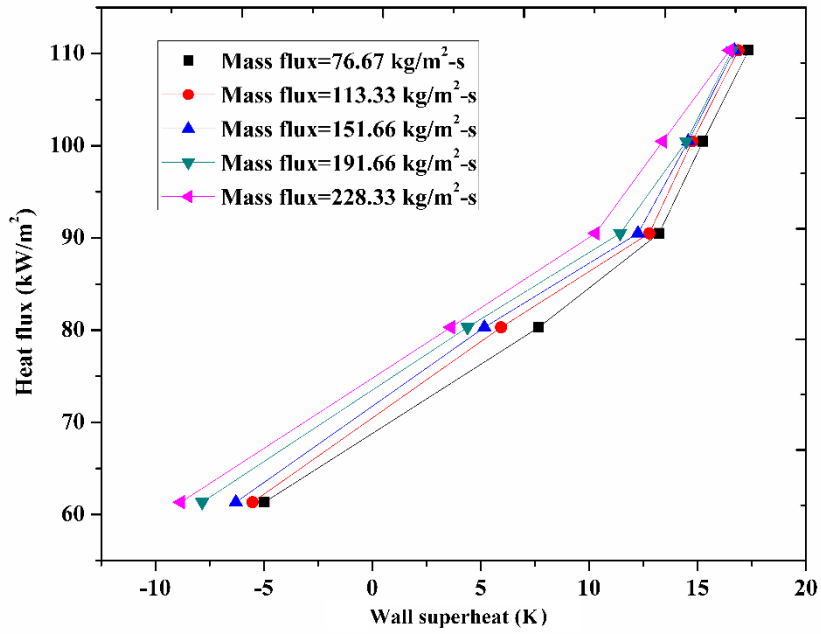

Figure B.12: Variation of heat transfer coefficient with wall super heat for water-ethanol mixture of ethanol volume fraction 50% at inlet temperature=313 K.

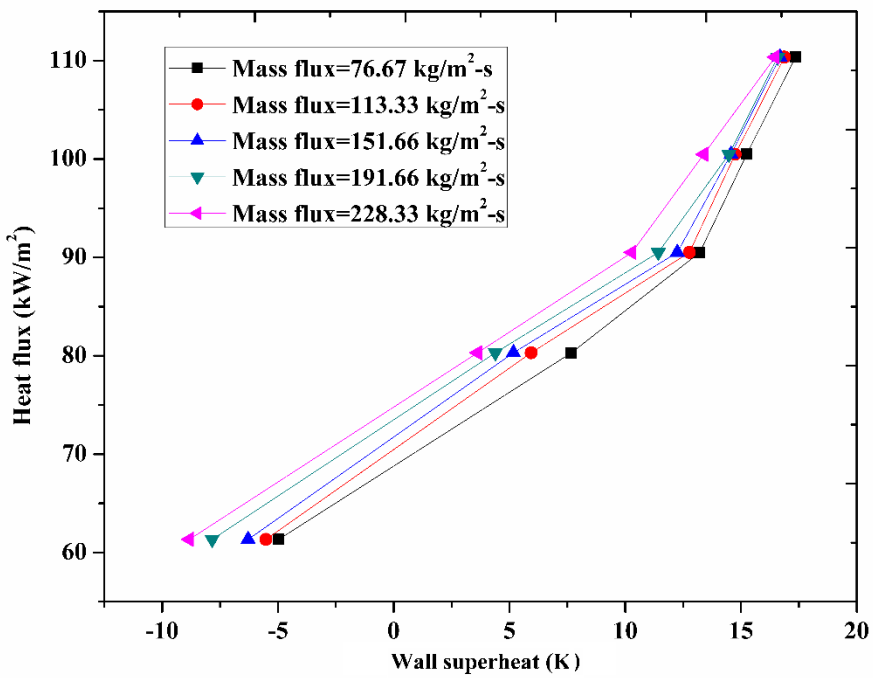

Figure B.13: Variation of heat flux with wall superheat for water-ethanol mixture of ethanol volume fraction 50% at inlet temperature=323 K.

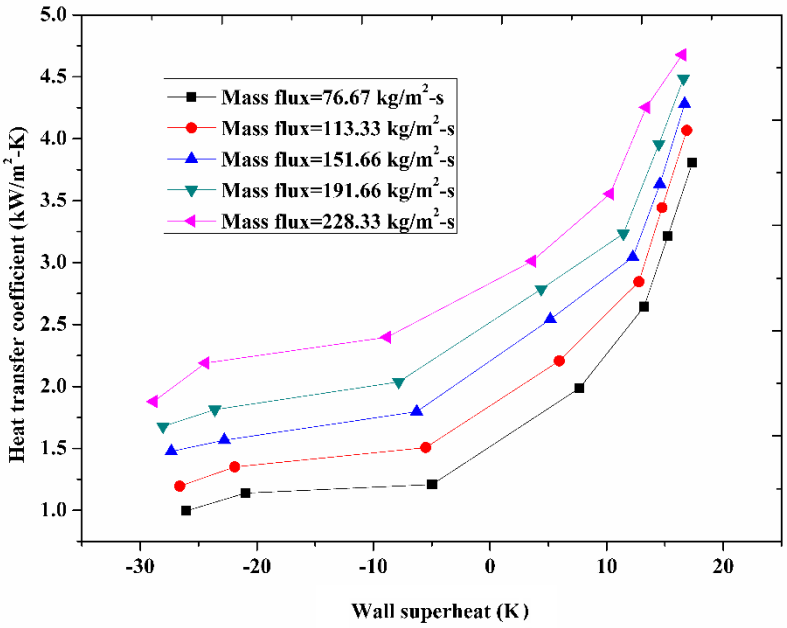

Figure B.14: Variation of heat transfer coefficient with wall super heat for water-ethanol mixture of ethanol volume fraction 50% at inlet temperature=323 K.

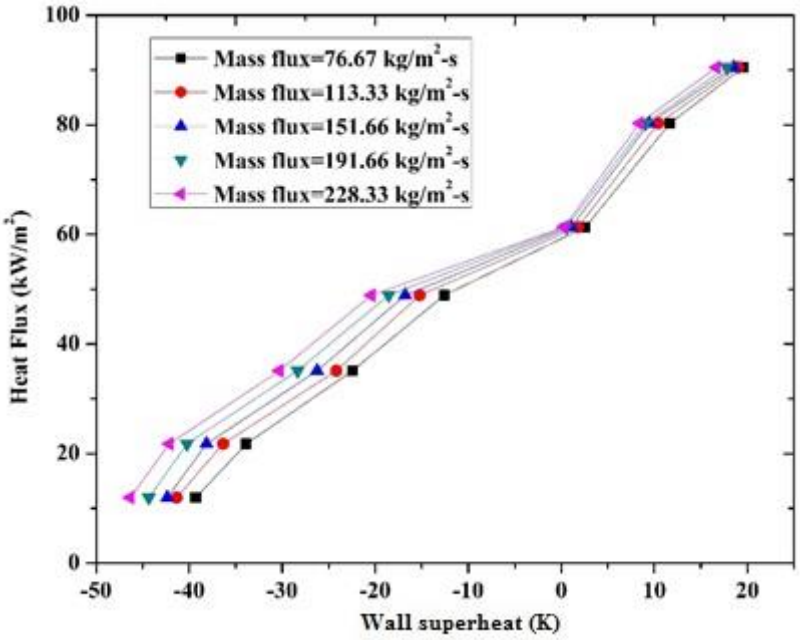

Figure B.15: Variation of heat flux with wall superheat for water-ethanol mixture of ethanol volume fraction 75% at inlet temperature=303 K.

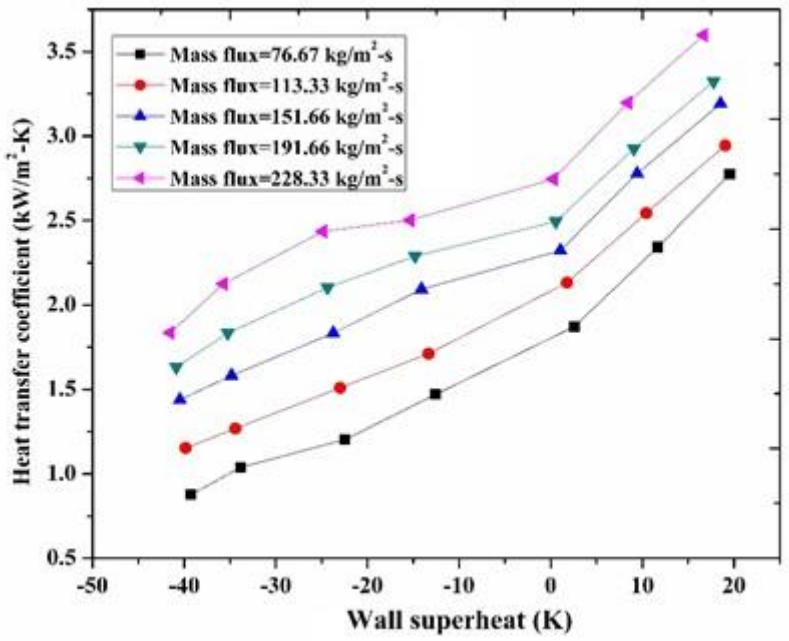

Figure B.16: Variation of heat transfer coefficient with wall super heat for water-ethanol mixture of ethanol volume fraction 75% at inlet temperature=303 K.

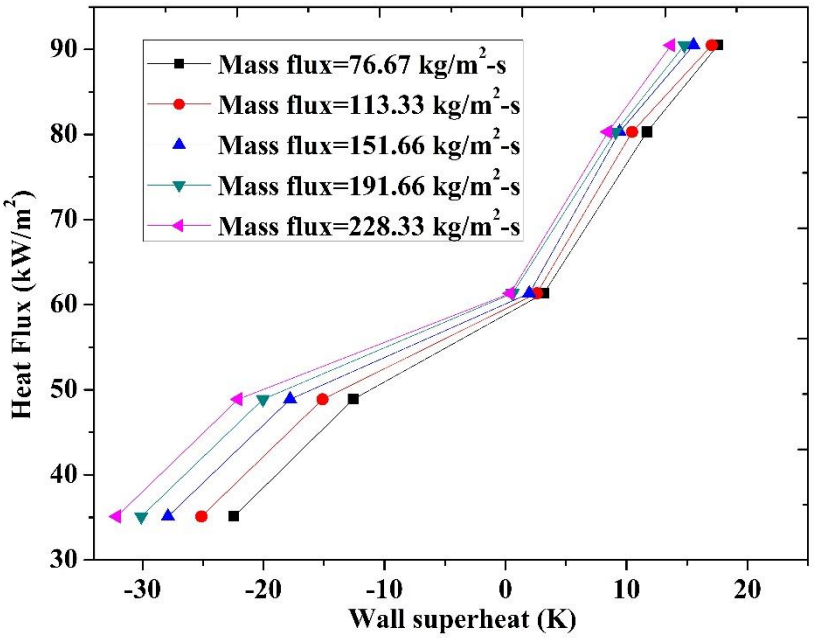

Figure B.17: Variation of heat flux with wall superheat for water-ethanol mixture of ethanol volume fraction 75% at inlet temperature=313 K.

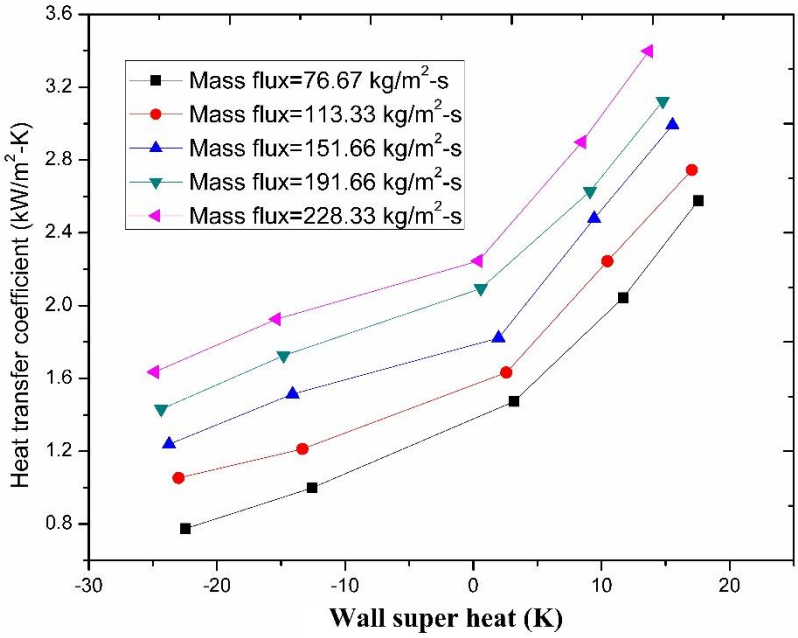

Figure B.18: Variation of heat transfer coefficient with wall super heat for water-ethanol mixture of ethanol fraction 75% at inlet temperature=313 K.

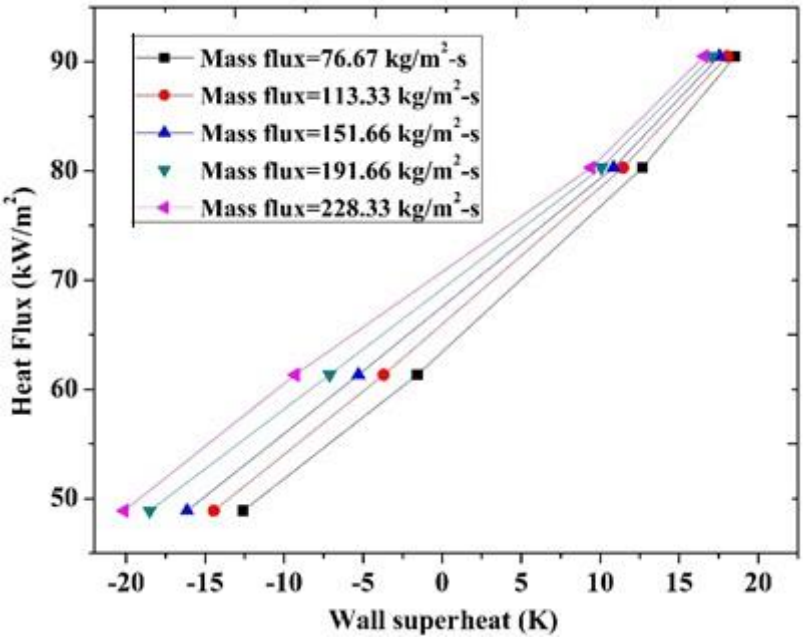

Figure B.19: Variation of heat flux with wall superheat for water-ethanol mixture of ethanol volume fraction 75% at inlet temperature=323 K.

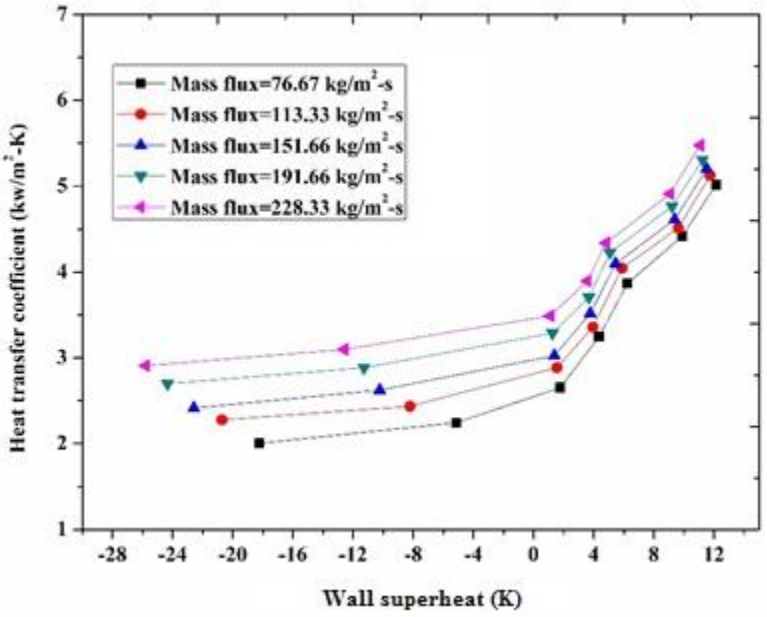

Figure B.20: Variation of heat transfer coefficient with wall super heat for water-ethanol ethanol volume fraction 75% at inlet temperature=323 K.

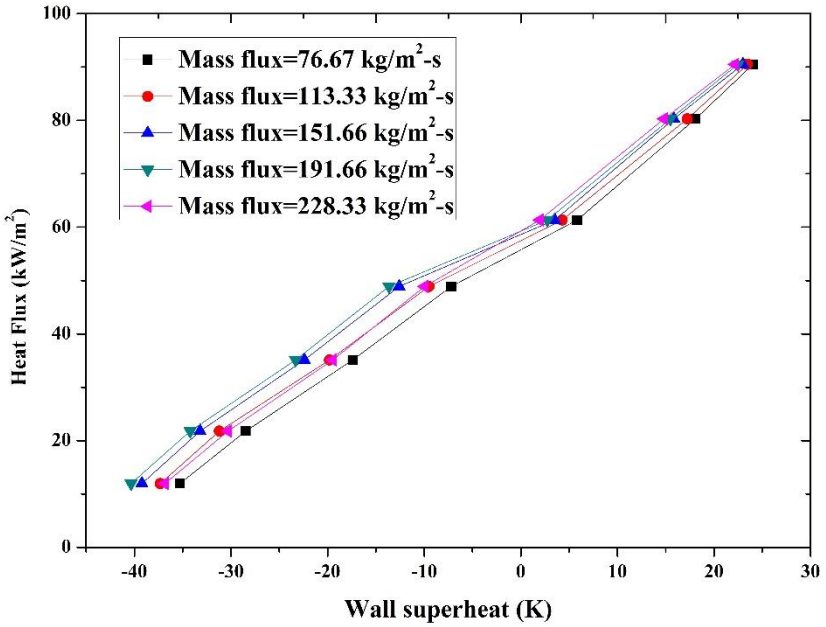

Figure B.21: Variation of heat flux with wall superheat for ethanol at inlet temperature=303 K.

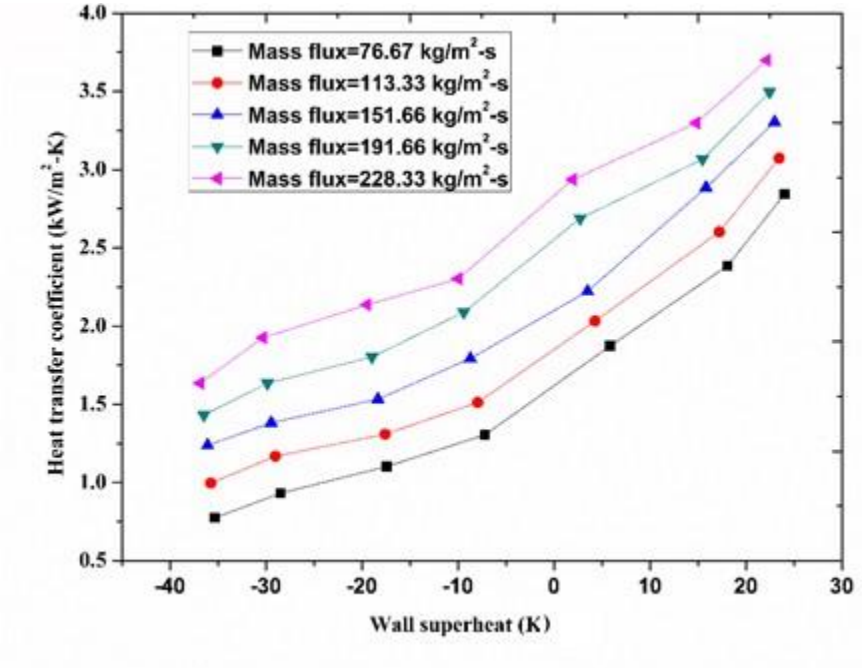

Figure B.22: Variation of heat transfer coefficient with wall super heat for ethanol at inlet temperature=303 K.

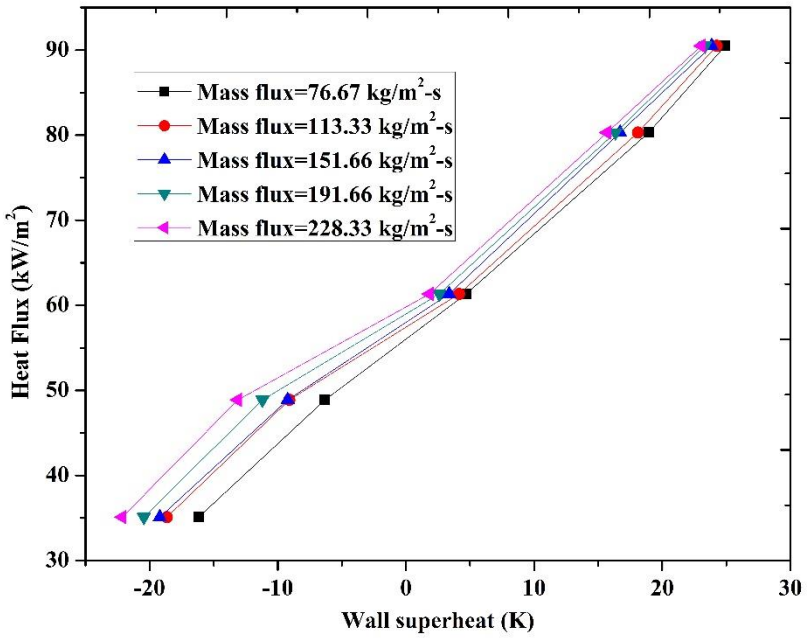

Figure B.23: Variation of heat flux with wall superheat for ethanol at inlet temperature=313 K.

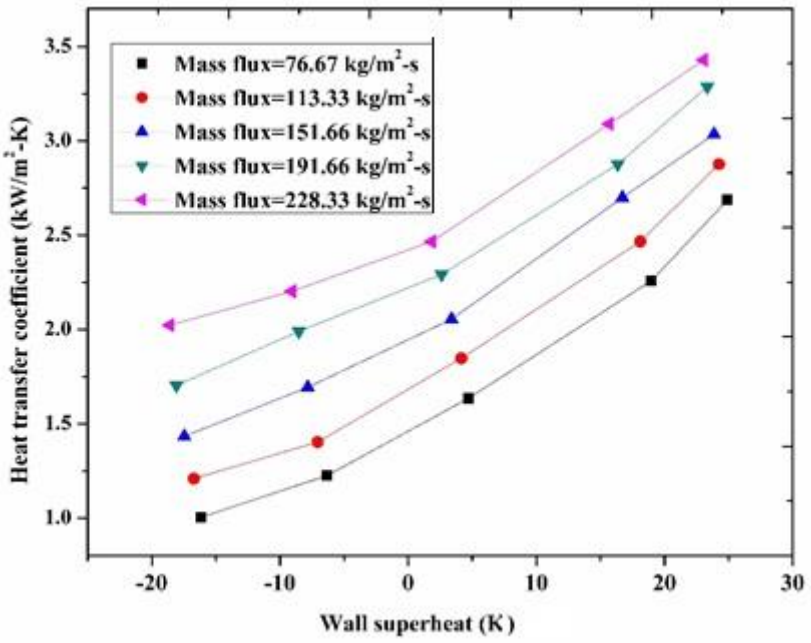

Figure B.24: Variation of heat transfer coefficient with wall super heat for ethanol at inlet temperature=313 K.

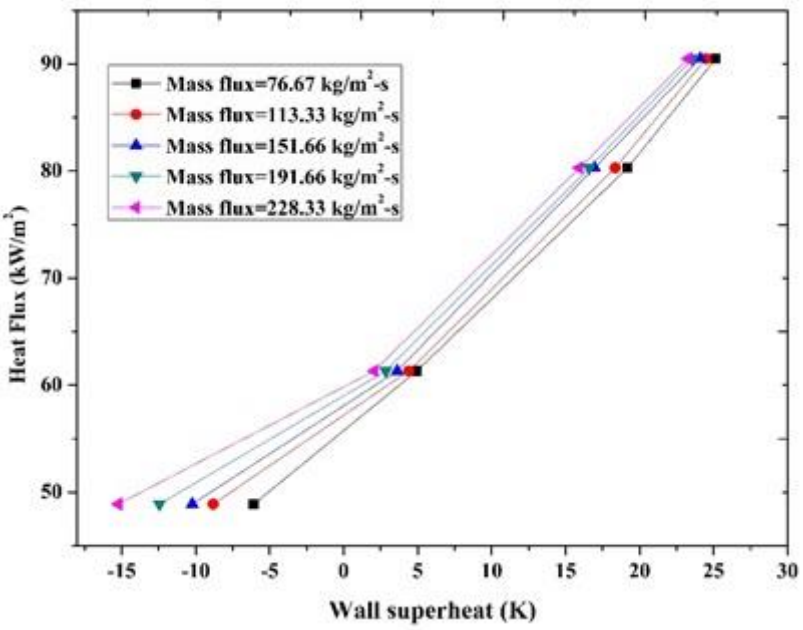

Figure B.25: Variation of heat flux with wall superheat for ethanol at inlet temperature=323 K.

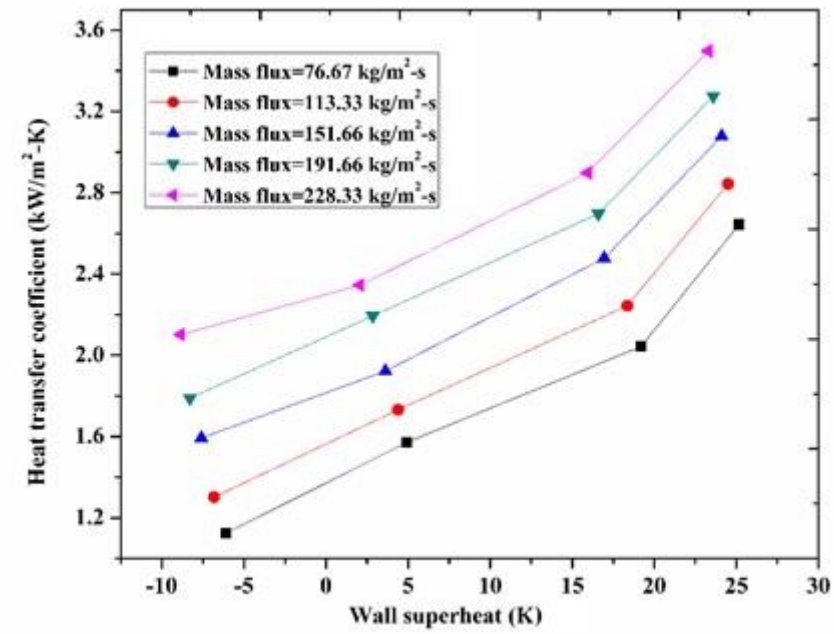

Figure B.26: Variation of heat transfer coefficient with wall super heat for ethanol at inlet temperature=323 K.

B.2. Effect of inlet temperature on forced convective heat transfer coefficient of water-ethanol mixture

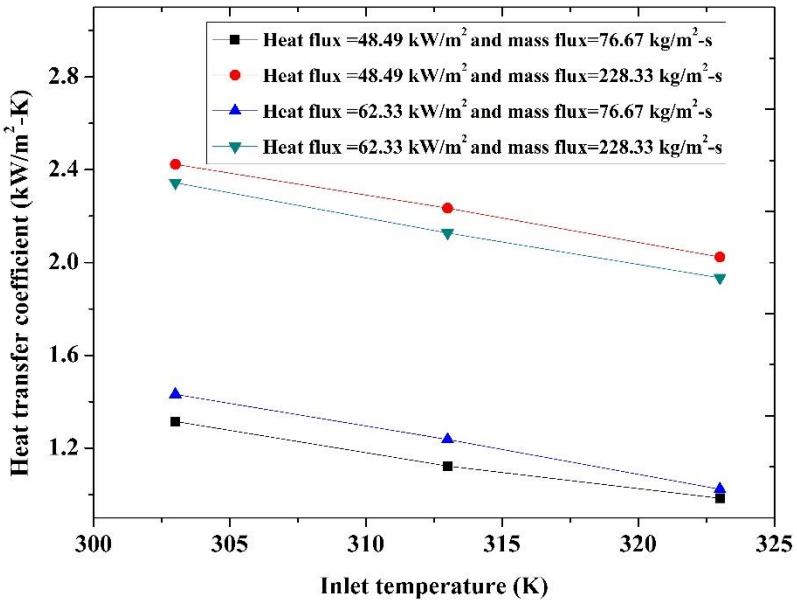

Figure B.27: Variation of forced convective heat transfer coefficient with inlet temperature for water-ethanol mixture of ethanol volume fraction 50%.

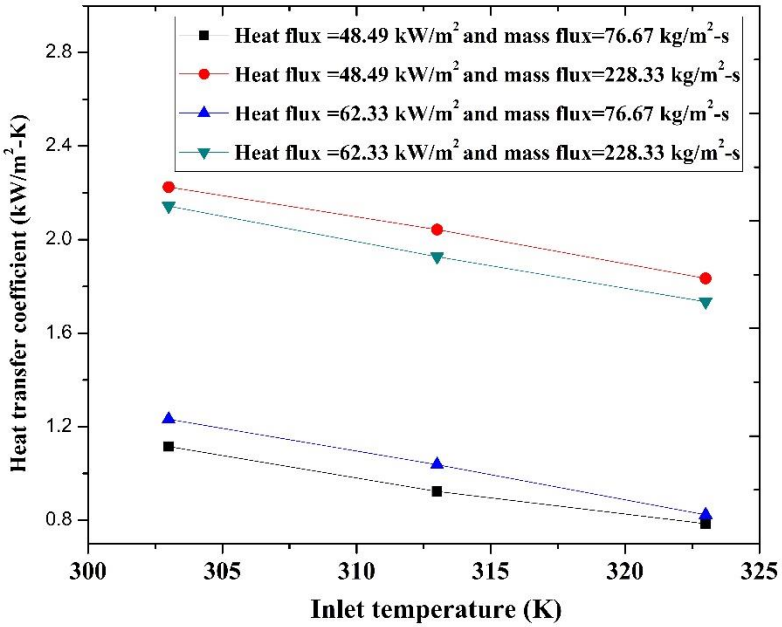

Figure B.28: Variation of forced convective heat transfer coefficient with inlet temperature for water-ethanol mixture of ethanol volume fraction 75%.

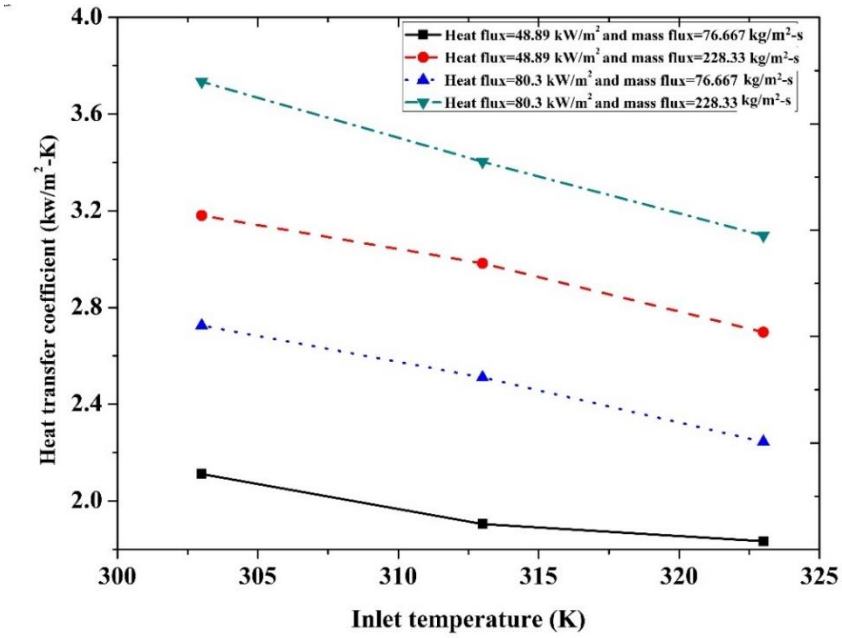

Figure B.29: Variation of forced convective heat transfer coefficient with inlet temperature for ethanol.

B.3. Effect of inlet temperature on subcooled flow boiling heat transfer coefficient

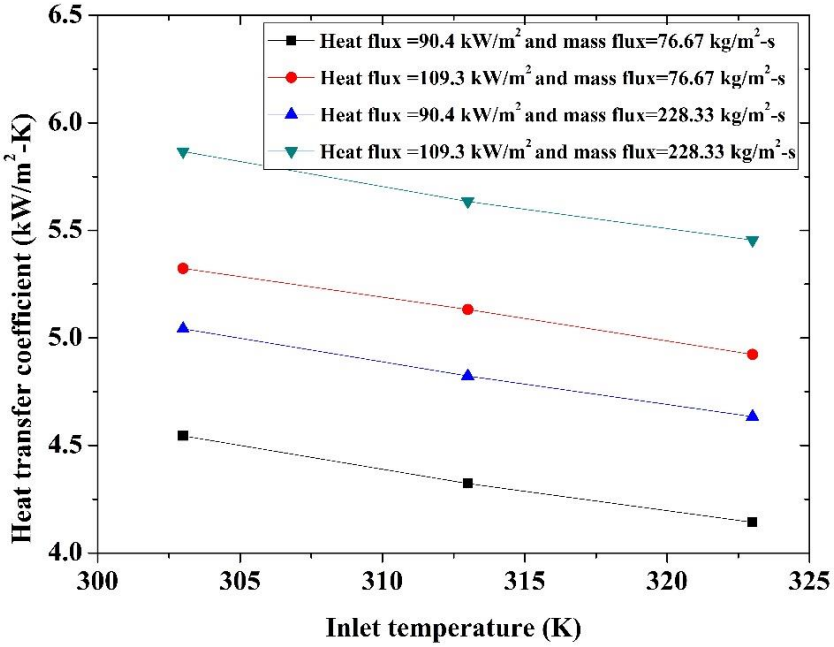

Figure B.30: Variation of subcooled flow boiling heat transfer coefficient with inlet temperature for water-ethanol mixture of ethanol volume fraction 50%.

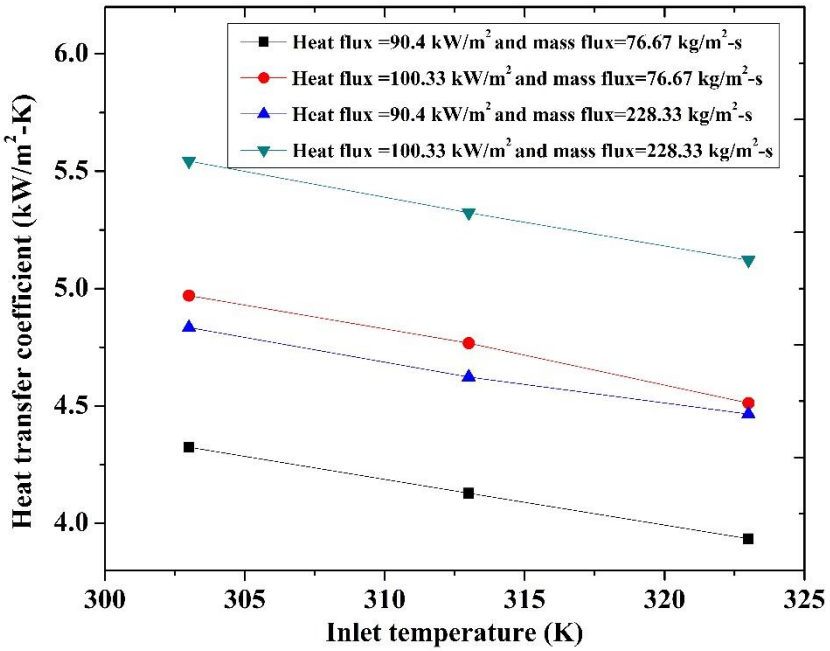

Figure B.31: Variation of subcooled flow boiling heat transfer coefficient with inlet temperature for water-ethanol mixture of ethanol volume fraction 75%.

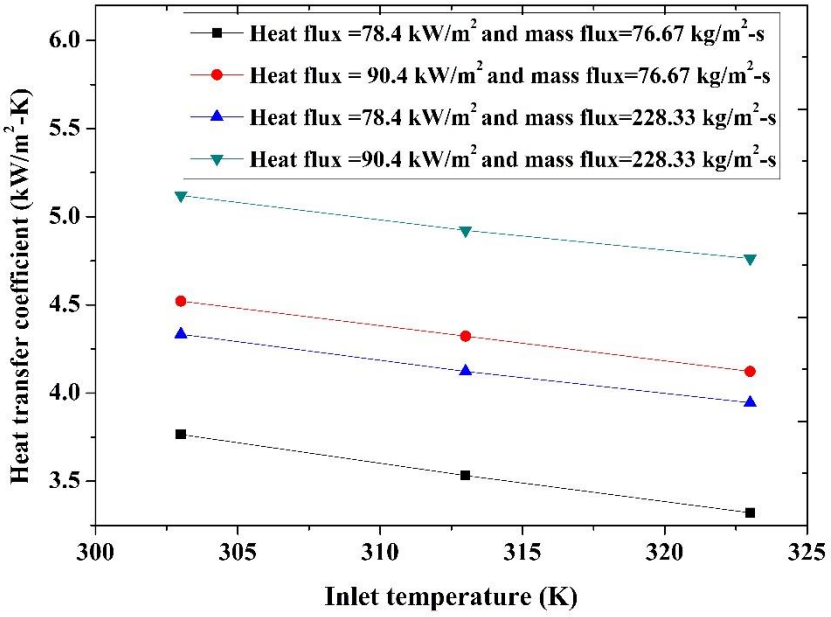

Figure B.32: Variation of subcooled flow boiling heat transfer coefficient with inlet temperature for ethanol.

APPENDIX C

MATHEMATICAL MODELLING CODE

C.1. MatLab r2013a code developed to estimate the forced convective heat transfer coefficient of water at heat flux=21.78 kW/m^2 and mass flux=76.67 kg/m^2-s

Pressure correction method:

```
Dt=0.01;
l=0.15;
b=0.01;
Nx=15;
Ny=4;
Dx=l/(Nx-1);
Dy=b/(2*Ny-1);
rho=1680;
mhu=0.00064;
Re=500;
dh=(4*l*b)/(2*(l+b));
ui=(Re*mhu)/(dh*rho);
u=zeros(1,Ny);
st=-(ui/((Ny)-1));
for j=1:Ny
    u(j)=st+(ui/((Ny)-1));
    st=u(j);
end
u
i=1;j=1;A=0.6;
delps=zeros(Nx,1);
delpd=zeros(Nx,1);
n=0;
delp1=zeros(Nx,1);
delp2=zeros(Nx,1);
uu(1,j)=ui;
for i=1:(Nx-1)
    delp1(i+1,j)=0;
    delp2(i+1,j)=0;
    while abs(delp2(1+1,j)-delp1(i+1,j))>0.01
        delp1(i+1,j)=delp2(i+1,j);
        delps(i+1,j)=abs(delp2(i+1,j));

uu(i+1,j)=(Dt/(rho*Dx))*delps(1+1,j)+(((mhu*Dt)/(rho*Dy^2))*(u(j)-
2*u(j+1)+u(j+2)))+u(j+1);
        delpd(i+1,j)=((-Dx*rho)/Dt)*(uu(i+1,j)-uu(i,j))-delpd(i,j);

uu1(i+1,j)=(Dt/(rho*Dx))*delpd(1+1,j)+(((mhu*Dt)/(rho*Dy^2))*(u(j)-
2*u(j+1)+u(j+2)))+u(j+1);
         delp2=delps(i+1,j)+A*delpd(i+1,j);
         uu(i+1,j)=uu(i+1,j)+A*uu1(i+1,j);
    end
    uu
    delps
```

Lax Wendroff Explicit method

```
Dt=0.01;
    l=0.15;
    b=0.01;
    Nx=12;
    Ny=8;% no of grids in half section
    Dx=l/(Nx-1); Dy=b/(2*Ny-1);%lets take a grid of 6/15 for l=15 and
b=2
    % lets take the temp as 20 degrees and so the properties of water
at that temp is
    d=1003;%density in kg/m^3
    m=8.55*(10^-4)%viscosity in pascals.second
    Re=1000;
    De=(4*l*b)/(2*(l+b));% equi dia = 4*A/P
    Ui=(Re*m)/(d*De)
        u=zeros(1,Ny);
        k=-(Ui/((Ny)-1));
        for j=1:Ny
            u(j) = k+(Ui/((Ny)-1));
            k=u(j);
        end
        u
        i=1;j=1;A=0.6;
        %say (p(i+2,j+2)-p(i+4,j+2))=p=0.5;
        p=zeros(Nx,1); P=zeros(Nx,1);n=0;
        p1=zeros(Nx,1);p2=zeros(Nx,1);
        uu(1,j)=Ui;
 for i=1:(Nx-1)%actually we do it for uu(i+0.5,j+1) p(i+1,j+1)
     p1(i+1,j)=-1;p2(i+1,j)=0;
                while abs(p1(i+1,j)-p2(i+1,j))>0.01
                    p2(i+1,j)=p1(i+1,j);
                    p(i+1,j)=abs(p1(i+1,j));

uu(i+1,j)=((Dt/(d*Dx))*p(i+1,j))+(((m*Dt)/(d*Dy^2))*(u(j)-
2*u(j+1)+u(j+2)))+u(j+1);
                P(i+1,j)= ((-Dx*d)/Dt)*(uu(i+1,j)-uu(i,j))-P(i,j);

uu1(i+1,j)=((Dt/(d*Dx))*P(i+1,j))+(((m*Dt)/(d*Dy^2))*(u(j)-
2*u(j+1)+u(j+2)))+u(j+1);
                p1(i+1,j)=p(i+1,j)+A*P(i+1,j);
                uu(i+1,j)=uu(i+1,j)+A*uu1(i+1,j);
                end
 end
  uu
  p1
```

C.2. Matlab r2013a code developed to determine the subcooled flow boiling heat transfer coefficient of water at heat flux=90.4 kW/m^2 and mass flux=76.667 kg/m^2-s.

```
delt = input('enter the delt');
delx = input('enter the delx');
dely = input('enter the dely');
uin = input('enter the uin');
cin = input('enter the cin');

% delt = 0.1;
% delx = 0.1;
% uin = 0.0076;
% cin = 0.5;
% dely = 0.125;

delpi = 0.001;%for pressure-correction method
%getting inputs
%for matrix of the form AX=B
N = input('enter the order for the matrix - I');
M = input('enter the order for the matrix - J');
theta = input('enter the contact angle theta');
%disp('enter the initial values for alpha, alpha10,
alpaha20,....alphan0');
alpha = ones(1,N);

fprintf(1,'Enter the initial values for alpha, alpha1i,
alpaha2i,....alphani...')
disp('\n');
for i=1:N
    s = sprintf('enter the alpha%di\n',i);
    alpha(i) = input(s);
end

% alpha = [0 0 0 0 0 0 0 0 0 0 0.5 1 0 0.5 1 0 0 0.5 1 0.5 0 0 0 0.5 1
0.5 0 0.5 1 0.5 1 0];


U=TDMAmain(delt,delx,uin,alpha,N);

disp('Solved using TDMA method...');
disp('alpha1 alpha2 alpha3....');
disp(U);
%%
Ui = alpha;
p1 = (cos(2*(theta*0.0174533))+1)/2;
Bf = min(p1,1);
cont=0;
for i=1:N
    if(U(i)>=0 && U(i)<1)
        cont = cont+1;
```

```
    end
end


if(cont==N)
    for i=1:N
            df = abs(U(i)-Ui(i));
            count=0;
            while(df>0.0001 && count<20)
                Ui = U;
                U=TDMAmain(delt,delx,uin,Ui,N);
                df = abs(U(i)-Ui(i));
                count=count+1;
            end
    end
end
% disp('----------------After initial itration-------------');
% disp(U);
%%
%corrector-predictor step----
%only for odd values
% for i=1:2:N
%     delalpha(i) = ((alpha(i)+U(i))/2) - ((alpha(i+2)+U(i+2))/2);
% end
alphat = alpha;
Ut = U;
alphat(N+1)=0;
alphat(N+2)=0;
Ut(N+1)=0;
Ut(N+2)=0;
Bfd=0;


for i=1:2:N
    delalpha = ((alphat(i)+Ut(i))/2) - ((alphat(i+2)+Ut(i+2))/2);
    count3=0;
    while((Ut(i)<0 || Ut(i)>1) && count3<20)

        if(Ut(i)<0)
            EN = max(-Ut(i),0);
              if(delalpha>EN)
                  P2 = (EN*(2+cin-2*cin*Bf))/(2*cin*(delalpha-EN));
                  Bfd = min(P2,Bf);
              else
                  Bfd=0;
              end
              Bfstar = abs(Bf-Bfd);
              alpha2star = (1-Bfstar)*((Ut(i)+alphat(i)+EN)/2)+ Bfstar*
((Ut(i+2)+alphat(i+2)+EN)/2);
              alphafstar = alpha2star-(EN/cin);
        end
        %-----------------------------------------------------------------
--------
```

```
        if(Ut(i)>1)
            EP = max(Ut(i)-1,0);
            if(delalpha>EP)
                  P3 = (EP*(2+cin-2*cin*Bf))/(2*cin*(delalpha-EP));
                  Bfd = min(P3,Bf);
            else
                  Bfd=0;
            end
            Bfstar = abs(Bf-Bfd);
            alpha2star = (1-Bfstar)*((Ut(i)+alphat(i)+EP)/2)+ Bfstar*
((Ut(i+2)+alphat(i+2)+EP)/2);
            alphafstar = alpha2star-(EP/cin);
        end
        %-----------------------------------------------------------------
--------

        Ut(i) = (2*alphafstar-alphat(i)+Bf*alphat(i)-Bf*alphat(i+2)-
Bf*Ut(i+2))/(Bf);
        count3=count3+1;

    end



end
U = Ut(1:N);
% disp('----------------before even---------------------');
% disp(U);
%%
%CP step for even numbers

for i=2:2:N
    if(Ut(i)<0 || Ut(i)>1)
        %normalization step
        dalpha = abs(Ut(i+1)-Ut(i+2))/ (abs(Ut(i-1)-Ut(i+2)));
        if(dalpha<=1 && dalpha>=0)
            alphacbc = min((dalpha/cin),1);
            P10 = (8*cin*dalpha+(1-cin)*(6*dalpha+3))/3;
            alphauq = min(P10,alphacbc);
        end
        if(dalpha<0 || dalpha>1)
            alphacbc = dalpha;
            alphauq = dalpha;
        end
        Ut(i) = (1-Bf)*alphacbc+Bf*alphauq;
    end
end

U = Ut(1:N);
% disp('----------------pre-final itration--------------------');
% disp(U);
%%
```

```
  %final looping
if(U(i)>0 && U(i)<1)
    df = abs(U(i)-Ui(i));
    count=0;
    while(df>0.0001 && count<20)
        Ui = U;
        U=TDMAmain(delt,delx,uin,Ui,N);
        df = abs(U(i)-Ui(i));
        count=count+1;
    end
end
disp('-----------------------final alpha-------------------------');
disp(U);

%wrting the alpha values
fn = 'alpha.txt';
fid = fopen(fn,'w');
for i=1:length(U)
  fprintf(fid, '%3.3f\n', U(i));
end

fclose(fid);
%-------------------------------------------------------------
%%
%-----------------stage-2-----------------------------------
disp('******************Stage-2************************');
disp('--------------------Pressure correction method------------------
');

%getting inputs
%material constants
kw = input('enter the thermal conductivity of fluid');
kwv = input('enter the thermal conductivity of vapour');

cpw = input('enter the specific heat of fluid');
cpwv = input('enter the specific heat of vapour');

muw = input('enter the visocity of fluid');
muwv = input('enter the viscocity of vapour');



% kw  = 0.607;
% kwv = 0.0106;
% cpw = 4180;
% cpwv = 1760;
% muw = 0.0008;
% muwv = 0.0016;

Tx = input('enter the fluid temperature');
Ty = input('enter the wall temperature');
```

```
V= M+1;
%m divsions of uin
divu = zeros(V,N);
Ts  = zeros(V,N);

for i=1:V
    divu(i,:) = divu(i,1)+(i-1)*(uin/M);
    Ts(i,:)=Tx;
end

for i=1:N
    Ts(1,i)=Ty;
end

Es = divu;
Esn = Es;
Edn = Es;
Est = Es;
delpnd = delpi;
phi = 0.5;
E = 0;

delp = ones(V,N)*0.001;
% delp = ones(9,N);

for i=2:N
    for j=2:M
        count20 = 0;
        E=0;
        df=1;
        delpnd = delpi;
        while(df>0.0001 && count20<5)
            E1 = delpnd;
%             Esn(j,i) = (delt/delx)*(delpnd)+(delt/dely^2)*((Est(j-
1,i)-2*Est(j,i)+Est(j+1,i)))+Est(j,i);
            Esn(j,i) = (delt/delx)*(delpnd)+(delt/(2*dely))*((Est(j-
1,i)-2*Est(j,i)+Est(j+1,i)))+Est(j,i);
            delpnd = (delx/delt)*((Esn(j,i)-Est(j,i)));
%             Edn(j,i) = (delt/delx)*delpnd+(delt/dely^2)*(Esn(j-1,i)-
2*Esn(j,i)+Esn(j+1,i))+Esn(j,i);
            Edn(j,i) = (delt/delx)*delpnd+(delt/(2*dely))*(Esn(j-1,i)-
2*Esn(j,i)+Esn(j+1,i))+Esn(j,i);
            delpnd = (delt/delx)*(abs(Esn(j,i)-Edn(j,i)));
            Est(j,i) = Edn(j,i);

            df = abs(E-delpnd);
                E = delpnd;
            count20 = count20+1;
        end

         delp(j,i) = E1 + phi*E;
         Est(j,i) = Esn(j,i)+phi*Edn(j,i);
```

```
    end
end



%For finding T
%LW explicit method

for i=2:N-1
    for j=2:M
        a1 = U(i-1);
        a2 = U(i);
        a3 = U(i+1);
        [kt,Cp,mu]=materialpty(kw,kwv,cpw,cpwv,muw,muwv,a1,a2,a3);
        Ts(j,i)= (delt/delx*Cp)*delp(j+1,i)  +
((kt*delt)/(2*delx*Cp))*(Ts(j,i-1)-2*Ts(j,i)+Ts(j,i+1))  +
((kt*delt)/(2*dely*Cp))*(Ts(j-1,i)-2*Ts(j,i)+Ts(j+1,i))  +
((delt*mu)/(2*dely*Cp))*(abs(Est(j-1,i)-Est(j,i)))  +  Ts(j,i);

    end
end


TS = Ts(1:2:V,1:2:N);


%Final step of finding H
Tss = zeros(1,N);
h  = zeros(1,N);
for i=1:N
    s = sum(Ts(:,i));
    Tss(i) = s/N;
end



for i=1:N
    h(i) = 90400/(103-Tss(i));
end

h1 = h(1:2:end);

H = sum(h1)/(N/2);

disp('H value is---------');
disp(H);

%wrting final H
fn1 = 'H.txt';
fid = fopen(fn1,'w');
```

```
fprintf(fid, '%3.3f\n', H);
fclose(fid);



%wrting the h values
fn2 = 'HTC.txt';
fid = fopen(fn2,'w');
for i=1:length(h)
  fprintf(fid, '%3.3f\n', h(i));
end
fclose(fid);

fn3 = 'U.txt';
fid = fopen(fn3,'w');
for i=1:size(Est,2)
    for j=1:size(Est,1)
        fprintf(fid, ' %3.3f', Est(j,i));
    end
     fprintf(fid, '\n');
end
fclose(fid);

fn4 = 'delp.txt';
fid = fopen(fn4,'w');
for i=1:size(delp,2)
    for j=1:size(delp,1)
        fprintf(fid, ' %3.3f', delp(j,i));
    end
    fprintf(fid, '\n');
end
fclose(fid);


fn5 = 'Temp.txt';
fid = fopen(fn5,'w');
for i=1:size(Ts,2)
    for j=1:size(Ts,1)
        fprintf(fid, ' %3.1f', Ts(j,i));
    end
    fprintf(fid, '\n');
end
fclose(fid);
```

TDMA Main program

```
function[u]=TDMAmain(delt,delx,uin,alpha,N)

%%  Program has been tested on MATLAB, version R2010a and version
R2012a
%  version: 1.0
%  Jan 17, 2017
% Copyright (c) IPLAB 2017, Author: Krishna Kumar P
%All rights reserved.
%%

r = ones(1,N);

%find constants K1 and K2

idelt = 1/delt;
rc = uin/delx;

K1 = idelt+rc;
K2 = -rc;
%finding RHS

for i=1:N-1

    r(i) = rc*(alpha(i+1)-alpha(i))+(alpha(i)/delt);

end

r(N) = -rc*alpha(N);

%  Solve the  n x n  tridiagonal system for y:
%
%  [ a(1)  c(1)                                ] [  y(1)  ]   [  f(1)
]
%  [ b(2)  a(2)  c(2)                          ] [  y(2)  ]   [  f(2)
]
%  [       b(3)  a(3)  c(3)                    ] [        ]   [
]
%  [            ...   ...   ...                ] [  ...   ] = [  ...
]
%  [                    ...    ...    ...       ] [        ]   [
]
%  [                       b(n-1) a(n-1) c(n-1) ] [ y(n-1) ]   [ f(n-
1) ]
%  [                              b(n)  a(n)   ] [  y(n)  ]   [  f(n)
]
%
%  f must be a vector (row or column) of length n
%  a, b, c must be vectors of length n (note that b(1) and c(n) are not
used)
```

```
a = ones(1,N);
b = ones(1,N);
c = ones(1,N);
a = a.*0;
b = b.*K1;
c = c.*K2;
c(end)=0;

%applay TDMA algorithm (Thomas algorithm)

u = TriDiag(a,b,c,r,N);


end
```

Material Property

```
function[kt,Cp,mu]=materialpty(kw,kwv,cpw,cpwv,muw,muwv,a1,a2,a3)

b = (a1+a2+a3)/3;
kt = kwv*b+ kw*(1-b);
Cp = cpwv*b+cpw*(1-b);
mu = muwv*b+muw*(1-b);

end
```

APPENDIX D

CONTOUR PLOTS OF FORCED CONVECTIVE HEAT TRANSFER COEFFICIENT OF WATER-ETHANOL MIXTURE

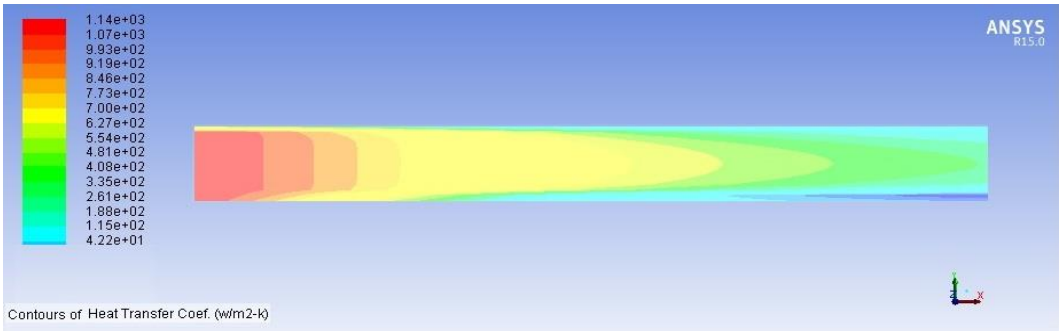

Figure D.1: Variation of forced convective heat transfer coefficient along the channel for water-ethanol mixture of ethanol volume fraction 50% at heat flux =21.78 kW/m^2 and mass flux=228.33 kg/m^2-s.

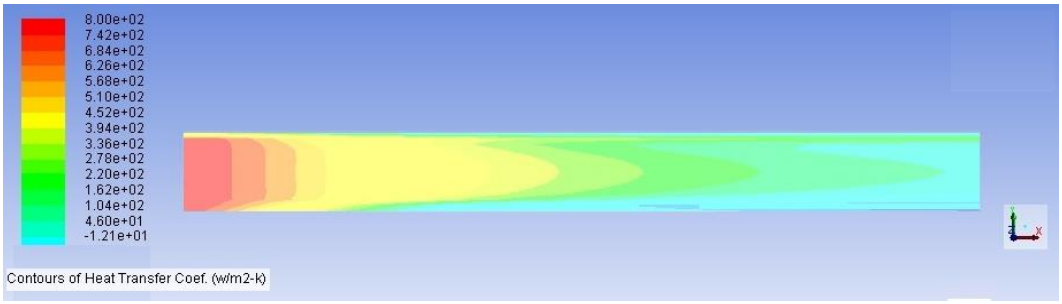

Figure D.2: Variation of forced convective heat transfer coefficient along the channel for water-ethanol mixture of ethanol volume fraction 75% at heat flux =21.78 kW/m^2 and mass flux=228.33 kg/m^2-s.

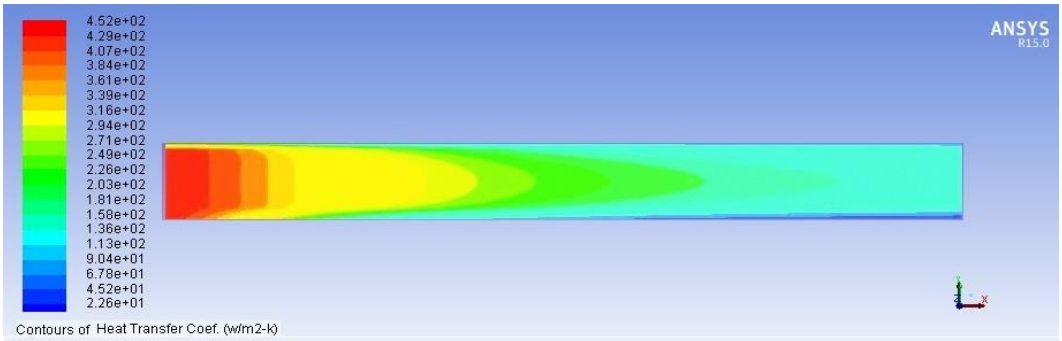

Figure D.3: Variation of forced convective heat transfer coefficient of ethanol along the channel at heat flux =21.78 kW/m^2 and mass flux=228.33 kg/m^2-s.

APPENDIX E

IMAGES OF BUBBLE FORMATION FOR WATER-ETHANOL MIXTURE

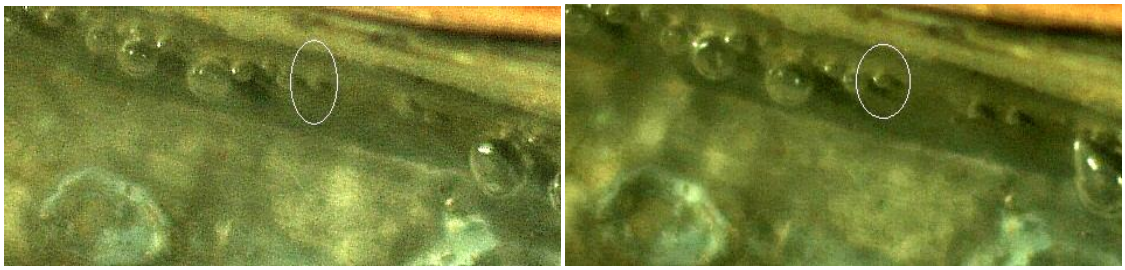

(a) (b)

(c) (d)

Figure E.1: Bubble formation in water at 100.3 kW/m^2 and mass flux=115.33 kg/m^2-s and inlet temperature=303 K.

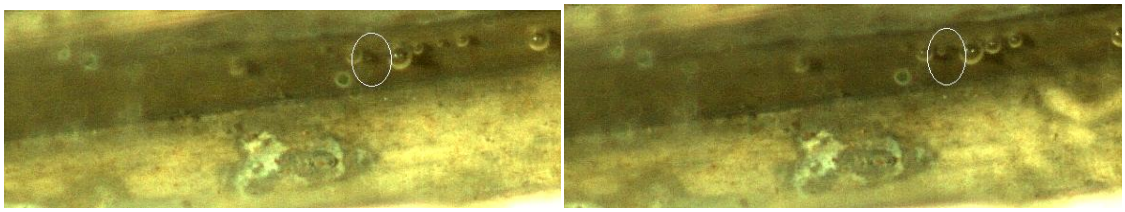

(a) (b)

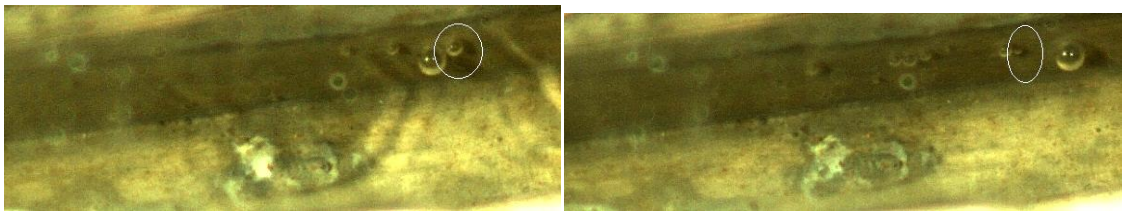

(c) (d)

Figure E.2: Bubble formation in water at 100.3 kW/m^2 and mass flux=228.33 kg/m^2-s and inlet temperature=303 K.

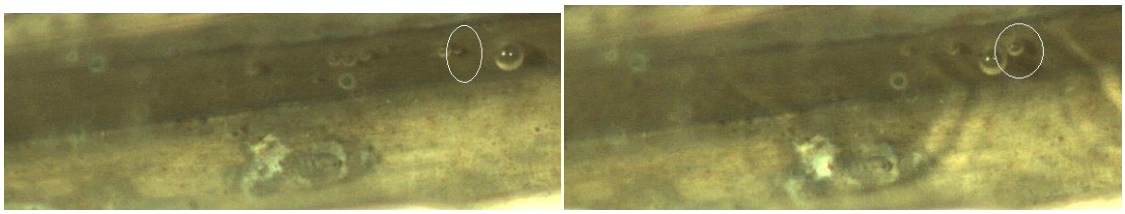

(a) (b)

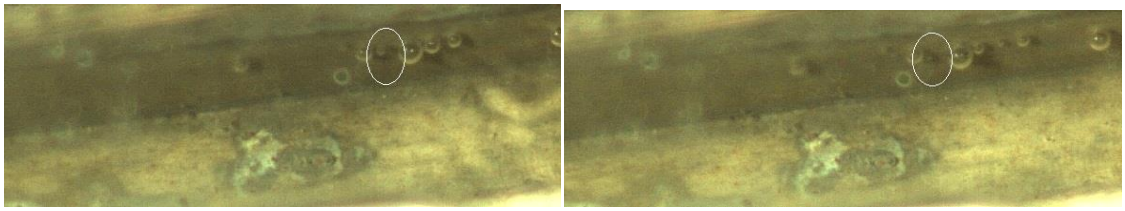

(c) (d)

Figure E.3: Bubble formation in water at 109.6 kW/m^2 and mass flux=115.33 kg/m^2-s and inlet temperature=323 K.

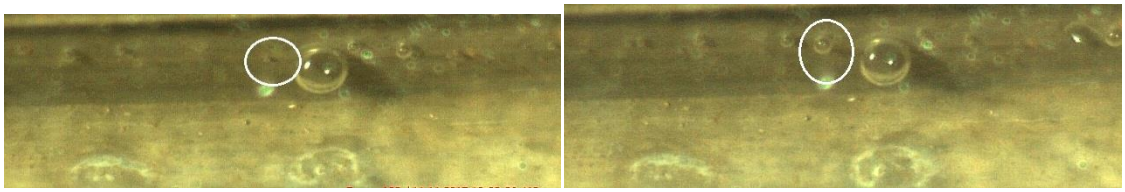

(a) (b)

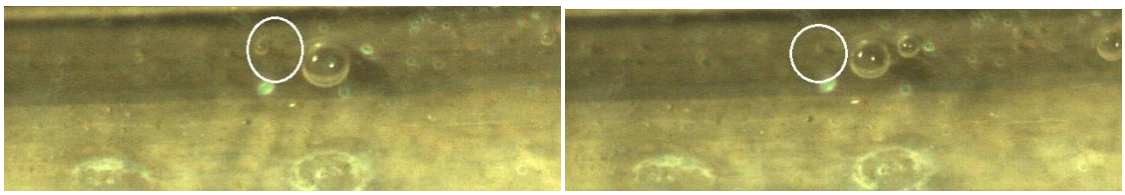

(c) (d)

Figure E.4: Bubble formation in water at 109.6 kW/m^2 and mass flux=228.33 kg/m^2-s and inlet temperature=323 K.

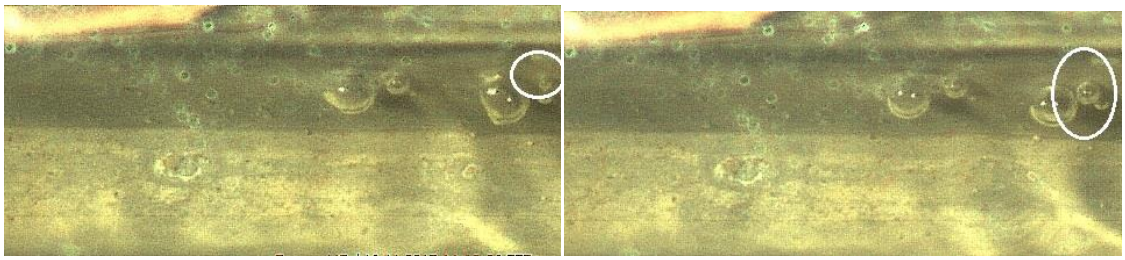

(a) (b)

(c) (d)

Figure E.5: Bubble formation in water at 121.5 kW/m^2 and mass flux=228.33 kg/m^2-s and inlet temperature=323 K.

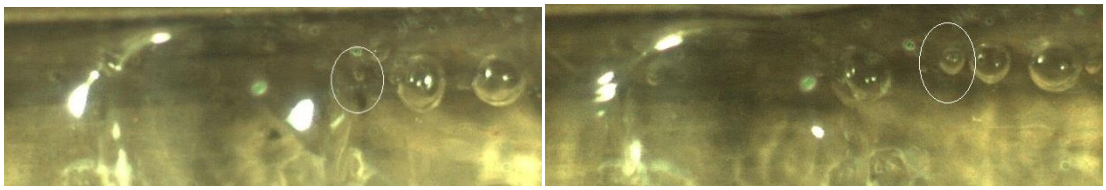

(a) (b)

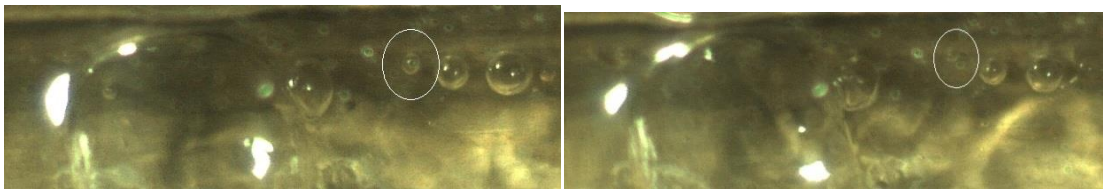

(c) (d)

Figure E.6: Bubble formation in water-ethanol mixture of ethanol volume fraction 25% at 90.4 kW/m^2 and mass flux=115.33 kg/m^2-s and inlet temperature=303 K.

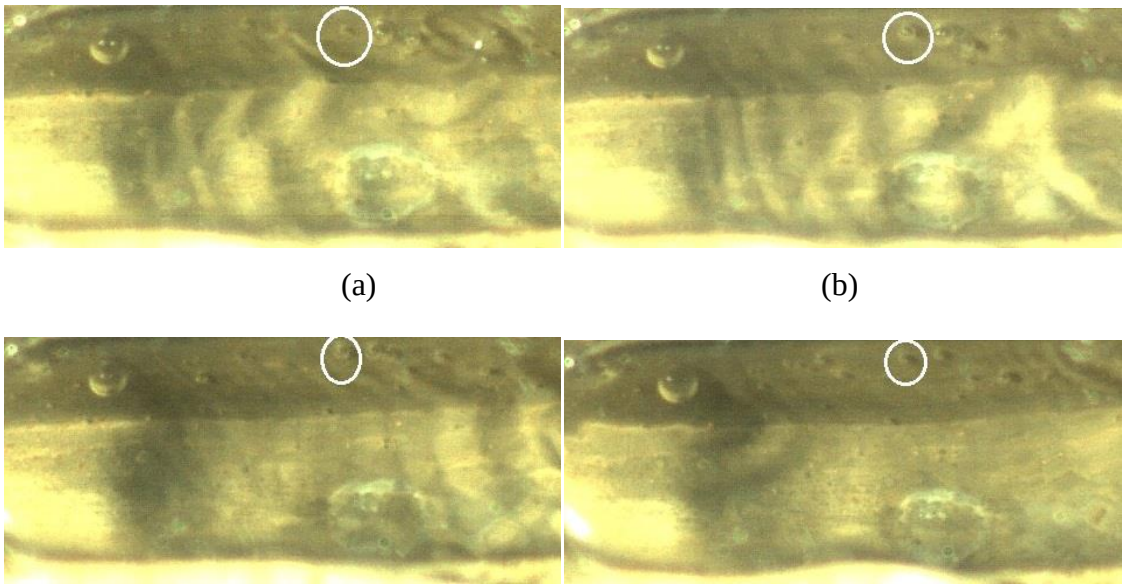

(a) (b)

(c) (d)

Figure E.7: Bubble formation in water-ethanol mixture of ethanol volume fraction 25% at 90.4 kW/m^2 and mass flux=228.33 kg/m^2-s and inlet temperature=323 K.

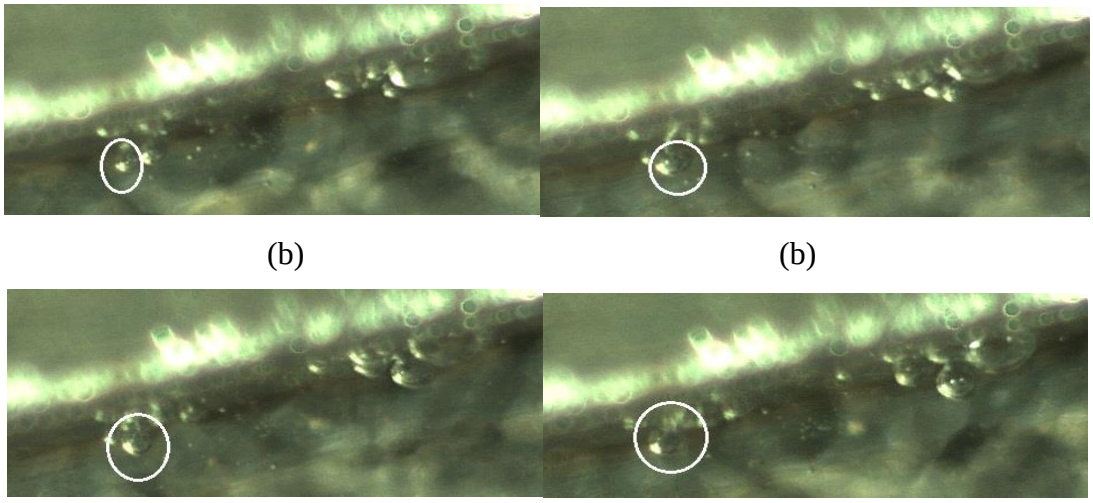

(b) (b)

(c) (d)

Figure E.8: Bubble formation in water-ethanol mixture of ethanol volume 50% at 90.4 kW/m^2 and mass flux=76.67 kg/m^2-s and inlet temperature=323 K.

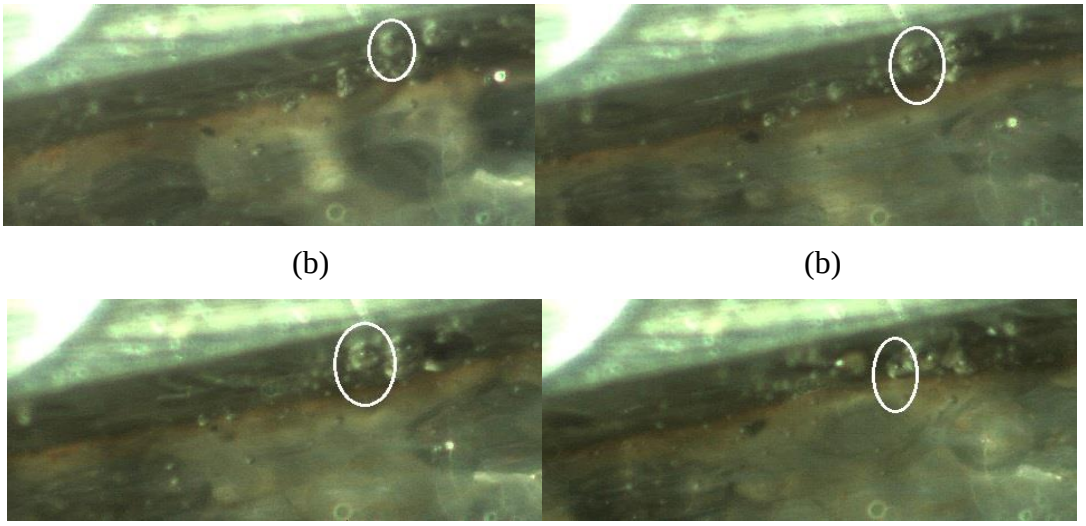

(b) (b)

(c) (d)

Figure E.9: Bubble formation in water-ethanol mixture of ethanol volume fraction 75% at 90.4 kW/m^2 and mass flux=115.33 kg/m^2-s and inlet temperature=313 K.

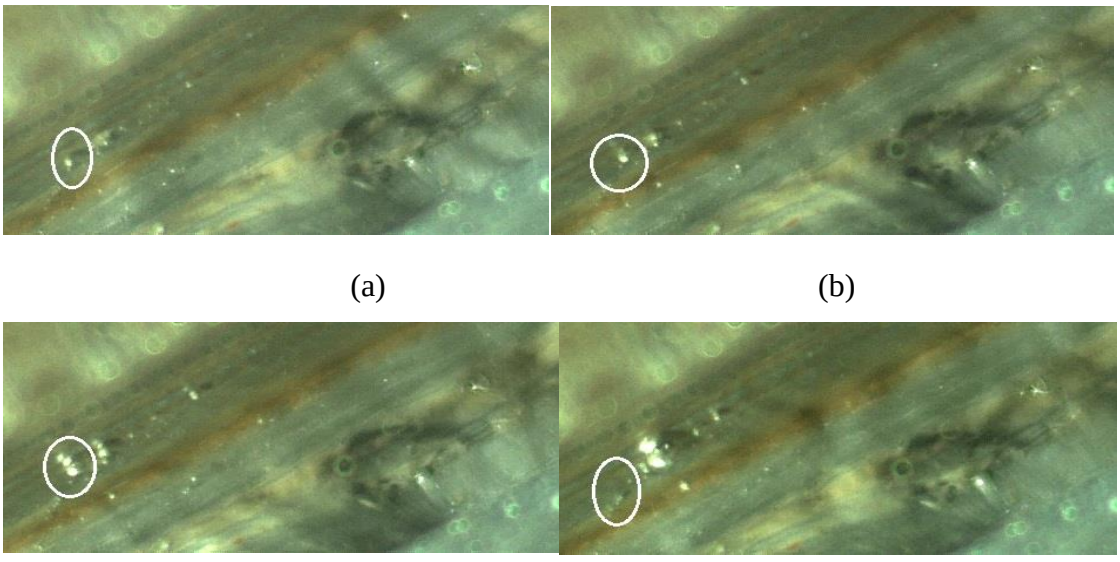

(a) (b)

(c) (d)

Figure E.10: Bubble formation in Ethanol at 90.4 kW/m^2 and mass flux=228.33 kg/m^2-s and inlet temperature=323 K.

LIST OF PUBLICATIONS

1. Journal publications

1. **Suhas**, **B.G.** and Sathyabhama, A. (2016). "Numerical Analyses of Single-Phase Pressure Drop and Forced Convective Heat Transfer Coefficient of Water–Ethanol Mixture: An Application in Cooling of HEV Battery Module", *Heat Transfer—Asian Research* 45 (7): 681-698.

2. **Suhas**, **B.G.** and Sathyabhama, A. (2017). "Bubble dynamics of water-ethanol mixture during subcooled flow boiling in a conventional channel", *Applied Thermal Engineering* 113: 1596–1609.

3. **Suhas**, **B.G.** and Sathyabhama, A. (2017). "Experimental Investigation of Heat Transfer Coefficient and Correlation Development for Subcooled Flow Boiling of Water–Ethanol Mixture in Conventional Channel", *J. of Thermal Science and Engineering application,* ASME 9(4):041003-11.

4. **Suhas**, **B.G.** and Sathyabhama, A. (2018) "Heat transfer and force balance approaches in bubble dynamic study during subcooled flow boiling of water–ethanol mixture", *Experimental Heat Transfer,* Taylor and Francis 30 (1): 1-21.

5. **Suhas**, **B.G.** and Sathyabhama.A. (2018) Experimental study on forced convective and subcooled flow boiling heat transfer coefficient of water-ethanol mixtures: An application in cooling of HEV battery module, *Heat and Mass Transfer,* Springer 54: 277-290.

. Conference proceedings/Symposium

1. **Suhas B.G** and Sathyabhama, A. (2014). Influence of operating parameters on the battery module cooling in hybrid electric vehicles, Proceedings of the 5th International and 41st national conference on fluid mechanics and Fluid power, December 14-16, Indian Institute of Technology, Kanpur, UP, India

2. **Suhas, B.G.,** Pushkar, K and Sathyabhama, A. (2016). Numerical investigation of forced convective heat transfer coefficient of water-ethanol mixture in a horizontal rectangular channel, Proceedings of the 6th International and 43rd national conference on fluid mechanics and Fluid power, December 15-17, MNNITA, Allahabad, U.P., India.

3. **Suhas, B.G.,** and Sathyabhama, A. (2017). Investigation of heat transfer coefficient and Bubble dynamics of ethanol during subcooled flow boiling, 6th International Engineering Symposium - IES 2017 March 1-3, Kumamoto University, Japan.

BIODATA

Suhas B.G
"Sukritha", Vivekanandanagara
Mangaluru, Dakshina Kannada
Karnataka-575006
Contact no: 8105510164
e-mail: suhas_bg@yahoo.co.in

PROFESSIONAL SUMMARY

Results-oriented thermal engineer with a hands-on approach to tackling projects and accomplishing goals.

SKILLS

- Ansys-ICEM
- Fluent
- Math work-Matlab
- Microsoft office and excel
- Solid edge

AREAS OF INTEREST

Advanced Fluid Mechanics, Advanced Heat Transfer, Air conditioning systems, Biomass energy, Computational fluid dynamics, Combustion, Cryogenics, Gas Dynamics, Gas turbine theory, Internal combustion Engines, Refrigeration systems, Solar Energy, Turbomachines and Wind energy.

EXTRA-CURICULAR ACTIVITIES

- Participated and volunteered in 42nd National Conference on Fluid Mechanics and Fluid power held during December 14-16, 2015 at NITK, Surathkal.
- Participated in National workshop on *Biofluid Dynamics and Bioheat transfer* held during 20th-21st Febraury 2017 at NITK, Surathkal.
- Participated in Spring Internship Programme held during March 4th-6th 2017 at Kumamuto University, Japan.
- Participated in National workshop on *Recent Advances and Challenges in Solar Thermal Systems* during 20th March 2017 at NITK, Surathkal.

EDUCATIONAL QUALIFICATION

Qualification	Discipline	Area of Specialization	Name of the Institution	Year of passing	CGPA / Percentage
SSLC	NA	NA	Canara High School (Main), Mangaluru	May 2004	92.8 %
PUC	PCMB	NA	Canara PU college, Mangaluru	May 2006	76.67%
Graduation	Mechanical Engineering (BE)	NA	PESIT, Banashankari campus, Bengaluru	June 2010	65.8%
Post-Graduation	Thermal Engineering (M.Tech Research)	Study of performance and emission characteristics of Hydrogen blend in SI Engine	NITK, Surathkal, Mangaluru	June 2013	7.71 CGPA
Doctoral Programme	Thermal Engineering	Heat transfer and bubble dynamic study on subcooled flow boiling of water-ethanol mixture	NITK, Surathkal, Mangaluru	February 2018	8.13 CGPA